

**Analysis of Sleeve Fracturing and Burst Experiments for Measurement of In-Situ Stress
and Rock Fracture Toughness**

by

Yao Huang

Undergraduate degree, University of Science and Technology of China, 2011

Master's degree, China University of Petroleum, Beijing, 2017

Submitted to the Graduate Faculty of the
Swanson School of Engineering in partial fulfillment
of the requirements for the degree of
Doctor of Philosophy

University of Pittsburgh

2022

UNIVERSITY OF PITTSBURGH

SWANSON SCHOOL OF ENGINEERING

This dissertation was presented

by

Yao Huang

It was defended on

March 30, 2022

and approved by

Andrew P. Bunger, PhD, Associate Professor, Department of Civil and Environmental
Engineering & Department of Chemical and Petroleum Engineering

Jeen-Shang Lin, PhD, Associate Professor, Department of Civil and Environmental Engineering

William Harbert, PhD, Professor, Department of Geology and Environmental Science

John Brigham, PhD, Associate Professor, Department of Civil and Environmental Engineering

Dissertation Director: Andrew P. Bunger, PhD, Associate Professor, Department of Civil and
Environmental Engineering & Department of Chemical and Petroleum Engineering

Copyright © by Yao Huang

2022

Analysis of Sleeve Fracturing and Burst Experiments for Measurement of In-Situ Stress and Rock Fracture Toughness

Yao Huang, PhD

University of Pittsburgh, 2022

Sleeve fracturing is a promising but underused field method for estimation of maximum and minimum horizontal stress in the subsurface. Similarly, the burst experiment is a laboratory technique for estimation of fracture toughness of rock under confined conditions that has been sparingly used for several decades by the petroleum industry. The techniques both involve pressurizing an uncased borehole until one or more fractures emanate from the borehole. However, ambiguity in their interpretation has led to inconsistencies and has been the primary barrier to wider adoption and full realization of the potential of these promising techniques. The main shortcoming is that previous analyses are constrained by Linear Elastic Fracture Mechanics (LEFM) or elastic stress analysis, for which the essential assumptions are violated in the vast majority of practically-relevant cases. Thus motivated, this research is aimed at simulating the behavior of fractures emanating from a pressurized borehole in both lab and field scale so that the measurements of this fracture initiation and growth can be leveraged for in-situ stress and fracture toughness estimation. The forward analysis uses cohesive zone elements in a Finite Element Analysis framework.

Working from these simulations for sleeve fracturing, a rapidly-deployable inversion algorithm is developed to estimate the maximum and minimum horizontal stress based on the field data. The results show that, combining this inversion algorithm with data that is available from

recent developments in field measurements using Fiber Optic sensors, the full potential of sleeve fracturing to predict both minimum and maximum horizontal in-situ stress can be realized.

Then, turning attention to the laboratory burst experiments, the results show that choosing a 3-parameter traction-separation law for the cohesive zone model is able to capture the impact of confining stress and specimen geometry. This is a major improvement over LEFM analysis, for which *ad hoc* dependence of the fracture toughness on confining stress and specimen geometry must be introduced. Furthermore, the results show that running burst experiments with different specimen geometries can provide a promising path to the challenging goal of experimental characterizing a traction-separation for a given rock (or other quasi-brittle) material.

Table of Contents

Preface.....	xvii
1.0 Introduction.....	1
2.0 Numerical Simulation of Sleeve Fracturing for In-Situ Stress Measurement using Cohesive Elements.....	6
2.1 Preamble.....	6
2.2 Chapter Summary	6
2.3 Introduction	7
2.4 Model Methodology	10
2.5 Model Setup	12
2.5.1 Field-Scale Model Setup	12
2.5.2 Lab-Scale Model Setup	15
2.6 Validation of Model.....	17
2.6.1 Validation of Model with Kirsch’s Solution	17
2.6.2 Validation of Model with Laboratory Test.....	18
2.7 Field Scale Simulation Results	22
2.8 Parametric Study of Cohesive Element Properties	26
2.9 Displacements Around the Wellbore	33
2.10 Specific Field Scale Case with Nearly Equal In-Situ Stress	35
2.11 Discussion	37
2.12 Conclusion	39

3.0 An Inversion Algorithm to Estimate Maximum and Minimum Horizontal Stress	
Based on Field Test Data for Sleeve Fracturing.....	41
3.1 Preamble.....	41
3.2 Chapter Summary	41
3.3 Introduction	42
3.4 Identify Algorithm Inputs from Data.....	45
3.5 Algorithm Methodology.....	48
3.6 Validation of Algorithm.....	51
3.7 Error and Uncertainty	53
3.8 Conclusion.....	56
4.0 Cohesive Elements Capture Size and Confining Stress Dependence of Rock	
Fracture Toughness Obtained from Burst Experiments.....	58
4.1 Preamble.....	58
4.2 Chapter Summary	58
4.3 Introduction	59
4.4 Background.....	62
4.5 Modelling Methodology	70
4.5.1 Cohesive Zone Elements.....	70
4.5.2 Model Setup.....	73
4.6 Results.....	77
4.6.1 Unstable Cases.....	77
4.6.2 Confined Stable Cases	82
4.6.3 Unconfined Partially Stable Cases.....	87

4.7 Comparison with Laboratory Experiments	91
4.8 Discussion of T-S Law	94
4.9 Conclusions	97
5.0 Conclusions.....	99
Appendix A Extended Discussion of Lab Scale Simulation	102
Appendix B Impact of In-Situ Stresses on Key Quantities	107
Appendix C Picking Key Quantities for Illustrative Cases.....	111
Appendix D Values Corresponding to Figure 24 and 25	117
Bibliography	121

List of Tables

Table 1 Material properties	14
Table 2 In-situ stresses for different cases	15
Table 3 Material Properties	16
Table 4 Comparison of simulation results with lab test data for the pressure associated with first and second crack initiation.	22
Table 5 Material properties and in-situ stress	46
Table 6 Material properties of Kasota Valley Limestone (Lu et al. 2020; Lu et al. 2017; Lu 2016)	75
Table 7 Configuration properties and stability for lab tests (after Zhang 2019 and Yoshioka et al. submitted).....	77
Table 8 CZ element properties.	93
Appendix Table 1 Comparison of simulation results with lab test data for the pressure associated with first and second crack initiation.	105
Appendix Table 2 Comparison of lab-scale simulation results with different cohesive element properties for the pressure associated with first and second crack initiation.....	106
Appendix Table 3 P_I obtained by field-scale cases under different in-situ stresses.....	107
Appendix Table 4 P_I obtained by field-scale cases for different cohesive element strength.	107
Appendix Table 5 Key quantities for four example cases.....	111
Appendix Table 6 Comparison of estimated and actual in-situ stresses for four example cases	112

**Appendix Table 7 Comparison of mean and standard deviation for estimated in-situ stresses
varying different key quantities for illustrative case (see Figure 23 in major text).118**

**Appendix Table 8 Comparison of mean and standard deviation for estimated in-situ stresses
varying all the key quantities for three illustrative cases with 5% uncertainty level for
 P_2 119**

**Appendix Table 9 Comparison of mean and standard deviation for estimated in-situ stresses
varying all the key quantities for three representative cases with different uncertainty
level for P_2 120**

List of Figures

Figure 1 World Stress Map, from Heidbach, et al. 2018, used with permission.....	2
Figure 2 Generic illustration of rock elements connected together by cohesive zone elements on a potential plane of crack growth (after ABAQUS 2011).	10
Figure 3 Traction-separation law of cohesive elements (after Barrenblatt 1962 and Dugdale 1960).	12
Figure 4 Model setup for field test, showing a) Full model including infinite elements around the model’s perimeter, and b) Closer view of borehole with pre-defined crack trajectories.	13
Figure 5 Loading setup for field-scale simulation.....	14
Figure 6 Model setup for the laboratory test.....	16
Figure 7 Benchmark of numerical simulation with Kirsch’s (1898) solution.	18
Figure 8 Setup for the laboratory test for: a) Complete setup including pumping equipment with a concrete specimen, note that a constraining metal pipe covered the expandable portion of the sensor assembly that protruded from the rock specimen during inflation; b) Close-up of cored sandstone rock specimen with inflatable sensor assembly inserted.	19
Figure 9 Lab-scale simulation result with ABAQUS finite domain at the correct scale.....	20
Figure 10 Field-scale simulation results showing the open cohesive elements for: a) Case 1; b) Case 2; c) Case 3; d) Case 4. Deformed cohesive elements are shown at wellbore pressures indicated by P, which are somewhat above the corresponding crack	

initiation pressures so that the deformed cohesive elements are visible and illustrative of crack growth directions.....	23
Figure 11 Crack initiation and propagation behavior for field-scale under different in-situ stresses a) Case 1; b) Case 2; c) Case 3; d) Case 4.	24
Figure 12 Field-scale simulation results showing the open cohesive elements for: a) $\alpha=0.003$; b) $\alpha=0.03$; c) $\alpha=0.6$; d) $\alpha=0.9$. Deformed cohesive elements are shown at wellbore pressures indicated by P, which are somewhat above the corresponding crack initiation pressures so that the deformed cohesive elements are visible and illustrative of crack growth directions.....	27
Figure 13 Crack initiation and propagation behavior for field-scale under different α (recall w_1 and w_2 are the crack opening at the wellbore for the first and secondary crack, respectively).	28
Figure 14 Field-scale simulation results showing the open cohesive elements for: a) $T_{max}=1\text{MPa}$; b) $T_{max}=2\text{MPa}$; c) $T_{max}=4\text{MPa}$; d) $T_{max}=10\text{MPa}$. Deformed cohesive elements are shown at wellbore pressures indicated by P, which are somewhat above the corresponding crack initiation pressures so that the deformed cohesive elements are visible and illustrative of crack growth directions.....	29
Figure 15 Crack initiation and propagation behavior for field-scale for different T_{max}, with the inflection point for one case labelled as an illustration.	30
Figure 16 Field-scale simulation results showing the open cohesive elements for: a) $G_c=8\text{N/m}$; b) $G_c=16\text{N/m}$; c) $G_c=32\text{N/m}$; d) $G_c=64\text{N/m}$. Deformed cohesive elements are shown at wellbore pressures indicated by P, which are somewhat above the	

corresponding crack initiation pressures so that the deformed cohesive elements are visible and illustrative of crack growth directions..... 32

Figure 17 Crack initiation and propagation behavior for field-scale for different Gc. 33

Figure 18 Wellbore circumferential displacement and its corresponding simulation results showing the open cohesive elements for a) P=10.15MPa; b) P=21.15MPa; c) P=37.15MPa..... 34

Figure 19 Field-scale simulation results showing the open cohesive elements for case with equal in-situ stresses: a) initiation period; b) propagation period. Deformed cohesive elements are shown at wellbore pressures indicated by P, which are somewhat above the corresponding crack initiation pressures so that the deformed cohesive elements are visible and illustrative of crack growth directions. 36

Figure 20 Crack initiation and propagation behavior for field-scale with equal in-situ stress. 36

Figure 21 Sketch of the sleeve fracturing technique..... 44

Figure 22 Data curves with inflection points and key quantities labelled for one representative case showing: a) P_2 and σ_{PP} ; b) P_1 ; c) θ , the angle between first and secondary cracks. 47

Figure 23 Comparison of estimated and actual in-situ stress for: a) maximum horizontal stress; b) minimum horizontal stress. 52

Figure 24 Comparison of histogram curves of the estimated horizontal stresses varying different key quantity for illustrative Case with actual $\sigma_{Hmax} = 15\text{MPa}$ and actual $\sigma_{Hmin} = 10\text{MPa}$ for: a); Comparison of uncertainty level for estimated maximum horizontal stress; b); Comparison of uncertainty level for estimated minimum

horizontal stress; c); Histogram curve for estimated maximum horizontal stress with confidence interval labelled; d) Histogram curve for estimated minimum horizontal stress with confidence interval labelled..... 54

Figure 25 Comparison of uncertainty of estimated horizontal stresses with different θ generated from two different uncertainty of P_2 for: a) maximum horizontal stress; b) minimum horizontal stress..... 56

Figure 26 Published results of fracture toughness versus confining stress on Indiana Limestone (after Roegiers, 1991; Thallak, 1993; Abou-sayed 1978; Schmidt and Huddle, 1977)..... 64

Figure 27 Lab setup for burst experiment (after Abou-Sayed 1978)..... 66

**Figure 28 AE sensor layout on the specimen, viewed from the top looking down (Zhang 2019).
..... 67**

Figure 29 Possible evolution of normalized stress intensity factor $K_I^{(B^*)}$ versus normalized crack length l (after Yoshioka et al. submitted)..... 69

Figure 30 . Data curves with two possible Pic labelled for lab experiment results of test 3 (1/2 inch borehole in a 6 inch specimen, the ratio of confining stress over internal stress is 1/8) (after Zhang 2019). 70

Figure 31 Bi-linear traction-separation law of cohesive elements (after Barrenblatt 1962 and Dugdale 1960)..... 73

Figure 32 Sketch of model setup for burst experiment: a) Boundary conditions and loading setup; b) Mesh setup for 1/2-inch borehole; c) Mesh setup for 2-inch borehole..... 76

Figure 33 Simulation results showing the open cohesive elements colored by SDEG value and maximum principal stress contour for lab test 8 (2-inch borehole, showing the ratio of confining stress over internal stress is 1/8) at: a) 22.95s; b) 24.21s; c) 24.22s..... 80

Figure 34 Crack width and length versus internal pressure with P_{ic} labelled for CZ-based simulation of test 8 (2-inch borehole, showing the ratio of confining stress over internal stress is 1/8). 81

Figure 35 Simulation results showing the open cohesive elements and maximum principal stress contour for stable cases (1/2 inch borehole, showing the ratio of confining stress over internal stress is 1/8) at: a) 289.96s; b) 307.96s; c) 500.00s..... 84

Figure 36 Crack opening versus internal pressure curve for CZ-based simulation of stable cases (1/2 inch borehole, showing the ratio of confining stress over internal stress is 1/8). a) showing the entire date with pressure increased to 150MPa; b) focusing on the first 50MPa with P_{ic} labelled..... 86

Figure 37 Simulation results showing the open cohesive elements and maximum principal stress contour for tests 1 and 2 (unconfining test with 1/2 inch borehole) at: a) 122.96s; b) 127.58s; c) 128.14s. 89

Figure 38 Crack width and length versus internal pressure with P_{ic} labelled for CZ-based simulation of tests 1 and 2 (unconfining test with 1/2 inch borehole). 90

Figure 39 Comparison of burst pressure obtained from experiments and CZ-based simulations as well as LEFM methods. Note that KIC for the one parameter LEFM model is taken as 0.73 94

Figure 40 Comparison of stress concentration of case8 at the same crack length 18.00mm under different critical separation ratio 96

Appendix Figure 1 Crack opening versus pressure loading for ABAQUS infinite domain, i.e. (incorrectly) assuming that the load application in the lab can be replaced with a far field stress in an infinite domain. 104

Appendix Figure 2 Crack interaction behavior for field-scale under different in-situ stresses, with P_2 and σ_{PP} labelled as an illustration for: a) $\sigma_{Hmax}=20\text{MPa}$, $\sigma_{hmin}=10\text{MPa}$; b) $\sigma_{Hmax}=15\text{MPa}$, $\sigma_{hmin}=10\text{MPa}$; c) $\sigma_{Hmax}=20\text{MPa}$, $\sigma_{hmin}=15\text{MPa}$; d) $\sigma_{Hmax}=30\text{MPa}$, $\sigma_{hmin}=10\text{MPa}$ 108

Appendix Figure 3 Crack interaction behavior for field-scale for different cohesive element strength, with P_2 and σ_{PP} labelled as an illustration for: a) $T_{max}=1\text{MPa}$; b) $T_{max}=2\text{MPa}$; c) $T_{max}=3\text{MPa}$; d) $T_{max}=4\text{MPa}$ 109

Appendix Figure 4 Data curves with key quantities labelled for Case 10 showing: a) P_2 and σ_{PP} ; b) P_1 113

Appendix Figure 5 Data curves with key quantities labelled for Case 15 showing: a) P_2 and σ_{PP} ; b) P_1 114

Appendix Figure 6 Data curves with key quantities labelled for Case 30 showing: a) P_2 and σ_{PP} ; b) P_1 115

Appendix Figure 7 Data curve for Case 97, with P_1 quantity labelled. 116

Preface

Theoretical and applied mechanics is the origin of my scientific journey. I used to deviate from this beautiful way while it takes a long time for me to come back to my origin. It is the time to start the new adventure to a broader mechanics world. To everyone who have supported me during my PhD study, I wish to express my sincere gratitude.

First and foremost, I would like to express my deepest admiration for my advisor, Professor Andrew Bungler, who completely trust and support me during my path of achieving career goals. It is kind of fate for me to meet him and obtain the opportunity to pursue my PhD under his guidance. He is such a perfect advisor to me that I learned so much from him. The training I obtained from him benefit me so much in my research, my career, and my life. He is the kind of advisor who is always willing to help with sincerity. I do enjoy working with him that this experience has created a wonderful memory that will never fade in my life. I do admire our discussion through my research and career plan. His creativity and enthusiasm in rock mechanics lead me to a broader mechanics world. Furthermore, the insightful suggestions and strong assistance he provided for me to achieve my career goals in academia are priceless treasure for my life. Andy is the sun who bring the brilliant light to my world without doubt.

I would like to thank for the Support which is provided from Luna Innovations as a subaward (3723.01/PITT) on a Shell GameChanger Grant (CW235436). This support, as well as permission to publish, is gratefully acknowledged. I would like to express my great appreciation to my collaborators Dr. John Ohanian from Luna Innovations with Dr. Alexei Savitski and Dr. Haiyong Cai from Shell Exploration and Production for providing substantial inputs to this study and creating the collaborative environment. I also greatly appreciate constructive and useful

discussions with Dr. Tom Doe, especially of the technical history of sleeve fracturing, and with Dr. Alexei Savitski and Dr. Haiyong Cai and other colleagues at Shell with respect to the integration of simulations with field measurements. It is a privilege for me to work together with these professionals that I have benefited quite a lot from their insightful suggestions.

Moreover, I would like to thank my committee members Professor Jeen-Shang Lin, Professor Luis Vallejo, Professor John Brigham and Professor William Harbert for their professional guidance and time dedicated to this dissertation. I would also like to express my appreciation for my previous advisors Professor Liangming Peng and Professor Shiqing Cheng for the guidance and opportunities they used to offer me.

I gratefully acknowledge the contributions to this work by my colleague at University of Pittsburgh, Dr. Navid Zolfaghari for his professionally technical guidance at the very beginning for this study. I sincerely appreciate the insightful suggestions provided by my senior colleague Dr. Fu Wei and Yunxing Lu. Moreover, I would like to say thank you to all my friends and my fellow graduate students in our research group, Navid Zolfaghari, Wei Fu, Guanyi Lu, Pengju Xing, Qiao Lu, Delal Gunaydin, Maggie Benghe and Yunxing Lu for our scientific discussion and wonderful friendship.

I would like to express the deepest gratitude to my parents and my godmother Deng for their endless love, support, and encouragement. They are my most significant treasure. It is their love that help me to recover from the hell I used to surfer. It is their love that support me to fly over thousands of miles oversea to fight for my dream. It is their love that make me become what I am now. Wish them all healthy and happy.

When I was a kid, I dreamed to be a great scientist. Then I went to my dream university. It could have become a brilliant start of my dream. However, I was too young to face myself at that

time, leading to the first failure in my life. The non-healing cracks are further left on myself. I have to say it takes me a long way to do the self-healing. Indeed, the cracks never disappeared and will not disappear in the future. However, I have gained enough power and love to live with them. Thank you again to my dear advisor, I do enjoy my PhD life and this part of time completely healed me. I am prepared to spread my wings to the broader beautiful scientific world.

Finally, I would like to give my special gratitude to myself. It is a long way with so many challenges and uncertainties. However, you did it! You have overcome all the difficulties and all the challenges and finally you step here by yourself successfully. All hail to you, dear Dr. Yao Huang! May God bless all your future endeavors.

1.0 Introduction

Pressurizing an uncased borehole by using an inflatable packer can lead to one or more fractures emanating from the borehole. The initiation and propagation behavior of the stimulated fractures and the interaction behavior among these fractures are considered to be related to the in-situ stresses and the rock properties. Based on this premise, the technique “sleeve fracturing” has been proposed and applied in the evaluation of in-situ stresses by field testing (Stephansson 1983; Serata et al. 1992).

Knowledge of in-situ stresses is significant as this information has been widely used across a variety of cross-cutting areas, including but not limited to the Earth Sciences, Geo-Engineering, Petroleum Engineering and Mineral Engineering. The stress information is analyzed and compiled in a standardized format and quality-ranked for reliability and comparability on a global scale, as illustrated in Figure 1 (Heidbach, et al. 2018). In this collection of data, some of the stresses are considered to be known with high reliability because they are ascertained through combining different methods. Others, however, are less certain, often because they are estimated based solely on earthquake mechanism or the hydraulic fracturing stress testing technique. Because of this, some regions in the World Stress Map are left with high uncertainties. Therefore, there is a great importance to bring down these uncertainties in the orientation and magnitude of stresses mapped all around the World owing to the fact that they have been widely relied upon for things ranging all the way from assessing seismic hazard to reservoir characterization and management in oil and gas field.

Fundamentally, the in-situ stress can be represented by three principal stresses with their orientations. Vertical stress is typically taken as one of the principal stresses and is routinely

estimated based on integration of the density of the overburden. The minimum horizontal stress is usually estimated based on a variety of well-established tests (see the review of Ljunggren et al 2003). However, it is substantially more difficult to quantify the magnitude of maximum horizontal stress (σ_{Hmax}) and the maximum horizontal stress is left as one of the most uncertain subsurface properties. This is because fracture-based testing methods (e.g. Haimson and Cornet 2003) typically depend most directly on minimum stress, and the first fractures to open are opposed by the least compressive stress. Quantifying maximum stress therefore relies on ability to observe and interpret more subtle and/or subsequent details of fracture initiation and growth.

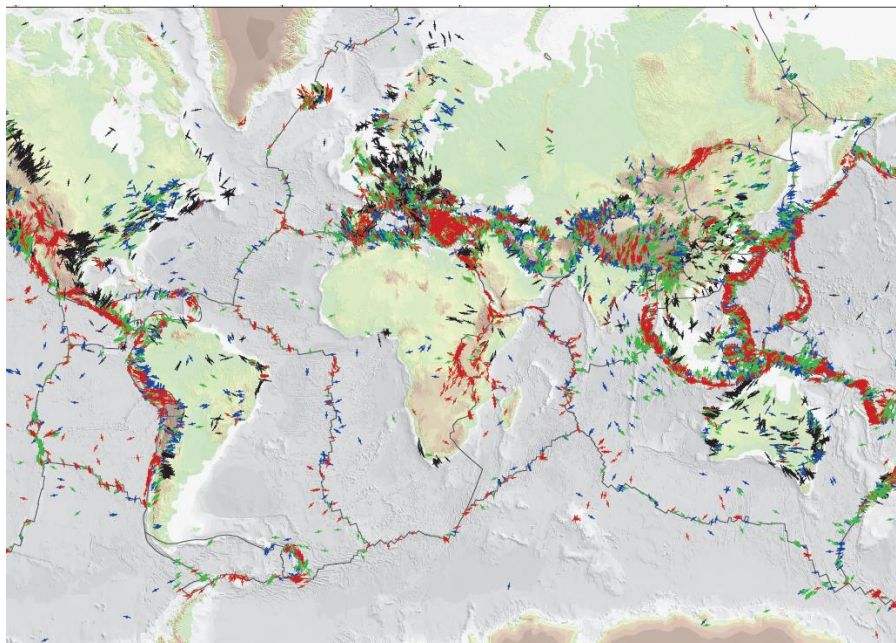


Figure 1 World Stress Map, from Heidbach, et al. 2018, used with permission.

The sleeve fracturing technique is an attractive technique holding the potential to estimate both maximum and minimum horizontal stresses (e.g. Moos and Zoback 1990; Zoback et al. 2003; Hickman and Zoback 2004; Stephansson 1983; Serata et al. 1992). Unlike hydraulic fracturing,

where fluid flows into the fractures and causes them to grow in length away from the borehole, sleeve fracturing does not allow the fluid to flow into the induced fractures by hydraulically isolating the wellbore and applying pressure through an inflatable packer (Stephansson 1983; Serata et al. 1992, see Figure 21), thereby increasing the opportunity for secondary fracture(s) to initiate by preventing rapid fluid loss to the first fracture(s). Thus, the sleeve fracturing technique has the advantages of removing uncertainty in the interpretation of in-situ stresses caused by fluid penetration into the surrounding rock. The secondary fracture initiation behavior has been proved to be essential to estimation of the maximum horizontal stress (Detournay and Jeffrey 1986) from sleeve fracturing tests. It used to be difficult to detect secondary fracture initiation in field test and in the analysis due to the technology limitation. However, this limitation of secondary fracture detection has been overcome by the advent of distributed strain sensing applying optical fibers, and the ability to embed such distributed strain sensors in the inflatable packer (Ohanian 2019, Ohanian et al. 2021). Chapters 2 and 3 of this dissertation comprise pre-prints of articles addressing firstly the simulation of sleeve fracture using cohesive zone elements in a finite element analysis framework (Chapter 2) and development of an inverse method for estimating in-situ stress magnitudes based on matching the model predictions with observed fracturing in field experiments (Chapter 3).

Bearing some mechanical similarity to sleeve fracturing, pressurizing a sleeve inside a pre-notched borehole until the fracture growth is detected by a burst event comprises a laboratory method called the “burst experiment” (Abou-Sayed 1978). This is long-used technique applied mainly in the oil and gas industry to estimate the fracture toughness of rocks under confinement. Unlike other approaches that test rock fracture toughness under unconfined conditions, the burst experiment can determine rock fracture behavior in the deep subsurface with large confining

stresses. In this test, radial confinement is applied to the boundary of a cylindrical specimen while an internal and axially-notched borehole is pressurized simultaneously. As the test proceeds (Abou-Sayed 1978), the external and internal pressure are proportionally increased, with the internal pressure typically ramping up with a slope that is six times greater than the external pressure, until a crack catastrophically grows, and a burst event occurs in the specimen that is detected in the pressure and flow rate records of the pump(s) that are controlling the internal and external applied pressures.

A variety of analyses have been conducted to analyze the fracture initiation and propagation behavior of a pressurized borehole while these previous analyses are typically based on Linear Elastic Fracture Mechanics (LEFM) or elastic stress analysis for both sleeve fracturing problem (e.g. Chandler 1989, Serata et al. 1992, Charsley et al. 2003) and the burst experiment (Zhang 2019 and Yoshioka et al. submitted). For analysis of sleeve fracturing, LEFM requires assumption that plasticity is confined to a region that is small relative to ad-hoc flaw(s) introduced near the wellbore in order to compute a stress intensity factor for comparison to a fracture toughness, which is assumed to be an intrinsic property of the rock. However, the crack initiation from a borehole have been proved to be substantially impacted by finite plasticity (zone of plastic deformation comparable in size to the crack and/or borehole) because of the fact that, in reality, the crack does not become “large” compared to the plastic zone until it substantially exceeds the borehole radius (Lecampion 2012), which means that the small-scale yielding assumption of LEFM is beyond the region of modeling interest for sleeve fracture. Furthermore, the LEFM assumes that the equations of elasticity are valid arbitrarily close to the crack tip in analysis of the burst experiment. In contrast, the process zone near the crack tip is expected to be at least on the order of 10 mm (Labuz et al. 1987; Lin and Labuz 2013) for most rocks, which is similar to the

size of both the borehole and the specimen itself for typical burst experiment setups. Consequently, LEFM-based analyses will miss size effects (and, more generally, impacts of geometric details of the specimen) that could be significant to experimental interpretation. Hence, new analyses are required to overcome the limitation due to the LEFM assumptions to interpret more details of fracture initiation and growth for both sleeve fracturing and the burst experiment.

Motivated by the knowledge gaps remaining due to reliance upon LEFM for analysis and the urgent needs to leverage advanced technology in distributed fiber optic sensing, this study aims to provide a well-validated and sufficiently precise method to analyze and quantify the crack initiation, propagation and interaction behavior of cracks emanating from a pressurized borehole by taking advantage of the classical cohesive zone (CZ) model developed by Barenblatt (1962) and Dugdale (1960). The simulation carried out for sleeve fracturing problem is developed using cohesive zone elements deployed within a Finite Element framework, which aims to overcome limitation of LEFM analysis and revisit the effect of in-situ stresses on first and second crack initiation and growth under sleeve fracturing conditions. The results of this forward simulation are then further applied to establish a well-validated and sufficiently accurate method to estimate both maximum and minimum horizontal stress from sleeve fracturing data. The study conducted for the burst experiment aims to characterize dependence of rock fracture on confining stress and specimen size by developing a CZ finite element model. The presented study further aims to capture the crack initiation and propagation behavior for laboratory experiments using a traction-separation law that is the same for all experiments without introducing ad hoc *ad hoc* dependence of the fracture toughness on both confining stress and hole size. The details of this analysis of the burst experiment comprise Chapter 4 of this dissertation.

2.0 Numerical Simulation of Sleeve Fracturing for In-Situ Stress Measurement using Cohesive Elements

2.1 Preamble

This chapter comprises a preprint of Huang et al. (2021a). It presents a numerical simulation to investigate the impact of in-situ stresses on initiation and propagation behavior of primary and secondary fractures at both field and lab scale by analyzing the fracture emanation from a wellbore under sleeve fracturing conditions. The numerical model has been verified against Kirsch's solution and results of a laboratory test. The field-scale simulation results have demonstrated that the first fracture always orients with the opening in direction of maximum in-situ stress while the opening direction of the second fracture can vary with different in-situ stresses.

2.2 Chapter Summary

Numerical analysis of growth of fractures from a wellbore under sleeve fracturing conditions demonstrates the impact of in-situ stresses on initiation and propagation behavior of primary and secondary cracks at both field and lab scale. Crack initiation and propagation behavior are simulated in a Finite Element framework employing plane-strain cohesive element along the candidate crack paths. The model has been validated by benchmarking to Kirsch's solution as well as by comparing predictions to results of a laboratory block test. Indeed, the field scale simulation results show that the first fracture always orients with the opening in direction of maximum in-situ

stress while the opening direction of the second fracture can vary with different in-situ stresses. Furthermore, the deviation of wellbore displacement from the Kirsch solution due to the fracture initiation can be captured by the simulation, which can be further applied to interpret the initiation pressure and location of cracks based on field test data. In the context of past contributions on sleeve fracturing, these numerical results demonstrate that a relatively large region near the crack tip undergoes inelastic deformation, which contrasts with the assumptions required to treat this problem using linear elastic fracture mechanics (LEFM). Notably, the finite tip plasticity appears to eliminate unstable jumping of the crack length(s) predicted by LEFM solution. The finite tip plasticity also leads to prediction that the secondary fracture often occurs in orientations other than 90 degrees to the primary fracture. In contrast, the LEFM solution predicts none of this growth because the stress intensity factor (SIF) never reaches the rock fracture toughness in spite of the fact that these alternate orientations have the largest SIFs over limited periods of time. Finally, the finite tip plasticity shows the strength of materials approach (based on stress analysis around the hole) to give a lower-bound estimate of the pressure required for crack extension.

2.3 Introduction

Pressurizing an inflatable packer in an uncased borehole until one or more cracks emanates from the borehole (“sleeve fracturing”) is a technique used for the evaluation of in-situ stresses (Stephansson 1983; Serata et al. 1992). It is attractive as a method largely because of the potential to measure both minimum and maximum horizontal stress components from a single vertical borehole. The connection between sleeve fracturing data and estimation of both horizontal principal stresses relies on modeling extension of primary cracks that grow in the plane acted upon

by the least compressive stress, followed by secondary cracks in another orientation. Analysis that uses Linear Elastic Fracture Mechanics (LEFM) predicts that crack growth can undergo an unstable jump in the crack length and that the secondary crack will grow at 90 degrees to the primary crack, and hence in the plane acted upon by the most compressive horizontal stress (Detournay and Jeffrey 1986). A variety of analyses of this problem have examined issues such as connection between wellbore conditions and far-field stresses as well as the validity of the prediction of secondary fracture growth at 90° from the primary fracture (e.g. Chandler 1989, Serata et al. 1992, Charsley et al. 2003). However, the models generally take on the assumptions of LEFM, namely, a negligibly-small region of near-tip plasticity and propagation requiring $K_I=K_{IC}$, where K_I is the calculated stress intensity factor and K_{IC} is the fracture toughness, assumed to be a rock property. However, it has been recently shown that crack initiation from a borehole can be substantially impacted by finite plasticity (zone of plastic deformation comparable in size to the crack and/or borehole) owing to the fact that the crack does not become “large” compared to the plastic zone until it substantially exceeds the borehole radius (Lecampion 2012), which is beyond the region of modeling interest for sleeve fracture. Indeed, as a broad summary, the analysis to date of sleeve fracturing does not deal with initiation of fracturing, but instead tends to assume presence of initial cracks of rather arbitrary length and with an assumption that LEFM applies from the very beginning.

The working hypothesis of this paper is that consideration of the finite plasticity associated with initiation and growth, including the stress interaction among the growing cracks, will lead to modifications of fracturing pressures and geometries and hence will refine the predictions used for test interpretation.

The approach to modeling finite plasticity associated with fracturing will make use of the classical cohesive zone model, which has been developed by Barenblatt (1962) and Dugdale (1960). This method has been widely applied in simulating fracture process in rock and concrete (Saouma et al. 2003; Segura and Carol 2010; Yao 2012). The cohesive zone model assumes that fracturing is a gradual process where the separation between a pair of cohesive surfaces is controlled by the cohesive traction. Therefore, the computational challenges associated with the stress singularity at the crack tip when using LEFM can be avoided by utilizing cohesive element method. Moreover, implementation of the cohesive elements in a conventional finite element method leads to a relatively straightforward and efficient approach to analyze fracture initiation and propagation behavior.

This study aims to revisit the effect of in-situ stresses on first and second crack initiation and growth under sleeve fracturing conditions. This analysis allows for crack propagation that is not completely brittle elastic, which can be important in light of the fact that the wellbore, initial crack size, and likely size of the plastic zone near the crack tip are all of a comparable scale. For this purpose, a 2D plane-strain model is developed using ABAQUS while cohesive elements are implemented on pre-defined crack trajectories to simulate the possible crack initiation and propagation around the wellbore. Different boundary conditions are considered for field-scale and lab-scale simulation. Indeed, field-scale simulation results indicated that the first crack always initiate at the direction of maximum in-situ stress. However, the second crack can initiate at various direction with different in-situ stresses, which can challenge the general belief that the orientation of second fracture should be perpendicular to the first crack.

2.4 Model Methodology

The numerical simulation provided in this work is developed using the commercial FEM software ABAQUS. The rock matrix is represented by plane-strain elements governed by linear elasticity for an isotropic rock, and the cohesive elements are implemented on pre-defined crack trajectories, as illustrated in Figure 2. Breakage of pre-defined cohesive zone elements generates new cracks. The mechanical deformation of rock formation as well as stress distribution along the wellbore are also coupled together via elasticity equations and the behavior of the cohesive elements.

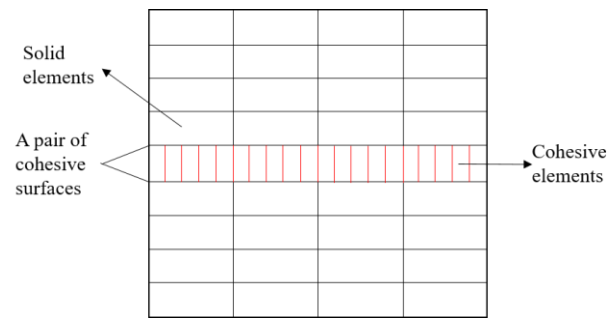


Figure 2 Generic illustration of rock elements connected together by cohesive zone elements on a potential plane of crack growth (after ABAQUS 2011).

The behavior of the cohesive elements follows a prescribed traction-separation law. The traction-separation law defines the relationship between the traction (T) and the displacement (δ) between a pair of cohesive surfaces (i.e. as shown in Figure 2). A bilinear damage evolution model (after Barrenblatt 1962 and Dugdale 1960, see Figure 3) is adopted in this study. This model assumes that the cohesive surfaces follow linear elastic behavior before the traction reaches the cohesive element strength, T_{max} , or the separation displacement exceeds the critical separation at

damage initiation δ_0 . Then, the traction tensor will reduce linearly to zero at the critical separation at complete failure δ_f . The area under this curve gives the critical energy release rate, G_c , which can be related to the fracture toughness of the rock, K_{Ic} , via

$$G_c = \frac{K_{Ic}^2(1-\nu^2)}{E} \quad (2-1)$$

where the E is the Young's modulus and ν is the Poisson's ratio. Additionally, the ratio ($\alpha = \delta_0 / \delta_f$) embodies the relative portion of the region wherein the cohesive element is in elastic deformation compared to the portion in which it is undergoing plastic softening. Moreover, the T_{max} has the similar order with tensile strength of material while they are slightly different with each other. Finally, note that in ABAQUS there is an ability to account for shearing failure and shearing deformation of cohesive elements, which is taken as negligible because crack opening is assumed to be caused by normal traction by setting shearing strength T_s and shearing stiffness K_s to values that exceed their tensile counterparts by several orders of magnitude. Clearly this modeling choice, along with prescribing straight and smooth crack paths, precludes the impact of crack tortuosity, curving, and mixed mode loading. These issues could impact behavior in a practical sense, but, because of the ability to illustrate some important behaviors with a simpler model, this added complexity is left to future investigation.

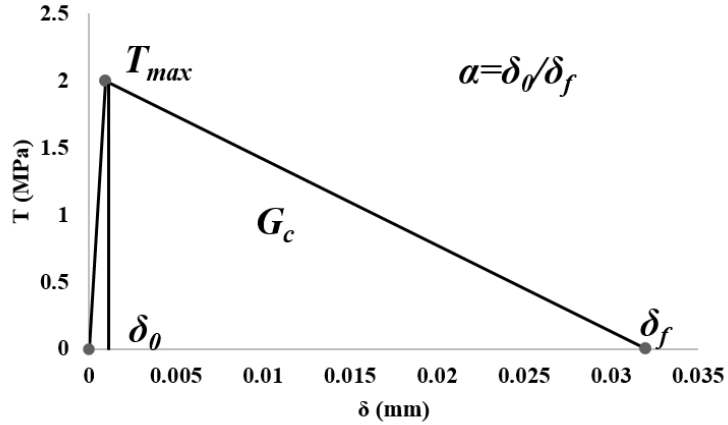


Figure 3 Traction-separation law of cohesive elements (after Barrenblatt 1962 and Dugdale 1960).

2.5 Model Setup

The problem of sleeve fracturing is considered using a plane strain approximation in an isotropic rock with bi-axial in-situ stresses. The plane strain approximation is valid provided that the length of wellbore pressurized by the sleeve is long compared to the wellbore diameter. The model is setup for field-scale and lab-scale models, as described in what follows. Note that in both cases a particular mesh is discussed and presented, and these are chosen after a mesh sensitivity study with various mesh densities confirms that the solution is not mesh dependent.

2.5.1 Field-Scale Model Setup

The geometry of the field-scale model, which considers a vertical borehole subjected to biaxial far-field stresses and internal pressurization, is shown in Figure 4. Infinite elements, which are a built-in feature of ABAQUS, are applied to simulate the infinite domain relevant to a field

test, as shown in Figure 4a. A hole is placed in the center of the domain, representing a pressurized borehole. This hole has 16 pre-defined crack trajectories distributed along the wellbore at angle increments of 22.5° . The cohesive elements are implemented on these pre-defined crack trajectories, as shown in Figure 4b. The length of cohesive element trajectories is 31.25 times as long as the borehole diameter. For most of the cases, the simulated fracture travel 2 to 4 times borehole diameter away from the borehole.

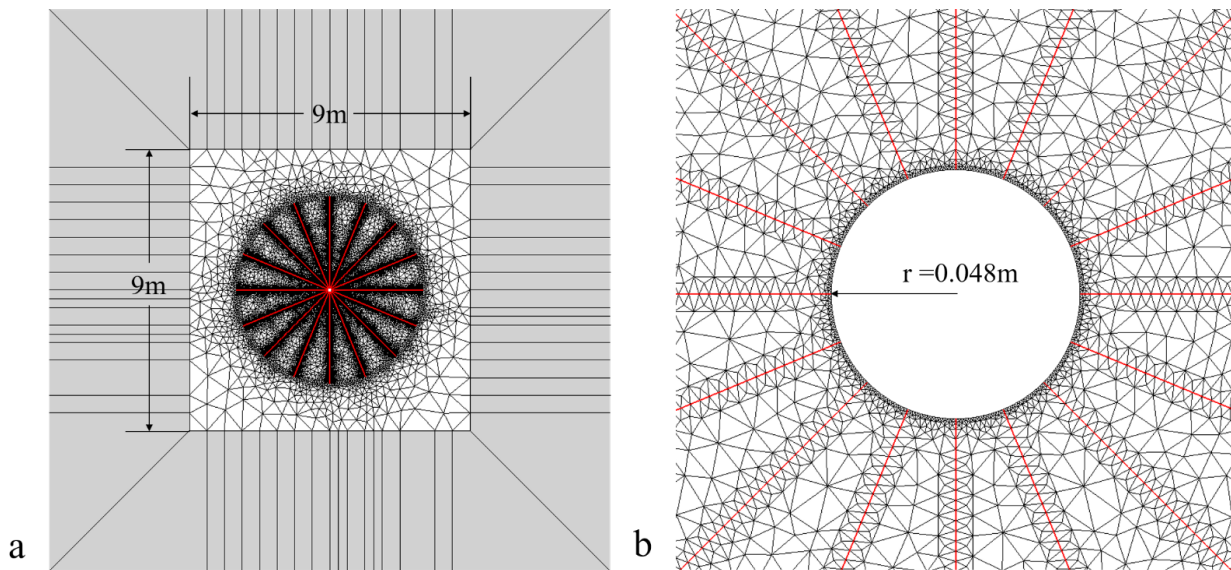


Figure 4 Model setup for field test, showing a) Full model including infinite elements around the model's perimeter, and b) Closer view of borehole with pre-defined crack trajectories.

Having set up the model, a variety of field-scale cases under different combinations of in-situ stresses are considered. Figure 5 shows the biaxial far field loading, where σ_{Hmax} is the maximum in-situ stress and σ_{hmin} is the minimum in-situ stress. Additionally, a pressure loading, p_w , which is made to incrementally increase to simulate sleeve pressurization, is applied around the interior of the borehole. Material properties for both rock elements and cohesive elements are

kept the same for four cases (Table 1) while different combination of in-situ stresses are considered, as given in Table 2.

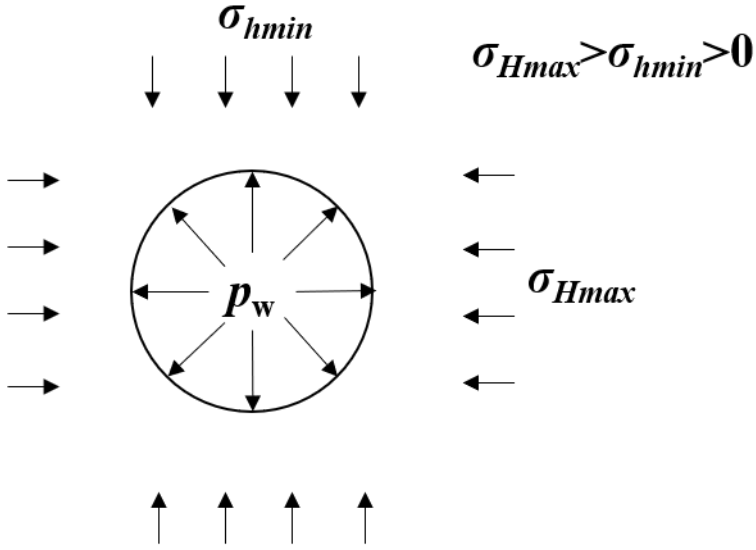


Figure 5 Loading setup for field-scale simulation.

Table 1 Material properties

Solid elements	Young's modulus	20.52GPa
	Poisson' ratio	0.2
Cohesive elements	G_c	32 N/m
	T_{max}	2MPa
	α	0.03

Table 2 In-situ stresses for different cases

	Case 1	Case 2	Case 3	Case 4
σ_{Hmax}	20MPa	15MPa	20MPa	30MPa
σ_{hmin}	10MPa	10MPa	15MPa	10MPa

2.5.2 Lab-Scale Model Setup

The model setup for a lab-scale experiment is generated to replicate an actual block test, and is shown in Figure 6. The loading in the experiments is applied by hydraulic pistons pressing on steel plates which, in turn, transmit the load to the specimen. To simulate this loading, four steel plates are placed on the boundaries of the specimen by defining frictional contact between the specimen and the steel plates wherein the friction coefficient of the contact is set as 0.2. Fixed boundary conditions are applied on the left and bottom plate to avoid rigid motions of the system. To avoid rigid rotation, the centers of the top and bottom plates are fixed in the x direction, and the centers of left and right plates are fixed in the y direction. The area percentage of pressure loading applied on the plate are related to the contact area between the steel plate and the piston used in the actual laboratory setup.

Similar to the field scale model, cohesive elements are distributed along 16 pre-defined planes for potential crack growth. The loads in the two directions are set to generate nominal applied stresses of $\sigma_1 = 2.76\text{MPa}$ and $\sigma_2 = 1.38\text{MPa}$, in order to match a laboratory block test, described later in this paper. Furthermore, rock and cohesive element properties are chosen as in Table 3, with these choices intended to match the properties of the material used in the block experiment.

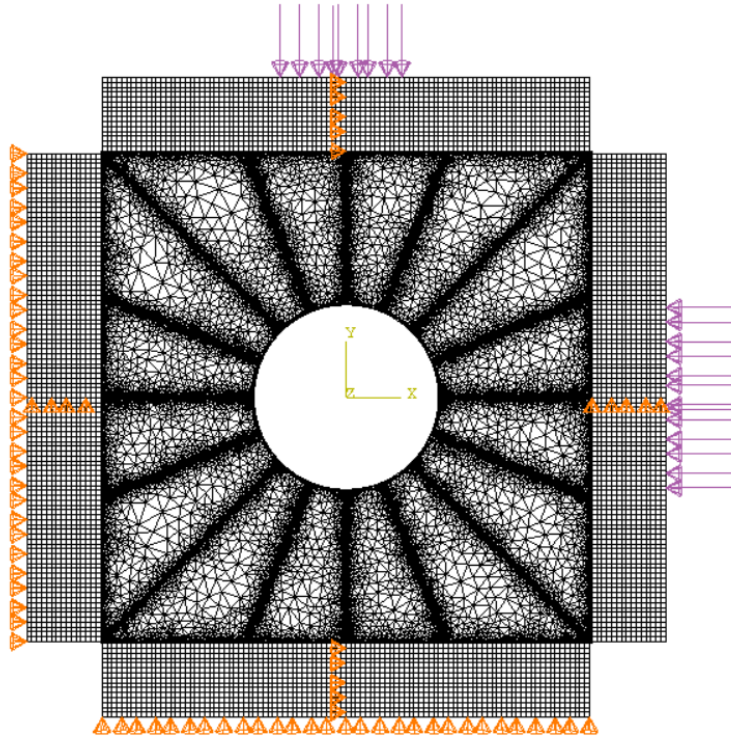


Figure 6 Model setup for the laboratory test.

Table 3 Material Properties

Solid elements	Young's modulus	26.9GPa
	Poisson' ratio	0.2
Cohesive elements	G_c	10.7 N/m
	T_{max}	1.5MPa
	α	0.003

2.6 Validation of Model

2.6.1 Validation of Model with Kirsch's Solution

The first step to validate the numerical model is to benchmark its stress calculation with the solution of the pressurized hole in an infinite elastic domain with stresses on its boundary (“Kirsch’s solution”, after Kirsch 1898), namely

$$\sigma_{rr} = \frac{\sigma_{\infty}}{2} \left[1 - \left(\frac{a}{r} \right)^2 \right] + \frac{\sigma_{\infty}}{2} \left[1 - 4 \left(\frac{a}{r} \right)^2 + \left(\frac{a}{r} \right)^4 \right] \cos 2\theta \quad (2-2)$$

$$\sigma_{\theta\theta} = \frac{\sigma_{\infty}}{2} \left(1 + \left(\frac{a}{r} \right)^2 \right) - \frac{\sigma_{\infty}}{2} \left(1 + 3 \left(\frac{a}{r} \right)^4 \right) \cos 2\theta \quad (2-3)$$

$$\sigma_{\theta\theta} = \frac{\sigma_{\infty}}{2} \left(1 + \left(\frac{a}{r} \right)^2 \right) - \frac{\sigma_{\infty}}{2} \left(1 + 3 \left(\frac{a}{r} \right)^4 \right) \cos 2\theta \quad (2-4)$$

Here, σ_{rr} is radial normal stress, $\sigma_{\theta\theta}$ is circumferential normal stress, and $\tau_{r\theta}$ is radial-circumferential shear stress. In this calibration problem, the hole has radius a with the radial coordinate r and angular coordinate θ . Uniaxial tension is represented as the remote stress σ_{∞} .

The radius of the hole is set as 0.06m and the remote stress σ_{∞} is set as 10MPa. The radial normal stress, circumferential normal stress, and radial-circumferential shear stress are shown along various trajectories in Figure 7.

Because numerical results are found to closely match the benchmark solution at a variety of different θ , here we only show benchmark results at one representative angle, Figure 7. Benchmark results from the Figure 7 show that the numerical simulation results match with Kirsch’s (1898) analytical solution both near the wellbore and in the far field. This successful benchmark demonstrates the validation of the numerical model in computation of stresses and strains for a hole in a bi-axial stress field.

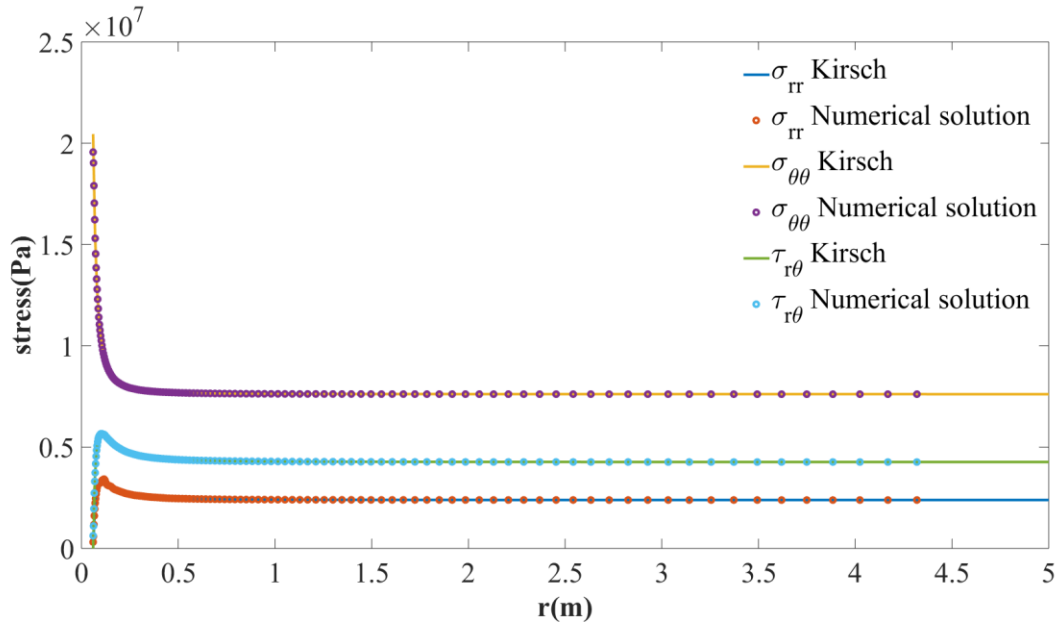


Figure 7 Benchmark of numerical simulation with Kirsch's (1898) solution.

2.6.2 Validation of Model with Laboratory Test

A block test run by Luna Innovations is used to validate the model's predictive ability in lab-scale. The setup of this test is shown in Figure 8. This test used a 0.254m x 0.254m block that was 0.305m long in axial direction of the packer. The central hole has a diameter of 0.095m. A load frame mounted with hydraulic pistons applied bi-axial loading to the block through four steel plates. The applied load resulted in a nominal stress of 2.76 MPa and 1.38 MPa in two orthogonal directions. The tensile strength of the concrete was experimentally found to be 3.19 MPa, and the fracture toughness was experimentally measured to be 0.548MPa m^{1/2}. The Young's modulus of material was 26.9GPa.

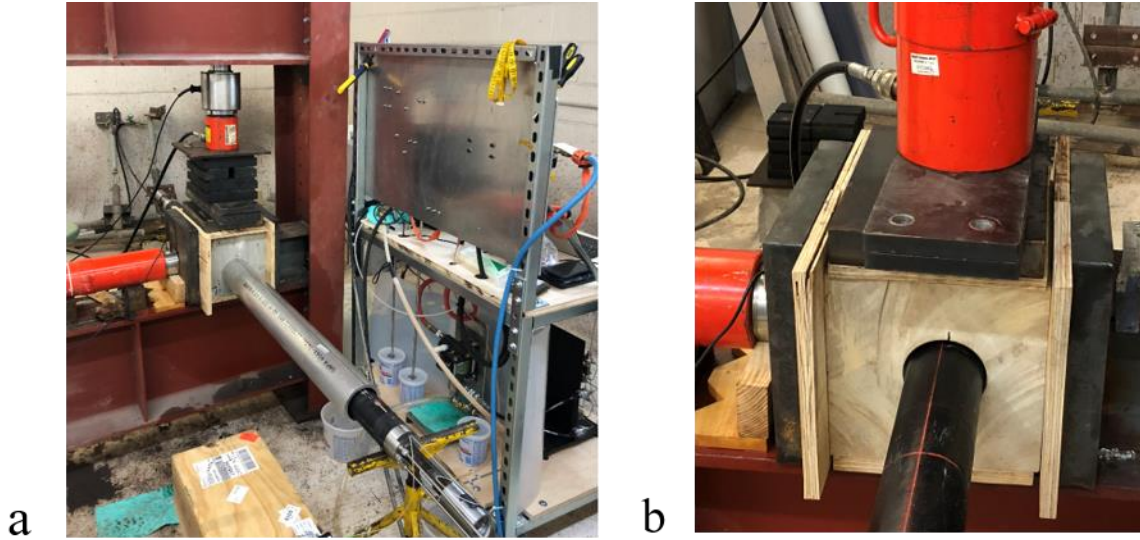


Figure 8 Setup for the laboratory test for: a) Complete setup including pumping equipment with a concrete specimen, note that a constraining metal pipe covered the expandable portion of the sensor assembly that protruded from the rock specimen during inflation; b) Close-up of cored sandstone rock specimen with inflatable sensor assembly inserted.

Figure 9 shows the crack initiation and propagation behavior predicted by the lab-scale numerical model. It is qualitatively similar to the behavior observed in the lab in that a primary crack growth in the plane upon which the smaller stress is acting. After this, upon increasing of the pressure inside the central hole, a secondary crack grows in the plane with angle 67.5° . Then, a tertiary crack initiates in the plane with angle 90° . The other 12 potential planes of crack growth did not show substantial fracturing, also in agreement with a lack of damage observed in the tested block. The crack opening versus pressure loading is plotted in Figure 9, which provides the initiation pressure for the first, second crack and third crack. Indeed, the difference between the initiation pressure of the secondary and tertiary crack is very small. Also, the results from Figure 9 show that the secondary crack has been suppressed by the tertiary crack. Furthermore, a

comparison of initiation pressure for first and second crack between simulation and lab test (Appendix Table 1) indicates reasonable agreement, with the simulation overestimating the pressure for primary crack growth by about 0.4% and overestimating the pressure for secondary crack growth by about 18%.

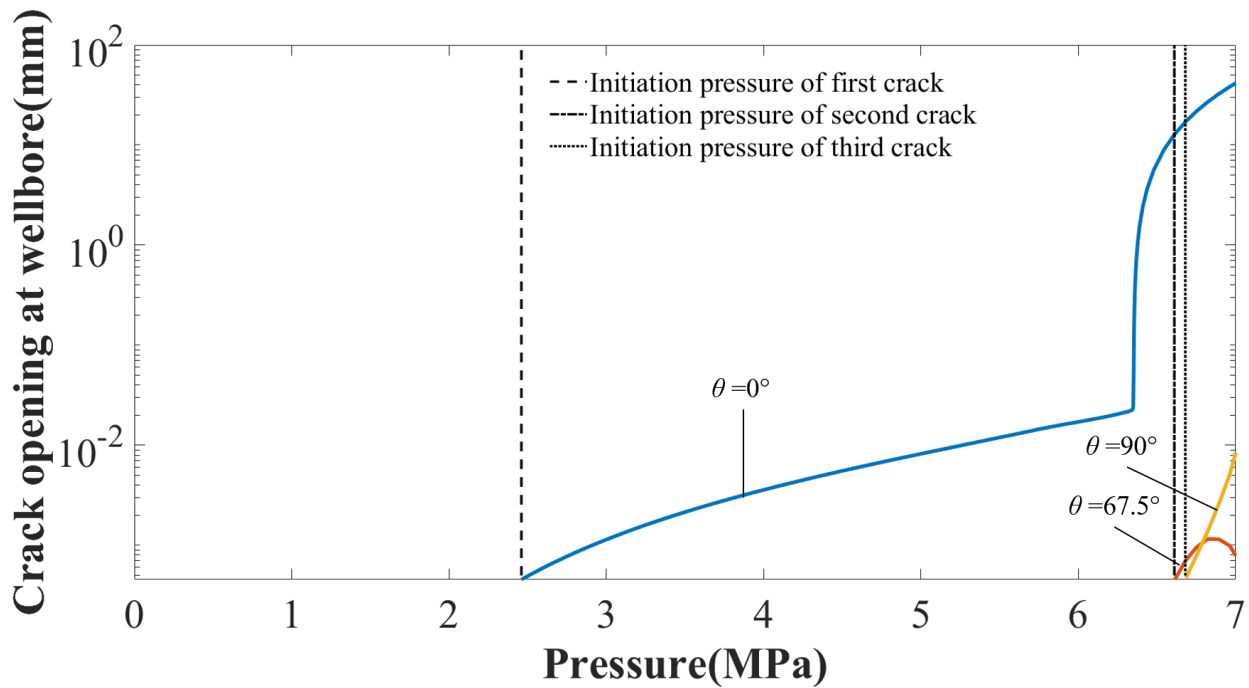


Figure 9 Lab-scale simulation result with ABAQUS finite domain at the correct scale.

A field-scale simulation with same material properties and in-situ stresses with lab experiment assuming that the load application in the lab can be replaced with a far field stress in an infinite domain is also provided in Appendix A to check whether the lab experiment results can predict the field test. More detail parametric study of loading conditions and the cohesive element properties are also discussed in Appendix A.

Finally, it is important to note that the laboratory simulations are observed to be heavily influenced by the details of the boundary conditions of the loading on the finite block. That is to say, using an infinite domain model results in huge difference not only between details of the predicted pressures for crack initiation, but also in the qualitative behavior. Indeed, as will be shown in the sections to come, other orientations of secondary fracture can be favored in the infinite domain models. In the lab-scale simulations, even details such as size of the distributed load (representing the loading piston size) and the thickness of the steel loading platens can substantially impact the results. And, besides being affected by the details of the loading conditions, cohesive element properties were found to be important. In particular, the values of T_{max} , G_c and δ_0 (Table 4) are essentially used as fitting parameters in order to achieve a match to the experiments, as they are both highly influential on the solution and poorly constrained by independent experiments. This final point emphasizes the importance of experiments, even if boundary conditions do not bear precise similarity to far-field stress conditions encountered in the field (as long as the model accounts for these lab-scale boundary conditions).

The key takeaways are therefore threefold. Firstly, the lab-scale model is validated by comparison to the lab experiments. Secondly, if one wishes to use lab experiment results to predict the field test, it is important to use a purpose-built simulator that accounts for the details of the boundary conditions rather than simply assuming that the lab experiments somehow approximate an infinite domain. Finally, lab simulations are sensitive to details of the model, both in terms of precise representation of the load application apparatus and suitable choices of rock and cohesive element properties.

Table 4 Comparison of simulation results with lab test data for the pressure associated with first and second crack initiation.

Initiation pressure	Lab test results	ABAQUS CZM finite domain
1 st crack	2.45MPa	2.46MPa
2 nd crack	5.59MPa	6.61MPa

2.7 Field Scale Simulation Results

Simulation results showing the open cohesive elements for four field-scale cases under different in-situ stresses (from Table 2) are shown in Figure 10. The presented figures show the crack geometry after the initiation of the second fracture, which corresponds in each case to a certain internal borehole pressure (see Figure 10). The first crack always initiates at the direction of maximum in-situ stress for all the four cases. The common assumption is that the second fracture should initiate at the direction perpendicular to the first fracture. This assumption seems to be already challenged in the lab-scale simulation results. However, the results from Figure 10 indicate that in the field-scale the second crack initiates at $\theta=45^\circ$ for Case 1-3, and the orientation of second crack for Case 4 is $\theta=22.5^\circ$. Hence, the simulations predict that the initiation direction of the second fracture can vary depending on the combination of in-situ stresses. In addition, the crack which orients with the opening in direction perpendicular to the first crack for Case 1-3 is the third crack rather than the second crack, which is inconsistent with the most common

assumption of growth direction (with origins in LEFM typically neglecting fracture interaction). Moreover, it can be seen from the Figure 10 that there are also small fractures opening at $\theta=22.5^\circ$ and $\theta=67.5^\circ$ for Case 1-3. However, such cracks are not accounted as the second crack since they have been suppressed by other cracks and cannot appreciably open in order to be resolved in wellbore measurement data, for example in field tests.

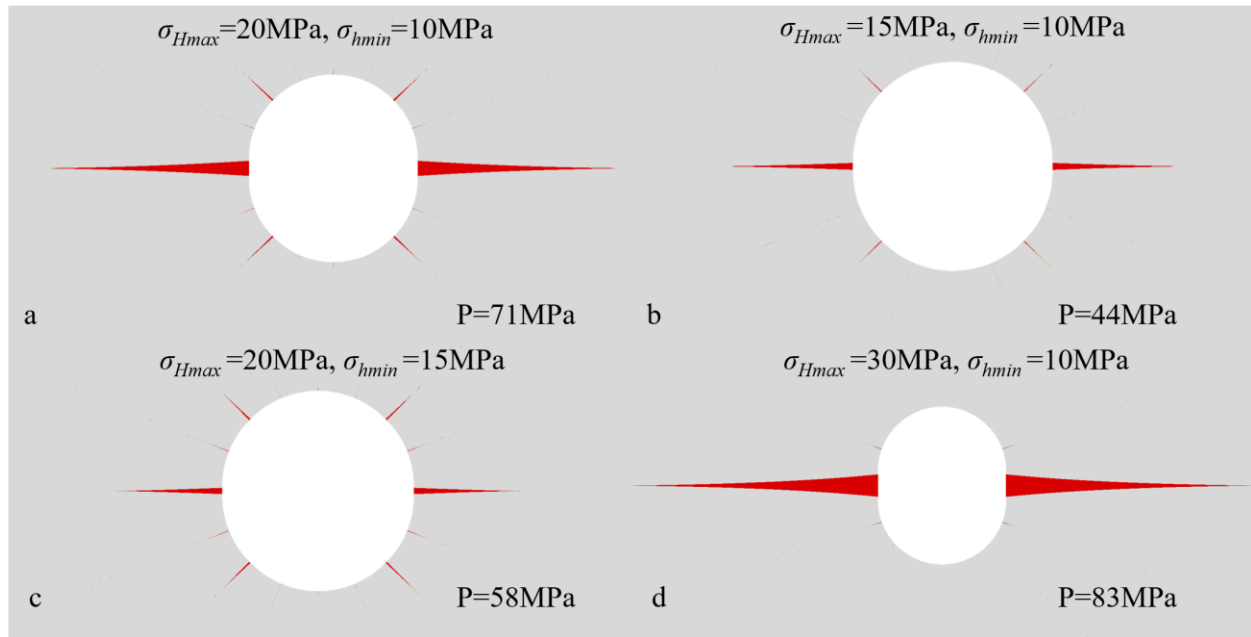


Figure 10 Field-scale simulation results showing the open cohesive elements for: a) Case 1; b) Case 2; c) Case 3; d) Case 4. Deformed cohesive elements are shown at wellbore pressures indicated by P, which are somewhat above the corresponding crack initiation pressures so that the deformed cohesive elements are visible and illustrative of crack growth directions.

The fracture width at the wellbore versus the pressure loading are plotted in Figure 11 to enable further examination of the fracture initiation and propagation behavior. As a point of comparison, Figure 11 also shows predictions of breakdown pressure based on comparison of the circumferential stress at various locations (angles, with 0 corresponding to the direction of the plan

acted upon by the least compressive stress). This prediction is a generalization based on the classical breakdown criterion of Hubbert and Willis (1972), where wellbore pressure leading to rock breakage in a given orientation q , denoted $p_b(q)$, is given by

$$p_b(\theta) = T_{max} + (\sigma_{Hmax} + \sigma_{hmin}) - 2(\sigma_{Hmax} - \sigma_{hmin})\cos 2\theta \quad (2-5)$$

Here T_{max} is the tensile strength of the rock (or, in the model, the cohesive element strength), σ_{Hmax} is the maximum in-situ stress, σ_{hmin} is the minimum in-situ stress, and θ is the angle between the certain crack and the first crack.

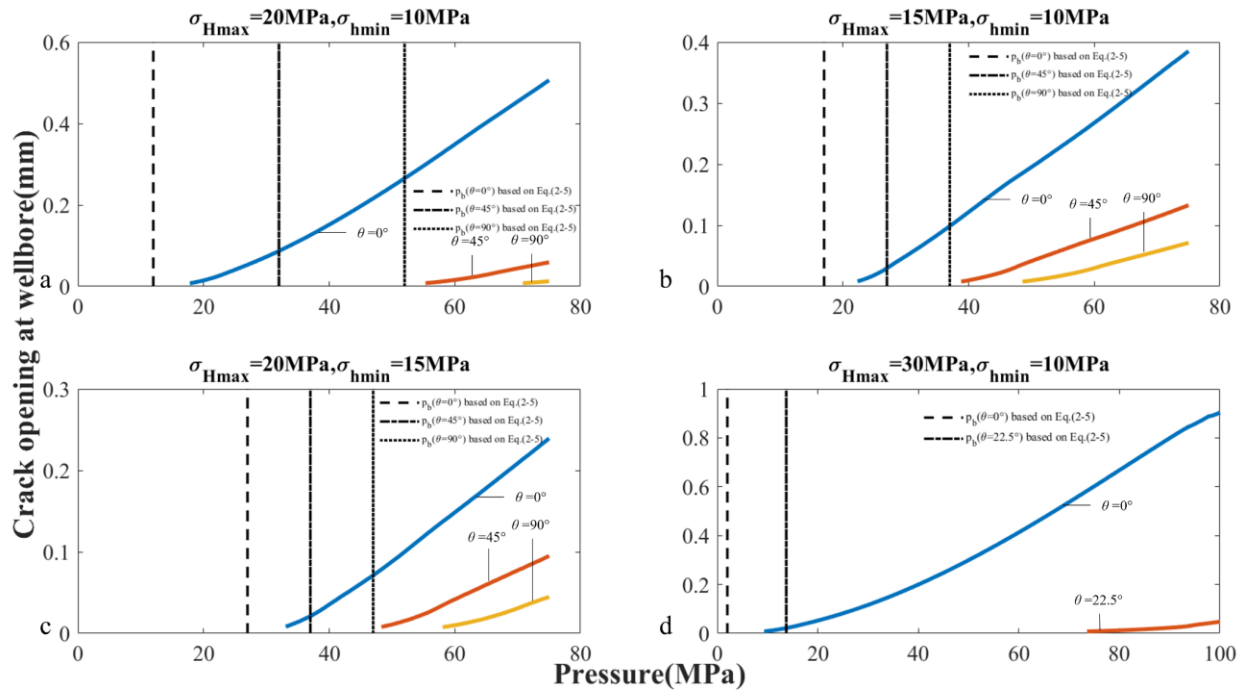


Figure 11 Crack initiation and propagation behavior for field-scale under different in-situ stresses a) Case 1; b) Case 2; c) Case 3; d) Case 4.

Figure 11 shows that the initiation pressure of the first fracture and second fracture is varying with the different combinations of in-situ stresses. In particular, the difference between

the first and the second crack initiation pressure increases with the difference between the maximum and minimum in-situ stress, which also demonstrates the impact of the ratio of in-situ stresses on the fracture initiation behavior. Moreover, the first crack's width is always the largest among all the cracks. In all the cases, the first crack propagates faster before other cracks initiate and more slowly thereafter. However, it is also observed that the growth is steady, lacking sudden jumps in crack length that are predicted as a consequence of the crack length being double-valued for a given pressure at the early stages of growth according to LEFM (as pointed out by Detournay and Jeffrey 1986).

Taken together, field-scale simulation results from Figs. 9 and 10 demonstrate the impact of in-situ stresses on fracture initiation and fracture propagation behaviors. Indeed, as expected, the simulation shows the first fracture always orients to grow in the plane acted upon by the least compressive stress. However, in contrast to prior expectation, the opening direction of the second fracture can vary with different in-situ stress combinations. This variability of the initiation angle of the second crack is due to the existence of the first fracture that can impact the stress distribution and eventually the direction in which damage develops to form a dominant crack. This behavior appears to be tied to the finite plasticity of the cohesive zone, interaction among growing fractures, and ability of the cohesive zone to deform and partially fail under conditions that would not lead to macroscopic crack propagation under the assumptions of LEFM. Additionally, there can be more than two directions of fracturing, as evidenced by crack growth in three orientations evidenced in Figs. 9 and 10. Furthermore, stress analysis based on a generalized form of Hubbert and Willis (1972) (Eq. (2-5)) can give us an apparent lower bound for the actual initiation pressure, noting that the lower bound is closer for the first fracture initiation than for second and third crack initiations. In the end, the most important observation is that the initiation and propagation

behavior of the first and second (and sometimes additional) fractures is sensitive to combination of in-situ stresses, which can be further applied to help estimate the in-situ stresses from the field test data.

2.8 Parametric Study of Cohesive Element Properties

Since the impact of in-situ stresses combination on crack initiation and propagation behavior has been proved by field-scale results, parametric study of cohesive element properties, including α , T_{max} and G_c are further provided under the same combination of in-situ stresses with Case 2 (Table 2). The fracture width at the wellbore versus the pressure loading are plotted in Figure 13,15 and 17 to enable further examination of the fracture initiation and propagation behavior under different α , T_{max} and G_c .

The critical separation ratio α determines the size of fracture process zone for a given cohesive element energy G_c and cohesive element strength T_{max} . Small α ratio means a large portion of the deformation is in the softening range and hence there is a large active fracture process zone.

Simulation results from Figure 12 show that the orientation of the second crack is not varying with different α ratio while the T_{max} and G_c are held to be the same so that only α is varying. Figure 13 shows that the initiation pressure of the first fracture and second fracture are both increasing as the α increases, which also means that the initiation pressure increases as fracture process zone becomes smaller. Additionally, the comparison between the predicted breakdown pressure and the initiation pressure observed from simulation also indicates that the initiation pressure of the first crack and second crack is moving toward the predicted breakdown pressure as

the α ratio becomes smaller. Moreover, the difference of initiation pressure between the first and second crack is increasing as the α ratio increases, which also indicates that the α ratio has more impact on the initiation pressure for the second crack than the first crack.

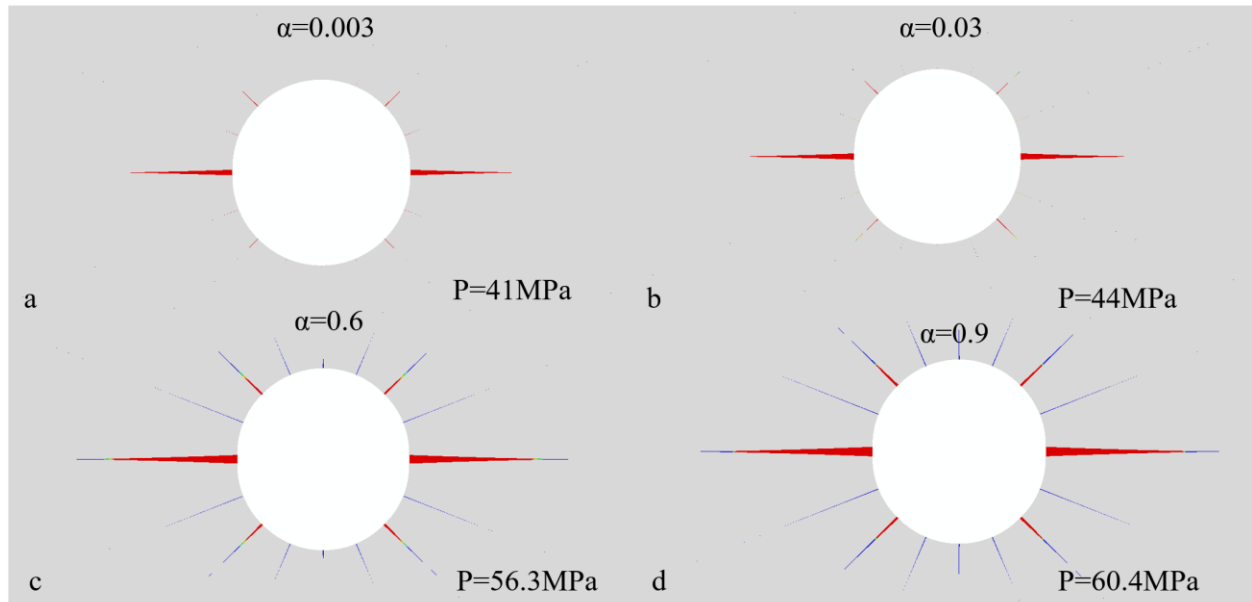


Figure 12 Field-scale simulation results showing the open cohesive elements for: a) $\alpha=0.003$; b) $\alpha=0.03$; c) $\alpha=0.6$; d) $\alpha=0.9$. Deformed cohesive elements are shown at wellbore pressures indicated by P, which are somewhat above the corresponding crack initiation pressures so that the deformed cohesive elements are visible and illustrative of crack growth directions.

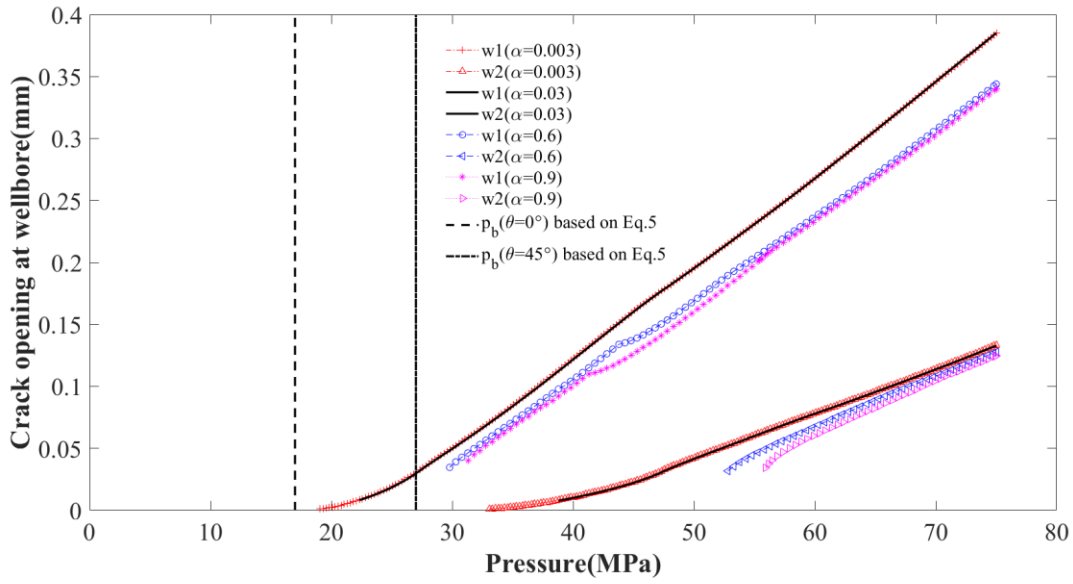


Figure 13 Crack initiation and propagation behavior for field-scale under different α (recall w1 and w2 are the crack opening at the wellbore for the first and secondary crack, respectively).

Simulation results from Figure 14 indicate that the change of T_{max} has no impact on the orientation of the second crack for cases in which α ratio and G_c are held to be the same so that only T_{max} is varying. Figure 15 shows that the initiation pressure of the first fracture and second fracture does not change much as T_{max} increases from 1MPa to 4MPa. However, the initiation pressure for the $T_{max} = 10$ MPa case does have a little difference with other three since there is a sudden jump in crack opening when crack starts to initiate. In all the cases, the first crack propagates faster before other cracks initiate and more slowly thereafter. Here we define the corresponding pressure at which the propagation speed of crack started to slow down as the “inflection pressure”. Indeed, it can be obtained from the Figure 15 that the inflection pressure for the first crack is decreasing as T_{max} increases, while the inflection pressure for the second crack is increasing as T_{max} increases. Note that for cases with the smallest values of T_{max} , there is no

observed inflection point, which is also why there is no inflection observed in the cases presented for varying α ratio (Figure 13).

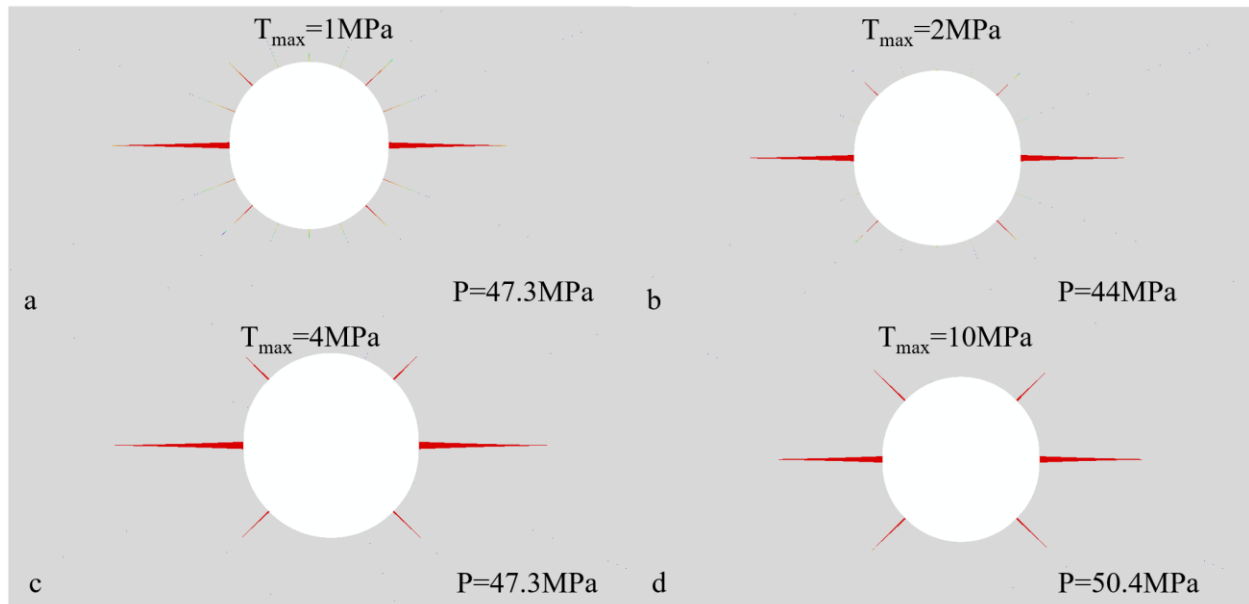


Figure 14 Field-scale simulation results showing the open cohesive elements for: a) $T_{max} = 1\text{MPa}$; b) $T_{max} = 2\text{MPa}$; c) $T_{max} = 4\text{MPa}$; d) $T_{max} = 10\text{MPa}$. Deformed cohesive elements are shown at wellbore pressures indicated by P, which are somewhat above the corresponding crack initiation pressures so that the deformed cohesive elements are visible and illustrative of crack growth directions.

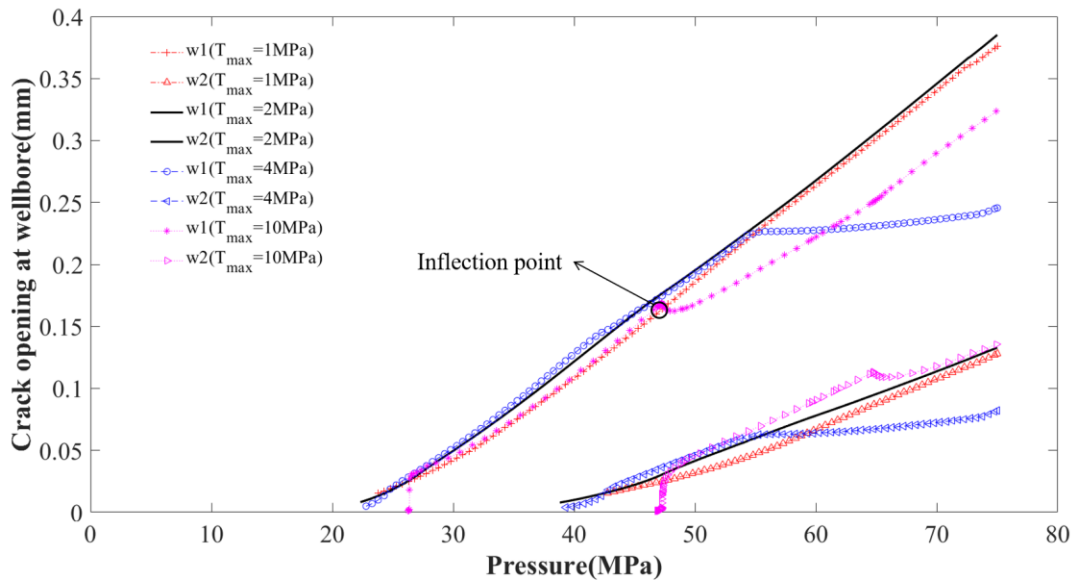


Figure 15 Crack initiation and propagation behavior for field-scale for different T_{max} , with the inflection point for one case labelled as an illustration.

Simulation results showing the open cohesive elements for four field-scale cases under different G_c are shown in Figure 16 while critical separation ratio α and cohesive element strength T_{max} are held to be the same so that only G_c is varying. The presented figures show the crack geometry after the initiation of the second fracture, which corresponds in each case to a certain internal borehole pressure (see Figure 16). The first crack always initiates at the direction of maximum in-situ stress for all the four cases. However, the results from Figure 16 indicate that the second crack initiates at $\theta=22.5^\circ$ for $G_c=8$ N/m, and the orientation of second crack for $G_c=16, 32$ and 64 N/m is $\theta=45^\circ$. Therefore, the simulations predict that the initiation direction of the second fracture can vary depending on the G_c value. Since G_c can be related to the fracture toughness of the material (see Eq. (2-1)), it can also be predicted that the initiation orientation for the second crack can vary with different fracture toughness. Hence, this prediction also challenges

the common assumption that the second fracture should initiate at the direction perpendicular to the first fracture.

Figure 17 shows that the initiation pressure of the first fracture and second fracture are both increasing as the G_c increases. The initiation pressure of the first crack and second crack in moving toward the predicted breakdown pressure as the G_c becomes smaller, which also means that material with a lower fracture toughness tends to have an initiation pressure closer to the lower bound for both first and second crack. Additionally, the inflection pressure for both the first and second fracture is increasing as the G_c increases. Furthermore, for the largest value of G_c , the inflection pressure is not observed.

Taken together, field-scale simulation results from Figs. 11-16 demonstrate the impact of cohesive element properties on fracture initiation and fracture propagation behaviors. Indeed, as expected, the simulation shows that critical separation ratio α and cohesive element strength T_{max} have no impact on the opening direction of the second fracture. For the cohesive element energy, G_c can only change the initiation direction of the second crack when it is small enough. However, in contrast to the expectation, the fracture initiation and propagation behavior can vary with different cohesive element properties. This variability should be considered in selecting proper cohesive element properties for field-scale simulation. In order to select proper input, one suggestion is to align the cohesive element properties to the material properties. Accordingly, it is better to define a small α for the material with larger fracture process zone and a large α for the material with small fracture process zone while the tensile strength and fracture toughness of material can give a guideline for selecting T_{max} and G_c . Additionally, the inflection pressure which has been proved to be sensitive to the combination of cohesive element properties can be further

applied to help select the cohesive element properties from the field test data assuming that such inflection point can be observed from field test data.

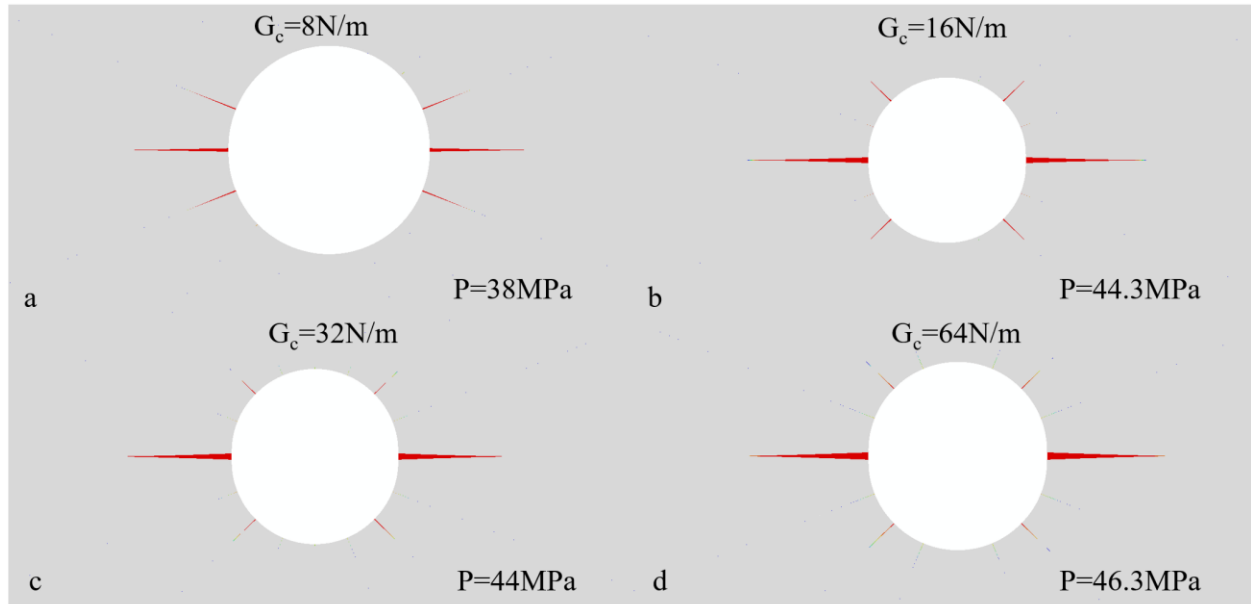


Figure 16 Field-scale simulation results showing the open cohesive elements for: a) $G_c = 8\text{N/m}$; b) $G_c = 16\text{N/m}$; c) $G_c = 32\text{N/m}$; d) $G_c = 64\text{N/m}$. Deformed cohesive elements are shown at wellbore pressures indicated by P , which are somewhat above the corresponding crack initiation pressures so that the deformed cohesive elements are visible and illustrative of crack growth directions.

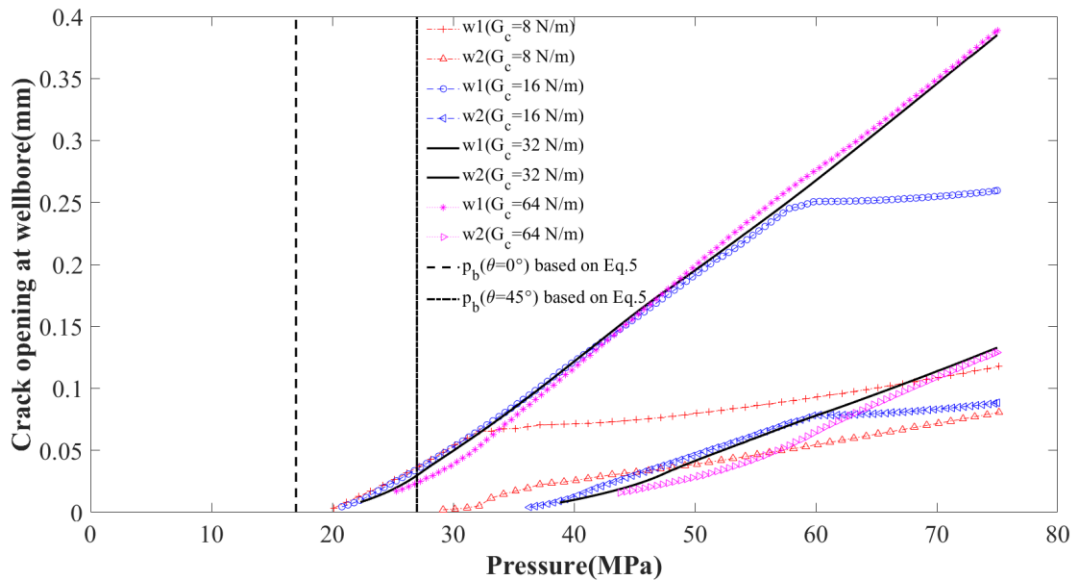


Figure 17 Crack initiation and propagation behavior for field-scale for different G_c .

2.9 Displacements Around the Wellbore

In the field, the strain around the wellbore can be measured using distributed fiber optic sensing (Ohanian 2019). Integration of strain can provide the displacement around the wellbore. Therefore, it is important to analyze the expected wellbore displacement behavior under different pressure loading based on numerical simulation results.

Here, Case 2 is selected to present examples of circumferential displacement u_θ around the wellbore at three different internal borehole pressures, along with open cohesive elements, in Figure 18. Figure 18a shows how circumferential displacement distributes along the wellbore before any crack initiates, where the wellbore displacement obtained from the numerical solution matches the solution of Kirsch (1898) perfectly because there is no crack initiation at $P=10.15$ MPa. As pressure increases, the fractures start to initiate. A small deviation from the Kirsch

solution can be seen from Figure 18b, which is due to the initiation of the first fracture. Finally, the deviation from the solution of Kirsch (1898) shown in Figure 18c is substantial due to fracture initiation and propagation. Therefore, the deviation of wellbore displacement from the Kirsch solution due to the crack initiation can be captured by the simulation, which can be further applied to interpret the initiation pressure and location of fractures based on field test data.

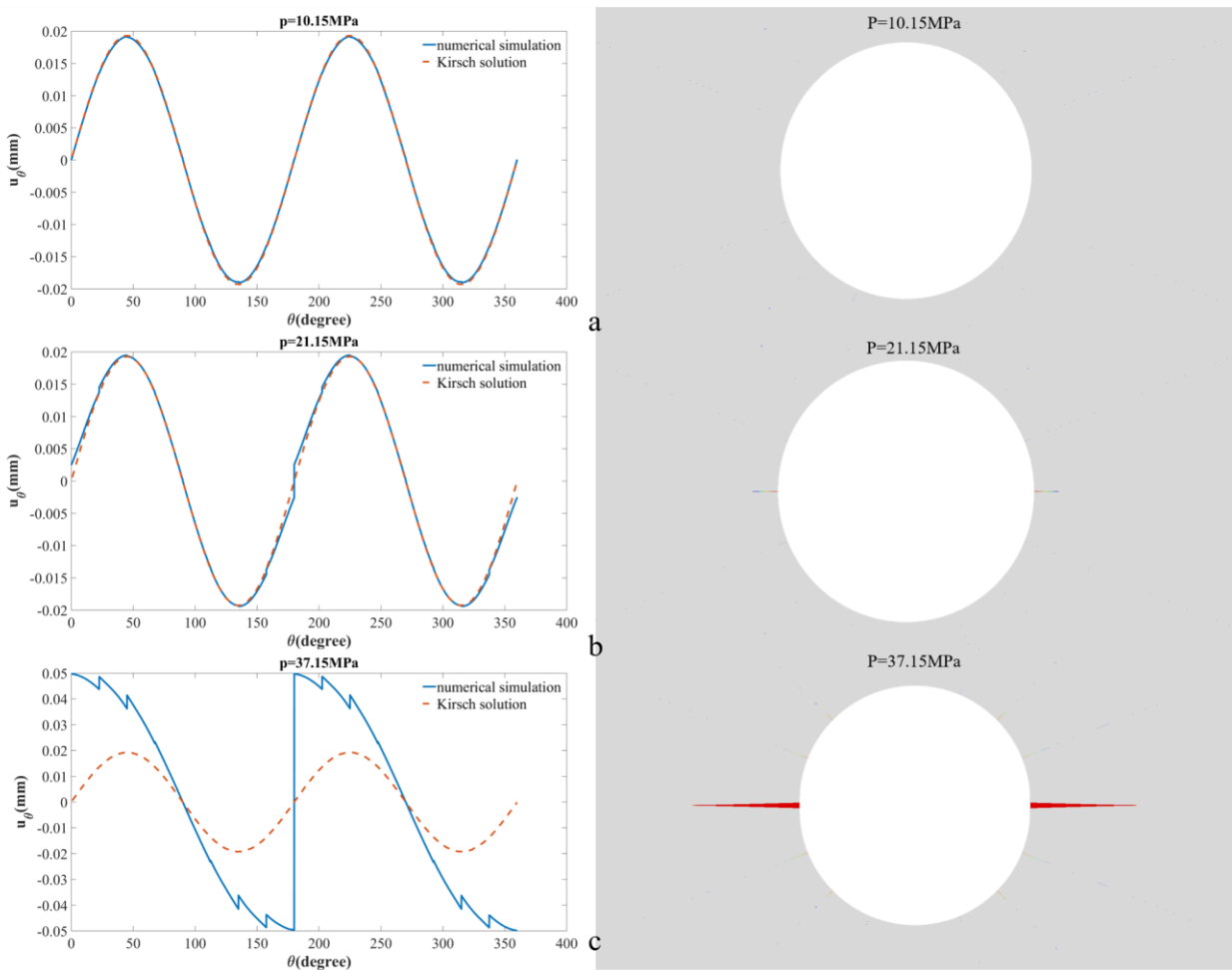


Figure 18 Wellbore circumferential displacement and its corresponding simulation results showing the open cohesive elements for a) P=10.15MPa; b) P=21.15MPa; c) P=37.15MPa.

2.10 Specific Field Scale Case with Nearly Equal In-Situ Stress

In previous sections, the maximum horizontal stress is considered substantially larger than the minimum horizontal stress (relative to an assumed-vertical wellbore orientation) for the field scale cases. However, there is a possibility in the actual field that the maximum horizontal stress is nearly equal to the minimum horizontal stress. Figs. 18 and 19 show the field scale simulation results for one case with the same maximum and minimum horizontal stresses. Material properties for both rock elements and cohesive elements for this case are given in Table 2. These simulation results indicate that all the cracks initiate at the same internal pressure (see Figure 19a). As the wellbore pressure increases, some fractures become dominant while the others are suppressed (see Figure 19b), which further demonstrates the crack interaction affect among all the cracks. The fracture width at the wellbore versus the pressure loading are plotted in Figure 20, thereby showing again that the initiation pressure of cracks at different orientations is the same. The crack width of all the crack are also the same at the crack initiation period. As pressure increases, crack width corresponding to crack at $\theta=22.5^\circ$ and 67.5° keeps increasing while the crack width corresponding to crack at $\theta=0^\circ$, 45° and 90° starts to decrease.

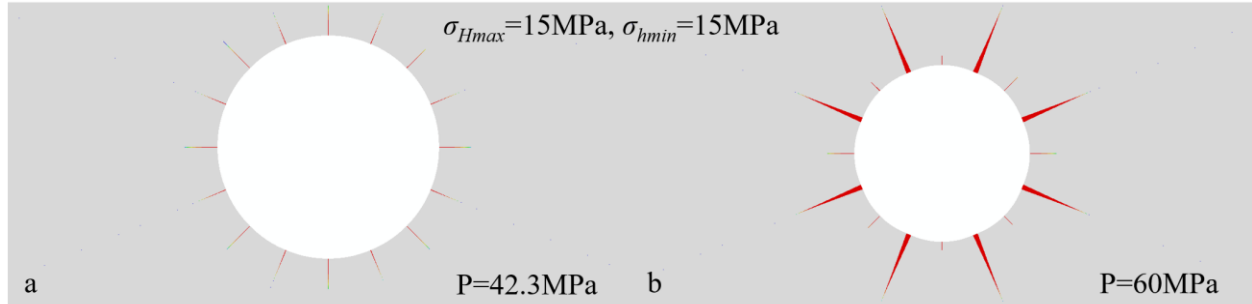


Figure 19 Field-scale simulation results showing the open cohesive elements for case with equal in-situ stresses: a) initiation period; b) propagation period. Deformed cohesive elements are shown at wellbore pressures indicated by P, which are somewhat above the corresponding crack initiation pressures so that the deformed cohesive elements are visible and illustrative of crack growth directions.

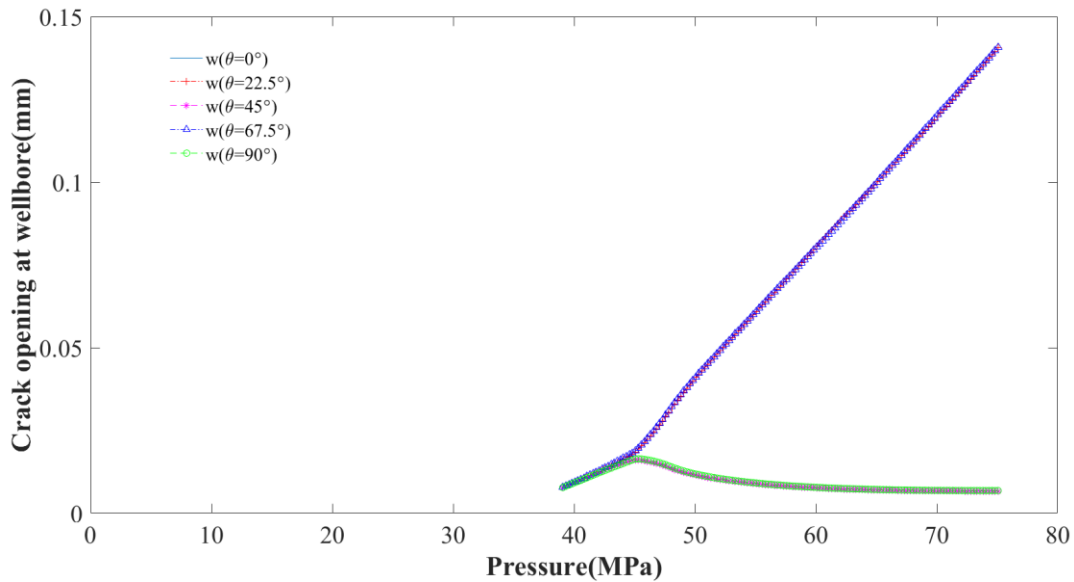


Figure 20 Crack initiation and propagation behavior for field-scale with equal in-situ stress.

While the phenomenon that all the cracks initiate at the same pressure is in one sense to be expected with exactly equal horizontal stresses, repeated simulations show similar behavior over the range $0.93 < \sigma_{hmin} / \sigma_{Hmax} \leq 1$. This result can be further applied to help estimate the in-situ stresses from the field test data, namely, that if field show that there are several cracks initiating at

the same internal pressure, the ratio of horizontal stresses is likely to be in the range $0.93 < \sigma_{hmin} / \sigma_{Hmax} \leq 1$.

2.11 Discussion

Numerical simulation of sleeve fracturing using cohesive zone (CZ) elements leads to identification of behaviors that are not captured by LEFM simulation or elastic stress analysis. Most notably, when stress analysis and LEFM based simulation analyze secondary crack initiation, the conclusion is always that the second crack will initiate perpendicular to the first crack. In fact, these past results are somewhat nuanced. Indeed, LEFM simulation of Chandler (1989) show a period after primary crack growth where the largest stress intensity factor (SIF) corresponds to fractures at angles less than 90 degrees from the primary crack. However, in LEFM there is zero crack extension as long as the SIF remains below the fracture toughness. In contrast, CZ-based simulations show that these periods during pressurization can generate plastic deformation and crack opening at angles other than 90 degrees to the primary crack. Furthermore, CZ-based simulation is the first to indicate potential for crack growth in more than two directions.

Besides leading to recognition of crack initiation and growth at angles other than 90 degrees to the primary crack, CZ modeling demonstrates that details of the plastic deformation behavior can impact on the pressures at which crack growth occurs. Perhaps most strikingly, the borehole pressure leading to both primary and secondary crack initiation and growth increases with increasing α ratio. Recall that large α ratio indicates that a smaller portion of the traction separation law is in the softening curve. So, the smallest initiation pressures correspond to the

lowest values of α ratio, indicating that a material that transitions to softening early in its deformation history will have different crack initiation pressures to one that remains elastic until it undergoes relatively sudden plastic softening. Furthermore, the results show that for cases with large active process zone, the initiation pressures are closer to those predicted based on comparison of Kirsch solution stresses (Eq. (2-5)) to a nominal material tensile strength. For materials with smaller active process zones, there is a higher range of pressures for which the crack does not initiate, after which the failure is more sudden. Hence, the apparent initiation pressure – i.e. the first pressure with observable crack growth – is higher for materials tending to have a smaller active process zone.

The issue of dependence on process zone size clearly raises the discussion of the measure by which a process zone is considered “large” or “small”. In this regard, the present work points to a size effect, with a transition in behavior experienced as intrinsic material length scale(s) is/are varied relative to structural length scale(s) (Bazant and Planas 1997). Hence the behavior transition should be understood to occur as a typical process zone size varies compared to the borehole size. Such a size effect has been explored in detail for hydraulic fracture initiation by Lecampion (2012) and comprises an important direction of future work for sleeve fracturing, where the introduction of multiple fractures propagating and interacting with one another creates challenges when it comes to defining a single structural length scale.

Finally, simulations accounting for both infinite domain and finite domain show substantial differences in both initiation pressures and in secondary and tertiary fracture growth. Because it is typically impractical to achieve the hole size to block size ratio of (1/10) needed to achieve behavior converging to a biaxially-stressed infinite domain, laboratory block test interpretation

should make use of models that account for both the finite specimen size and the details of load application including loading piston size and thickness of the loading platens.

2.12 Conclusion

A new numerical simulation model using plane-strain cohesive zone elements is carried out to investigate the fracture initiation and propagation behavior for sleeve fracturing problem. The model has been validated by both analytical solution and a laboratory test. While laboratory test results were shown to be highly sensitive to the manner of load application and block size, by accounting for these details it is possible to obtain a reasonable match with experiments in both fracturing geometry (i.e. orientation of the secondary fracture) and the borehole pressure leading to both primary and secondary initiation. This match requires some adjustment of CZ properties, and emphasizes the usefulness of such block experiments for model calibration to the particulars of the failure of given materials.

The CZ simulations bear similarity to predictions based on LEFM in the orientation of the initial crack growth, but differ in some marked ways. Simulation results for the field-scale model indicate that the first crack initiates and grows steadily, without an instantaneous jump (in contrast to LEFM), and it always orients to grow along the plane acted upon by the least compressive in-situ stress (consistent with LEFM) for $0 < \sigma_{hmin} / \sigma_{Hmax} \leq 0.93$. For cases with very similar horizontal stresses ($0.93 < \sigma_{hmin} / \sigma_{Hmax} \leq 1$), all the cracks initiate at the same internal pressure. The initiation pressure is also shown to be similar to, but somewhat greater than, predictions based on elastic stress analysis and comparison of the computed stress with a material tensile strength. The

cohesive zone properties impact this deviation from the initiation predicted through stress analysis, with the largest deviation occurring when the traction separation law corresponds to a material that is elastic through most of its loading and transitions suddenly to plastic softening before total failure occurs. On the other hand, a material that slowly softens after the traction reaches a nominal tensile strength most closely matches to the solution based on stress analysis around the borehole.

In contrast to the consistent orientation of the first fracture, the opening direction of the second (and subsequent) fractures is shown to vary with different in-situ stress combinations and CZ properties (in contrast to LEFM). Furthermore, the initiation pressure and location of fractures is systematically impacted by the in-situ stress conditions, pointing to a significant potential that simulations using cohesive elements can be used to interpret field test data leading eventually to estimation of both the minimum and maximum horizontal far-field stress acting on a vertical wellbore.

In summary, CZ simulations predict behavior with potential diagnostic importance for prediction of stresses, both minimum and maximum, based on data from sleeve fracturing experiments. Furthermore, these simulations set the stage for renewed efforts in sleeve fracturing for stress estimation. However, the key behaviors are complex and pertain to details of wellbore deformation, likely with relatively little discretionary ability to be provided by packer pressure and volume data alone. Hence, future directions in sleeve fracturing should be guided by these results and hence should pursue measurement of wellbore deformation with high azimuthal resolution in order to detect subtle crack growth events at all angles around the borehole. In this way, it is promising that minimum and maximum stresses can be estimated with unprecedented precision.

3.0 An Inversion Algorithm to Estimate Maximum and Minimum Horizontal Stress Based on Field Test Data for Sleeve Fracturing

3.1 Preamble

This chapter comprises a preprint of Huang et al. (2021b). In this chapter, a new inversion algorithm is developed to estimate the maximum and minimum horizontal stress with application of experimental data from sleeve fracturing experiments. The algorithm is developed by analyzing the crack initiation, propagation and interaction behavior between primary and secondary cracks based on the numerical simulation carried out in chapter 2. The Simulations using FEM with Cohesive Zone elements predict inflection points in the wellbore deformation that enable straightforward identification of 5 key quantities that comprise the inputs to the inversion algorithm. The algorithm has been validated using 100 sets of synthetic data generated by the FEM-CZ model while most cases showing agreement between the estimated and actual values of both minimum and maximum horizontal stress within a few percent.

3.2 Chapter Summary

An algorithm is developed to estimate maximum and minimum horizontal stress using experimental data from sleeve fracturing experiments. The algorithm is developed by analyzing the crack initiation, propagation and interaction behavior between primary and secondary cracks based on the Finite Element Method with Cohesive Zone elements. Five key quantities can be

obtained from data curves and are related to comprise the basis of the algorithm in a manner consistent with an approximate model based on stress analysis around the borehole. The algorithm has been validated by 100 synthetic data cases covering various parameter combinations. Moreover, quantifying the degree of uncertainty in the stress prediction indicates strongest dependence on detecting when the borehole deformation from the first fracture(s) is impacted by growth of secondary fracture(s). Validity based on simulated data motivates new methods for high resolution strain sensing during sleeve fracturing especially for the purpose of accurately detecting secondary fracture initiation.

3.3 Introduction

Knowledge of in-situ stresses is important as this information is widely applied across the Earth Sciences and Geo-Engineering. Fundamentally, the in-situ stress can be represented by three principal stresses and their orientations. Vertical stress is typically taken as one of the principal stresses and is usually estimated based on integration of the density of the overburden. The minimum stress is routinely estimated based on a variety of well-established tests. However, it is substantially more difficult to quantify the magnitude of maximum horizontal stress (σ_{Hmax}). This is because fracture-based testing methods (e.g. Haimson and Cornet 2003) typically depend most directly on minimum stress, because the first fractures to open are opposed by the least compressive stress. Quantifying maximum stress therefore relies on ability to observe and interpret more subtle and/or subsequent details of fracture initiation and growth.

Among a variety of methods proposed and applied to quantify both minimum and maximum horizontal stress, (e.g. Moos and Zoback 1990; Zoback et al. 2003; Hickman and

Zoback 2004; Stephansson 1983; Serata et al. 1992), the so-called sleeve fracturing method is promising but still relatively unproven, especially for estimation of the maximum horizontal stress. The approach resembles hydraulic fracturing-based methods in that a borehole is pressurized until evidence of fracturing is detected. However, by hydraulically isolating the wellbore and applying pressure through an inflatable packer (Stephansson 1983; Serata et al. 1992, see Figure 21), sleeve fracturing has the advantages of removing uncertainty in the interpretation that arises from fluid penetration into the surrounding rock and preventing rapid fluid loss to the first fracture(s) thereby increasing the opportunity for secondary fracture(s) to initiate.

Secondary fracture initiation is essential to estimation of the maximum horizontal stress (Detournay and Jeffrey 1986). However, difficulties arise both in detection of secondary fracture initiation and in the analysis. The advent of distributed strain sensing using optical fibers, and the ability to embed such distributed strain sensors in the inflatable packer, holds the potential to overcome the limitation of secondary fracture detection (Ohanian 2019, Ohanian et al. 2021).

Even with such emerging technologies for obtaining data, previous approaches to estimate the in-situ stresses from sleeve fracturing tests are typically based on linear elastic fracture mechanics (LEFM) or elastic stress analysis. These approaches also do not include details of wellbore deformation, instead focusing on wellbore pressure and volume relationships that comprised the data previously available from sleeve fracturing tests (e.g. Chandler 1989, Serata et al. 1992, Charsley et al. 2003). Hence, new analysis is needed to leverage distributed fiber optic strain sensing in sleeve fracturing. Furthermore, such analysis should not be constrained by the assumptions of LEFM, especially that LEFM requires assumption that plasticity is confined to a region that is small relative to ad-hoc flaw(s) introduced near the wellbore in order to compute a stress intensity factor for comparison to a fracture toughness, which is assumed to be an intrinsic

property of the rock. In reality, the region of plasticity is expected to be of a similar order to the wellbore size, and therefore the small-scale yielding assumption of LEFM is typically violated for fracture initiation from a wellbore (Lecampion 2012). The capabilities for FEM framework to simulate hydraulic fracturing have been validated by Zielonka et. al. (2014) and Arndt et. al. (2015). This study aims to overcome limitations of LEFM analysis by use of Cohesive Zone elements deployed within a Finite Element framework, and to then provide a rapid and sufficiently accurate method to estimate both maximum and minimum horizontal stress from sleeve fracturing data.

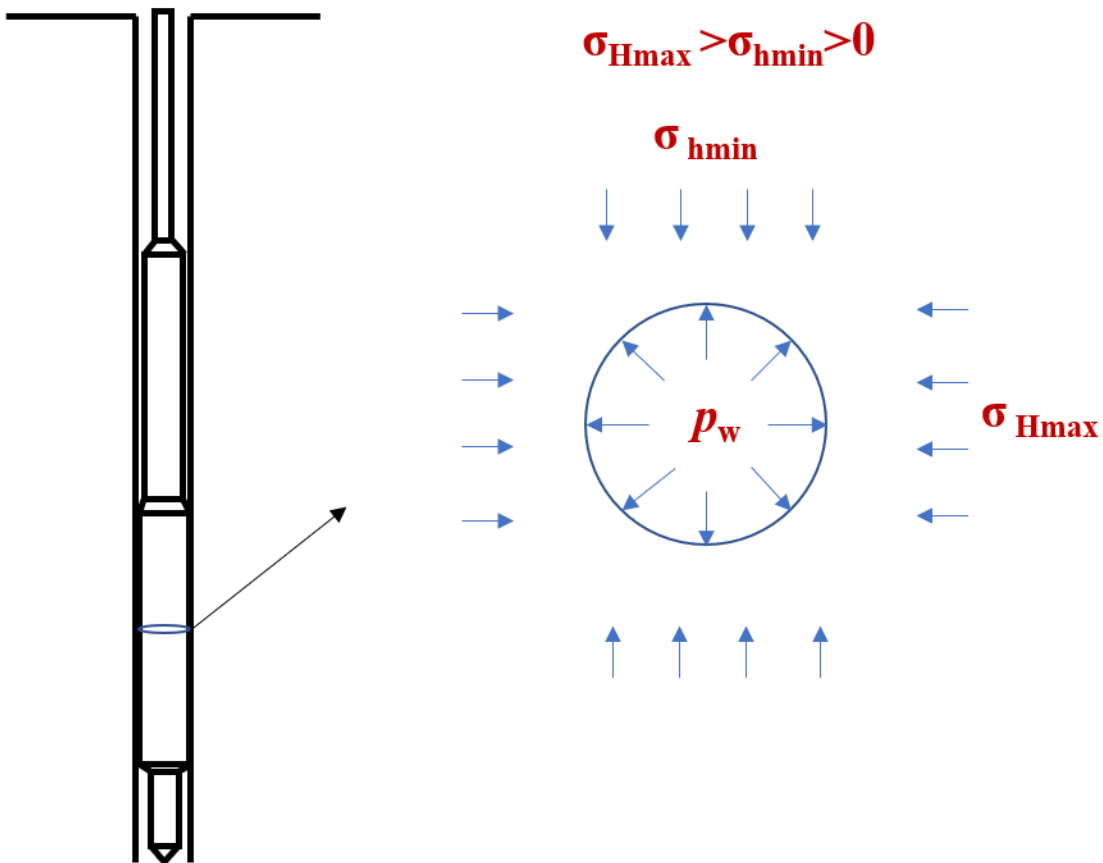


Figure 21 Sketch of the sleeve fracturing technique.

3.4 Identify Algorithm Inputs from Data

In previous work, Huang et al. (2021a) analyzed the crack initiation and propagation behavior for primary and secondary cracks under different combinations of in-situ stresses. In brief, the 2D plane-strain model is developed using ABAQUS while Cohesive Zone elements are implemented on pre-defined crack trajectories to simulate the possible crack initiation and propagation around the wellbore. Details of the model setup are provided in Section 2.5 with inputs described in Table 5. Based on simulations, the derivative of crack width with respect to internal pressure versus the internal pressure is plotted for an illustrative case, shown in Figure 22a. Four inflection points are labelled and are given by:

- 1) The derivative curve showing the propagation behavior of the first crack has one concave point (Point 1 labelled in the Figure 22a) before the initiation of the secondary crack. Note that the Point 1 is not the same as P_I , which is the pressure corresponding to the initiation of the primary crack (as shown in Figure 22b).
- 2) As pressure loading increases, the secondary crack starts to initiate. Then, the derivative curve of the first crack presents a bump point (Point 2 labelled in the Figure 22a) near the initiation pressure of the secondary crack.
- 3) A concave point (Point 3 labelled in the Figure 22a) appears in the derivative curve for the first crack as the secondary crack propagates.
- 4) Finally, the derivative curve showing propagation behavior of the secondary crack has one bump point (Point 4 labelled in the Figure 22a). Notably, Point 3 has the same corresponding pressure with Point 4.

Table 5 Material properties and in-situ stress

Solid elements	Young's modulus	E_{rock}	20.52GPa
	Poisson' ratio	ν	0.2
Cohesive elements	Cohesive element energy	G_c	32N/m
	Cohesive element strength	T_{max}	2MPa
	Critical separation ratio	α	0.03
In-situ stress	Maximum horizontal stress	σ_{Hmax}	15MPa
	Minimum horizontal stress	σ_{hmin}	10MPa

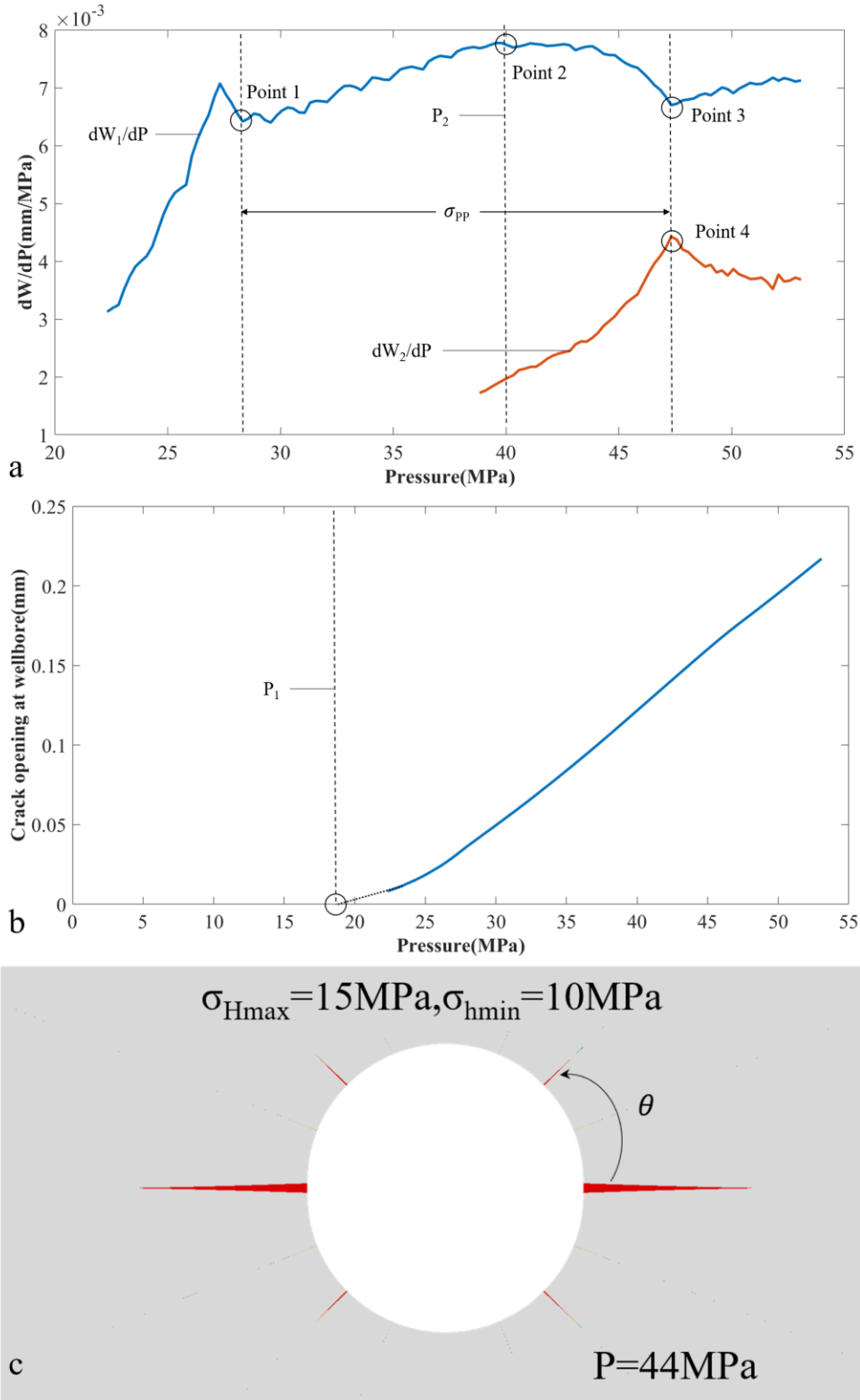


Figure 22 Data curves with inflection points and key quantities labelled for one representative case showing:

a) P_2 and σ_{PP} ; b) P_1 ; c) θ , the angle between first and secondary cracks.

Therefore, two quantities P_2 and σ_{PP} are defined to describe the pressures corresponding to these inflection points, as shown in Figure 22a. These two quantities appear to be tied to the fracture interaction behavior since the inflection behaviors are caused by the interaction between the first and secondary crack. Moreover, the quantity P_I is used to define the initiation pressure of the first crack, which can be obtained from the data curve plotting the crack width versus internal pressure (see Figure 22b). The quantity θ representing the angle between the first and secondary crack can also be obtained from numerical simulation results (see Fig 22c). Details of the impact of in-situ stresses and cohesive element strength on these four quantities are presented in Appendix B.

3.5 Algorithm Methodology

A simple approximate model for the predicted breakdown pressure for cracks at different orientations has been provided by Kirsch (1898), as adapted to the present problem by Huang et al. (2021a), via

$$p_b(\theta) = T_{max} + (\sigma_{Hmax} + \sigma_{hmin}) - 2(\sigma_{Hmax} - \sigma_{hmin})\cos 2\theta \quad (3-1)$$

Here T_{max} is the tensile strength of the rock (or, in the model, the cohesive element strength), σ_{Hmax} is the maximum in-situ stress, σ_{hmin} is the minimum in-situ stress, and θ is the angle between the crack and the maximum compressive stress direction.

Because the first crack always initiates at the $\theta=0^\circ$, that is, opposed by the least compressive stress, its initiation pressure is

$$P_1 = T_{max} - \sigma_{Hmax} + 3\sigma_{hmin} \quad (3-2)$$

Here P_1 and θ can be obtained from data (as described in the previous section), T_{max} is the rock tensile strength, and σ_{Hmax} and σ_{hmin} are two unknowns. This is the classical solution for crack initiation from a wellbore with a non-penetrating fluid (Hubbert and Willis 1957). Hence, the pressure P_1 corresponding to initiation of the first crack can be used to constrain this relationship. However, assuming tensile strength is known, there are two unknowns and therefore another equation is required to estimate the maximum and minimum horizontal stresses.

The three quantities P_2 , σ_{PP} and θ appear to be tied to the fracture interaction behavior since the inflection behaviors are apparently caused by the interaction between the first and secondary crack. Furthermore, by parametric study the quantities P_2 , σ_{PP} and θ are demonstrated to be systematically related to the combination of σ_{Hmax} and σ_{hmin} (Appendix B). Therefore, a hypothesis is proposed that these quantities can be related via an expression for the internal pressure of the borehole required to generate circumferential stress equal to σ_{PP} at the angle of the second crack, θ . If this pressure is proposed to correspond to the initiation pressure of the second crack P_2 , then the proposed relationship is

$$P_2 = \sigma_{PP} + (\sigma_{Hmax} + \sigma_{hmin}) - 2(\sigma_{Hmax} - \sigma_{hmin})\cos 2\theta \quad (3-3)$$

Here P_2 and σ_{PP} can be obtained from data (as described in the previous section). Initially this relationship is hypothesized by conjecture, building on observation and the form of the wellbore stress solution of the Kirsch (1898) solution. The hypothesis was extensively tested by numerical simulations with different stresses and rock properties, as detailed in Section 4. The results confirm this relationship and therefore it is adopted as a semi-empirical approximate model.

Now with two unknowns and two equations, both maximum and minimum in-situ stresses can be estimated from field test data (or synthetic data for validation). Graphical analysis of the

data (Figure 22) provides inputs P_1, P_2, σ_{pp} , the secondary fracture initiation angle θ (also from borehole strain data). Lab testing can constrain rock tensile strength T_{max} . The result is

$$\begin{Bmatrix} \sigma_{Hmax} \\ \sigma_{hmin} \end{Bmatrix} = \begin{bmatrix} 1 - \cos 2\theta & 1 + \cos 2\theta \\ -1 & 3 \end{bmatrix}^{-1} * \begin{Bmatrix} P_2 - \sigma_{pp} \\ P_1 - T_{max} \end{Bmatrix} \quad (3-4)$$

This approach essentially entails adopting the stress analysis of Eq. (3-2) as a simple approximate model for the fracture initiation and inflection points. The implementation involves providing inputs to the right-hand side of Eq. (3-4) based on data and inverting the 2x2 matrix.

Note that Eq. (3-4) is applicable, from a practical perspective, provided that the two horizontal stresses are sufficiently different from one another. Specifically, Huang et al. (2021a) demonstrates that the in-situ stresses appear, from the perspective of the data, to be identical when they are within the range $0.93 < \sigma_{hmin} / \sigma_{Hmax} \leq 1$. When this is the case, the data is predicted to indicate that there are several cracks initiating in multiple orientations and at the same internal pressure. Therefore, upon observation of multiple cracks initiating at the same pressure, it can be assumed that $\sigma_{Hmax} \sim \sigma_{hmin}$. For this condition, the Eq. (3-2) can be simplified to

$$P_1 = T_{max} + 2\sigma_{Hmax} = T_{max} + 2\sigma_{hmin} \quad (3-5)$$

It follows that, when similar in magnitude, the in-situ horizontal stresses can be estimated using only the first crack initiation pressure P_1 and the tensile strength of the rock T_{max} via

$$\sigma_{Hmax} = \sigma_{hmin} = \frac{P_1 - T_{max}}{2} \quad (3-6)$$

3.6 Validation of Algorithm

To validate the inversion algorithm embodied by Eq. (3-4) for dissimilar stress magnitude cases and Eq. (3-6) for similar stress magnitude cases, 100 cases are simulated to cover a practically-relevant range of in-situ stresses and rock mechanical properties. The ranges of parameters are (see Table 5 for definitions and Section 2.5 for details of numerical implementation):

$$\sigma_{Hmax} \in (10, 50)\text{MPa}$$

$$\frac{\sigma_{hmin}}{\sigma_{Hmax}} \in (0.5, 1)$$

$$E_{rock} \in (10, 70)\text{MPa}$$

$$\nu \in (0.15, 0.25)$$

$$K_{1C} \in (0.3, 2)\text{MPa m}^{1/2}$$

$$T_{max} \in (1, 10)\text{MPa}$$

$$\alpha \in (0, 1) \tag{3-7}$$

Simulations generate synthetic data of wellbore deformation versus internal pressure and the angle of secondary crack initiation for each case. The cases are firstly categorized by observing if there are multiple fractures initiating at the same wellbore pressure. If so, then the initiation pressure P_I is extracted graphically and Eq. (3-6) is used to estimate the magnitude of the similar magnitude horizontal stresses. If not, then the quantities P_1 , P_2 , and σ_{pp} are obtained graphically and the secondary fracture initiation data is obtained also, manually, from the data. In these cases of dissimilar magnitude stresses, Eq. (3-4) is applied to estimate the in-situ stresses based on the synthetic data.

Hence, for each of the 100 synthetic data cases we obtain an estimate of the stresses using the inversion algorithm. As a validation, the comparisons between estimated and actual maximum in-situ stresses are plotted in Figure 23.

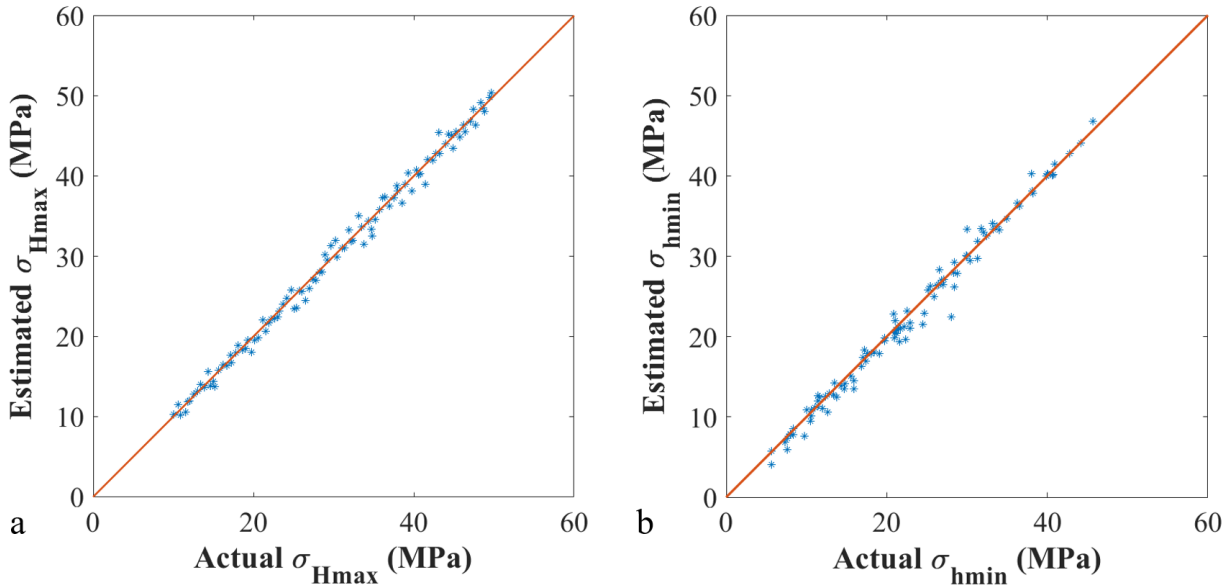


Figure 23 Comparison of estimated and actual in-situ stress for: a) maximum horizontal stress; b) minimum horizontal stress.

The comparison shows agreement at a level sufficient to validate the inversion algorithm over the ranges of parameters covered by this study and, of course, in the absence of either random noise or systematic errors in the data. Also, note that the algorithm works reasonably well even for cases that do not adhere as strictly to the pattern in Figure 22. Illustrative examples of data curves for several cases for which the inversion algorithm works well in spite of the data not giving ideal-looking results are provided in Appendix C. The conclusion is that the method is robust to various

borehole responses and that graphically identifying key quantities needed as inputs to the algorithm can provide sufficient accuracy in the inversion for a wide range of cases.

3.7 Error and Uncertainty

In previous work, Huang et al. (2021a) analyzed the crack initiation and propagation behavior for primary and secondary cracks under different combinations of in-situ stresses. In brief, the 2D plane-strain model is developed using ABAQUS while Cohesive Zone elements are implemented on pre-defined crack trajectories to simulate the possible crack initiation and propagation around the wellbore. Details of the model setup are provided in Section 2.5 with inputs described in Table 5. Based on simulations, the derivative of crack width with respect to internal pressure versus the internal pressure is plotted for an illustrative case, shown in Figure 22a. Four inflection points are labelled and are given by:

1. Inspection of a range of simulation data curves, both ideal and non-ideal in behavior (see Appendix C). For each of these, the uncertainty ascertained based on how sharply the curve changes at the relevant inflection points.
2. Inspection of a quarry test data curve (summarized in Ohanian et al. 2021).

Applying best-judgement estimates to these synthetic and field data curves, uncertainty of θ , P_1 , P_2 , σ_{PP} and T_{max} is set as 3%, 2%, 5%, 2% and 5%, respectively.

With these uncertainty levels set, 10,000 realizations of the inversion algorithm are carried out by randomly drawing the key quantities from the prescribed distributions. This gives an overall estimate of the uncertainty of the stress estimates. Additionally, the individual contribution of

uncertainty in each key quantity is estimated by fixing the others and allowing each quantity individually to be drawn 10,000 times, at random, from its prescribed distribution. Comparison of the histogram curves for estimated horizontal stresses by varying different key quantity are plotted in Figure 24 (also see Appendix Table 7 in Appendix D).

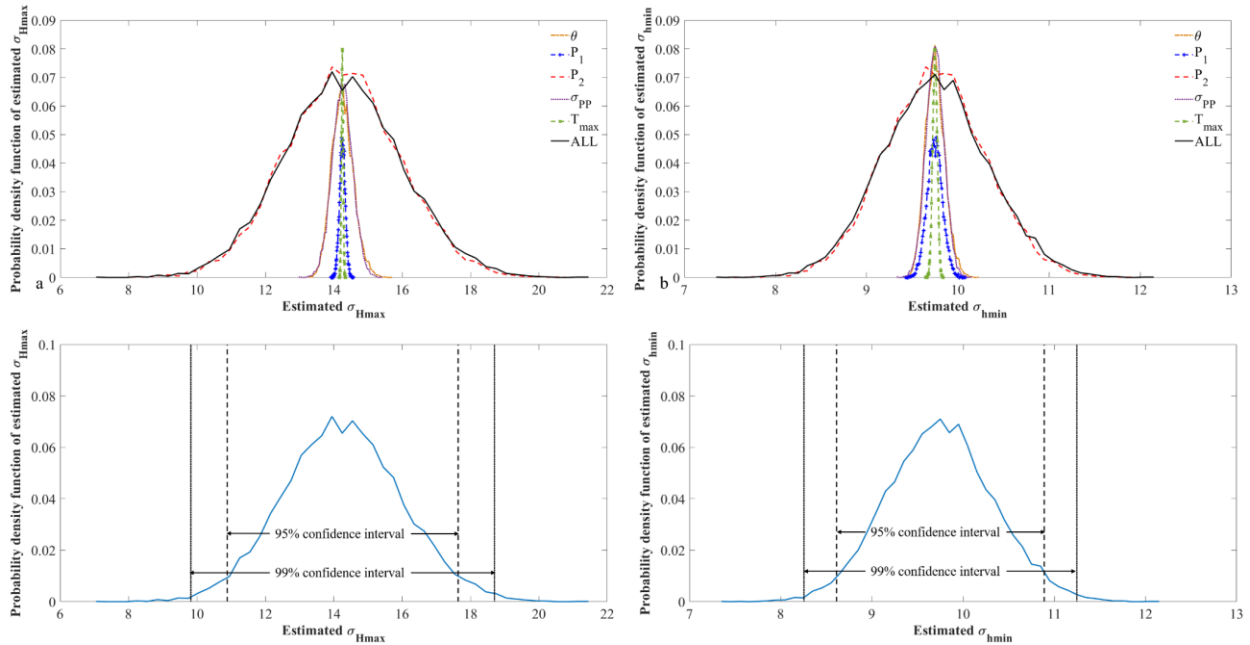


Figure 24 Comparison of histogram curves of the estimated horizontal stresses varying different key quantity for illustrative Case with actual $\sigma_{Hmax} = 15\text{MPa}$ and actual $\sigma_{hmin} = 10\text{MPa}$ for: a); Comparison of uncertainty level for estimated maximum horizontal stress; b); Comparison of uncertainty level for estimated minimum horizontal stress; c); Histogram curve for estimated maximum horizontal stress with confidence interval labelled; d) Histogram curve for estimated minimum horizontal stress with confidence interval labelled.

Figure 24a and 24b show that all the means are nearly the same while the standard deviations are different from each other. Indeed, the uncertainty degree of estimated σ_{Hmax} by varying only P_2 is the largest compared with the uncertainty by varying other key quantities (see

Figure 24a and 24b), indicating that the uncertainty of picking P_2 contributes most to the uncertainty for the estimation of both maximum and minimum horizontal stress. In addition, the coefficient of variation when accounting for simultaneous uncertainty in all the key quantities is 12% for estimated σ_{Hmax} and 6% for σ_{hmin} . The accuracy of the method is therefore reasonable even in light of inevitable uncertainty in picking key quantities comprising the algorithm inputs. Note a similar uncertainty level is reported for statistic simulation method used to estimate minimum and maximum stress (Feng et al. 2019). To examine this more closely, confidence intervals of 95% and 99% of the normal distribution curve fitting the estimated horizontal stresses are shown in Figure 24c and 24d. For this case, it can be concluded that the maximum horizontal stress is 14.3 ± 3.4 MPa while the minimum horizontal stress is 9.8 ± 1.1 MPa with 95% confidence.

Uncertainty estimation for all 100 cases firstly demonstrates dependence on the angle θ formed between the primary and secondary fractures. In the simulations, this quantity is found to be 22.5° , 45° , or 67.5° , with uncertainty for corresponding illustrative Cases 10, 15 and 30 shown in Figure 25 (see also Appendix D, Appendix Table 8). Less uncertainty occurs on the estimated value of the stresses for the cases where the combination of stresses and rock mechanical properties lead to a larger angle between the primary and secondary cracks. Additionally, Figure 25 shows that improving estimation of the quantity P_2 proportionally reduces the level of uncertainty.

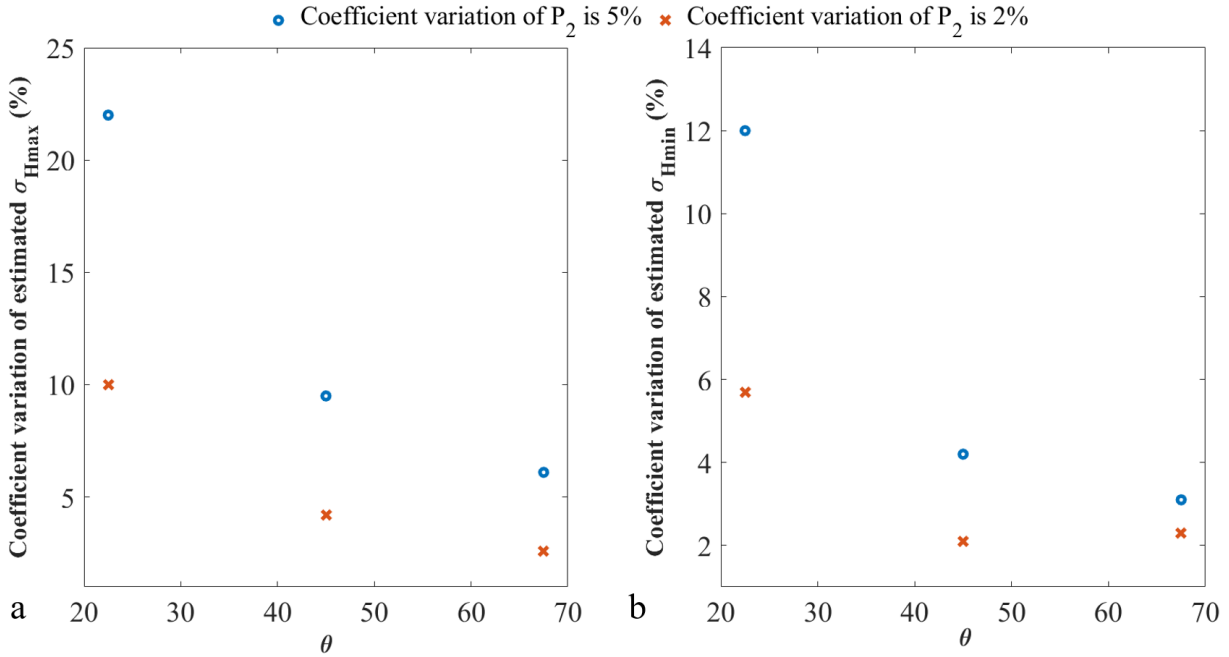


Figure 25 Comparison of uncertainty of estimated horizontal stresses with different θ generated from two different uncertainty of P_2 for: a) maximum horizontal stress; b) minimum horizontal stress.

3.8 Conclusion

A new inversion algorithm is developed and validated to estimate both maximum and minimum horizontal stress for sleeve fracturing field test. The algorithm is based on an approximate model of fracture initiation with its basis in stress analysis around a wellbore. Simulations using FEM with Cohesive Zone elements predict inflection points in the wellbore deformation that enable straightforward identification of 5 key quantities that comprise the inputs to the inversion algorithm. The algorithm is validated using 100 sets of synthetic data generated by the FEM-CZ model, with most cases showing agreement between the estimated and actual values of both minimum and maximum horizontal stress within a few percent.

Quantifying uncertainty in the stress estimations shows the greatest sensitivity to picking the quantity P_2 , an inflection point that is most directly tied to the ability to detect onset of growth of the secondary fracture(s) and the impact of secondary fracture growth on the deformation of the wellbore associated with the primary fracture. For reasonable ranges of uncertainties on the algorithm inputs, the 90% confidence intervals on the stress estimates tend to be less than 10 percent. However, when the secondary fracture initiates at a shallow angle relative to the primary fracture, the uncertainty is greater, with potential to exceed 20% especially if P_2 is poorly detected. Thus, as field experimental methods are developed, an emphasis should be placed on detailed detection of secondary fracture growth and its influence on deformation of the borehole caused by the first fracture, with a goal to limit the uncertainty for picking P_2 to around 2%, although for cases with larger angle between the first and second fractures the method is robust to larger levels of uncertainty in the data inputs.

4.0 Cohesive Elements Capture Size and Confining Stress Dependence of Rock Fracture Toughness Obtained from Burst Experiments

4.1 Preamble

This chapter comprises a preprint of Huang et al. (2022). In this chapter, a CZ-based numerical simulation is presented to investigate the impact of size/geometry and confinement on initiation and propagation behavior of primary and secondary fractures of at lab scale by analyzing the fracture emanation from a pre-notched borehole under confinement. The numerical model has been verified comparing predictions to results of laboratory tests known as “burst experiments”. The simulation results have demonstrated that application of LEFM to rock fracture, especially under conditions where the near-tip inelastic zone size is similar to the crack size, will result in a need to introduce a fracture toughness that is both size and stress dependent. Then, the CZ-based approach overcomes this limitation of LEFM-based simulations by capturing the crack initiation behavior with three parameter traction-separation law that is the same for all tests.

4.2 Chapter Summary

Numerical analysis of growth of cracks from a notched borehole under confinement demonstrates the impact of size and confining stress on initiation and propagation behavior of rock fracture at lab scale. A Finite Element framework employing plane strain cohesive elements is applied to simulate crack initiation and propagation behavior. The model is validated by comparing

predictions to results of laboratory tests known as “burst experiments”, which have been used for several decades to characterize rock fracture toughness under confined conditions. The simulations capture the crack initiation behavior with three parameter traction-separation law that is the same for all tests. This contrasts with approaches that apply linear elastic fracture mechanics wherein ad hoc stress and size dependence must be introduced to the fracture toughness. Furthermore, the simulations also confirm the limitation of the typical burst experiment configuration owing to ambiguity in identifying the moment of crack initiation, thereby pointing to a straightforward modification of the experiment that will remove this ambiguity, while also indicating that pairing Acoustic Emission monitoring with the typical setup in order to independently detect crack initiation can enable complete characterization of the traction-separation law.

4.3 Introduction

The burst experiment (Abou-Sayed 1978) is a long-used technique applied mainly in the oil and gas industry to estimate the fracture toughness of rocks under confinement in the laboratory. While other approaches are convenient for testing unconfined specimens, determining rock fracture behavior in the deep subsurface, where confining stresses are large, requires specialized tests, with the burst experiment being among the most popular. In this test, radial confinement is applied to the boundary of a cylindrical specimen with simultaneous pressurization of an internal and axially-notched borehole. As the test proceeds (Abou-Sayed 1978), the external and internal pressure are proportionally increased, with the internal pressure typically ramping up with a slope that is six times greater than the external pressure, until a crack catastrophically grows, and a burst event occurs in the specimen that is detected in the pressure and flow rate records of the pump(s)

that are controlling the internal and external applied pressures. Recently, Yoshioka et al. (submitted) proposed that, in some commonly-used geometries and loading combinations, there will be an undetected stable crack growth period before the crack grows unstably to the boundary. This will lead to large uncertainty on the actual notch (i.e. crack) length that is associated with the stresses reaching the condition for rupture. The inaccurate notch length will, in turn, lead to inaccurate estimation of the fracture toughness. To investigate this source of uncertainty in experimental interpretation, Zhang (2019) carried out a series of both classical and modified burst experiments with acoustic emission (AE) detection to experimentally evaluate how the experimental configuration impacts the validity of the estimates of the fracture toughness. These experiments, combined with Finite Element Analysis of the associated stress intensity factor, (Yoshioka et al. submitted), have clarified that the uncertainty in notch length for some geometries and have provided guidelines for modifying the geometry of the burst experiment to overcome this issue. However, the analysis is based on Linear Elastic Fracture Mechanics (LEFM), which assumes that the equations of elasticity are valid arbitrarily close to the crack tip. In contrast, for most rocks the process zone near the crack tip is expected to be at least on the order of 10 mm (Labuz et al. 1987; Lin and Labuz 2013), which is similar to the size of both the borehole and the specimen itself for typical burst experiment setups. As a result, LEFM-based analyses will miss size effects (and, more generally, impacts of geometric details of the specimen) that could be important to experimental interpretation.

Motivated by these prior works and the knowledge gaps remaining due to reliance upon LEFM for analysis, a cohesive zone (CZ) finite element model is used here to interpret burst experiment results in order to characterize dependence of rock fracture on confining stress and specimen size. Papanastasiou and Thiercelin (2011) presented a model that introduces a

combination of fracture mechanics parameters with length dimension that scales the size of the holes, thus allowing for size effect predictions. Therefore, the approach leverages recent burst experiments (Zhang 2019) carried out in Kosota Valley Limestone with various loading geometries including varying the confining stress as well as the size of the borehole. Matching LEFM-predictions to the results of these experiments requires introducing *ad hoc* dependence of the fracture toughness on both confining stress and hole size. While this approach has pragmatic use, it is challenging to translate such results for the purpose of predicting crack propagation in rock at scales and confining levels that are not covered by the experiments. The present study therefore aims to capture the crack initiation and propagation behavior for laboratory experiments using a traction-separation law that is the same for all experiments, regardless of hole size and confinement level.

With that said, it is important to recognize that there are a variety of potential sources of high rock fracture toughness observed under field conditions. The causes are thought to include confining stress acting on the region where the rock is breaking and plasticity, including ductile rock deformation, at scales that cannot be neglected relative to the size of the main crack (Papanastasiou, 1997, 1999). The burst experiment and the CZ modeling thereof considers the role of stress and plasticity in part. Namely, it considers a particular stress state of isotropic radial confining stress and the limited case of inelastic deformation ahead of the crack tip along the line of crack growth. While this limited consideration surely does not capture the entirety of high apparent rock fracture toughness under field conditions, it does provide a step forward in the overall goal of developing laboratory-scale tests that can characterize rocks in a manner such that the associated models can be deployed for field-scale predictions. Furthermore, the calibrated

cohesive model can be used as propagation criterion in elastoplastic computations for field conditions to account for the high effective fracture toughness.

The paper is organized as follows. The burst experiment in the literature and the typical results provided from Zhang (2019) will be reviewed as a background. Then, the methodology of modeling and model setup for numerical simulation are provided. Next, the simulation results are carried out to show the size and confining stress dependency of crack initiation and propagation behavior. Finally, a comparison will be shown among various approaches to capturing experimental behavior, including LEFM with a single value of the fracture toughness, LEFM with ad hoc dependence of toughness on confinement and hole size, and the new model using a 3 parameter CZ model for all cases.

4.4 Background

Numerous studies investigate the effect of confining stress on the fracture toughness, with perhaps the most in depth being carried out with Indiana limestone (Roegiers, 1991; Thallak, 1993; Abou-sayed 1978; Schmidt and Huddle, 1977). Schmidt and Huddle (1977) designed two types of experiments to study the effect of confining stress on fracture toughness of Indiana Limestone. One is a single-edge-notch test and the other is a three-point-bend test notch modified to enable application of confinement. Roegiers and Zhao (1991) have conducted laboratory experiments with Chevron-notched disk specimen (CDISK) to measure K_{IC} of rocks again under simulated subsurface stress conditions. Primary loading is applied on the specimen and confining stress is generated by hydraulic oil. Thallak et al. (1993) designed and carried out a series of experiments to measure fracture toughness in a hydraulic fracturing-like environment. The specimen is set into

a cylindrical cell and then the fracture fluid is injected until evidence for crack growth or fracture break-through is observed. The confining stress is generated by fluid in the chamber while the surrounding membrane prevents the fluid from flowing into the specimen. The burst experiment (Abou-Sayed 1978; Abou-Sayed and Jones 1979) applies radial confinement to the boundary of a cylindrical specimen with concurrent pressurization of an interior, axially-notched borehole. The outer and inner pressure is increased proportionally until the specimen bursts. A compilation of these published results is shown in Figure 26, indicating an increasing relationship between the fracture toughness and confining stress. More recently, Funatsu et al. (2004) carried out experiments using single edge notched round bar in bending and semi-circular bend specimens of Kimachi sandstone and Tage tuff to investigate the effect of confining pressure on the fracture toughness of clay bearing rock. The fracture toughness of sandstone and tuff was found to be significantly affected by increasing confining pressure.

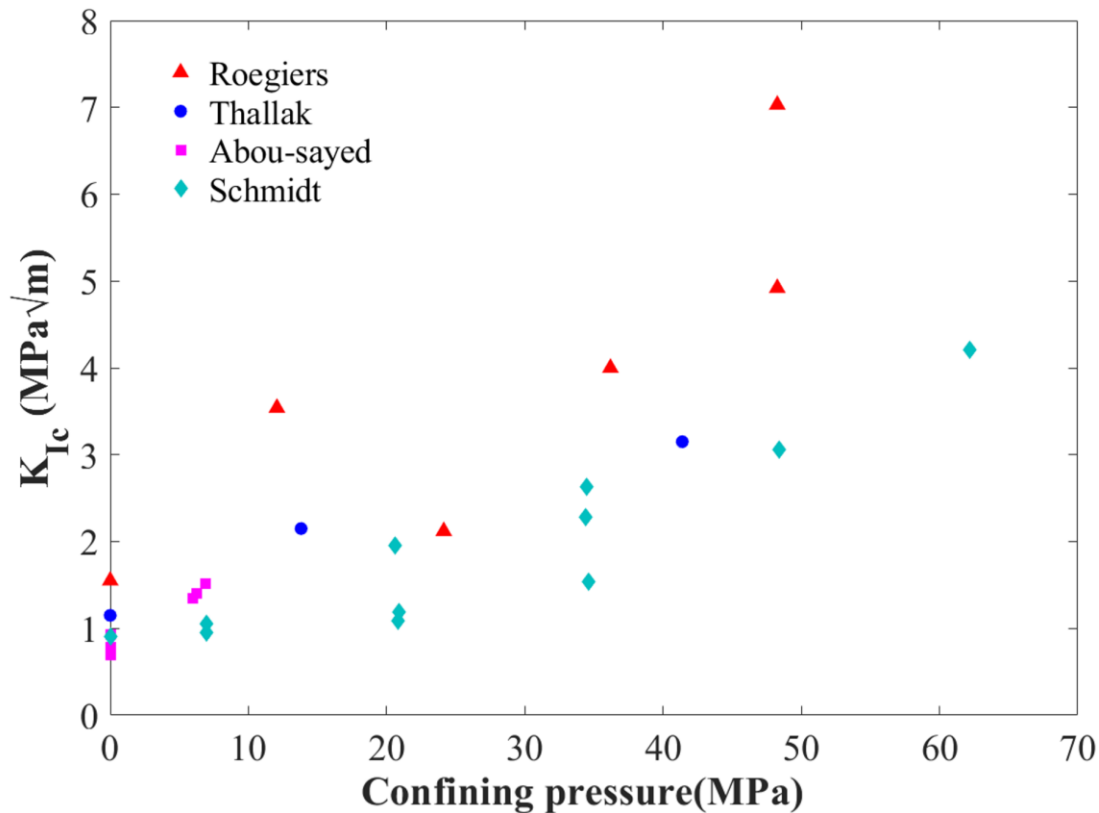


Figure 26 Published results of fracture toughness versus confining stress on Indiana Limestone (after Roegiers, 1991; Thallak, 1993; Abou-sayed 1978; Schmidt and Huddle, 1977).

As a result of these and similar studies, the stress dependence of fracture toughness for rock has become widely accepted. However, characterizing this phenomenon remains a challenge with the burst experiment continuing to be perhaps the most widely used approach (Abou-Sayed 1978). More recently, Zhang (2019) carried out a series of both classical and modified burst experiments to experimentally evaluate how the experimental configuration impacts the validity of the estimates of the fracture toughness. The setup of the burst experiments carried out by Zhang (2019) is shown in Figure 27. Here the specimen diameter is 6 inches (152.4 mm) and in the case where the inner hole diameter is 0.5 inches (12.7 mm), the ratio of these two diameters (1/12)

recovers a classical burst experiment as described by Abou Sayed (Abou-Sayed 1978). A modified configuration changes only the hole diameter, increasing it to 2 inches (50.8 mm).

To begin a burst experiment, the cylindrical rock specimen is placed in the center of a triaxial cell (see Figure 27), with confining stress provided by the oil filled chamber. The specimen is held at the vertical center of the cell by two aluminum spacers, while a Tygon jacket is inserted into the central hole of specimen and sealed by two rubber plugs. A steel rod holds the two rubber plugs in place inside the Tygon tube, expanding them via compression to provide better sealing. The injection tube is drilled inside the steel rod and thus induced the internal pressure, P_i , by pumping hydraulic oil through the tube while the Tygon jacket prevents the fluid from infiltrating the specimen. Moreover, two ISCO syringe pumps are used simultaneously to ramp up both the internal pressure and the confining pressure, P_o , in a fixed proportion to one another, until a pressure drop is observed. Note that the ratio of the external to internal pressure is typically taken as 1/6 or 1/8, and little justification is given in the literature. However, for consistency with past work, we adopt also this proportional pressure ramping procedure. Once the pressure drop is observed, it is interpreted as the moment of specimen rupture which is in turn assumed to coincide with crack initiation and growth, hence the name “burst experiment”. The validity of this final assumption is critical to the interpretation and will be discussed in detail throughout this paper.

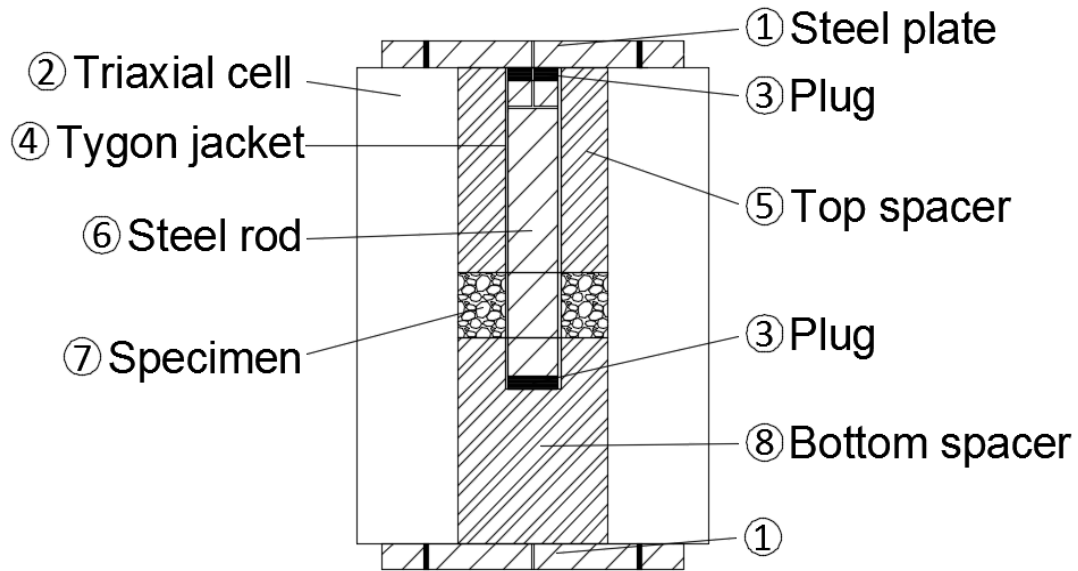


Figure 27 Lab setup for burst experiment (after Abou-Sayed 1978).

Because of the possible ambiguity involved with the assumption that the burst pressure corresponds to the moment of crack extension, acoustic emission (AE) detection method has also been applied in Zhang (2019) by placing four sensors on the top surface of the specimen (see Figure 28). The AE data is collected during the increase of the internal pressure, providing the numbers of events changing with time. The results from AE detection are analyzed along with the pressure records to infer if rock breakage occurred prior to the peak pressure.

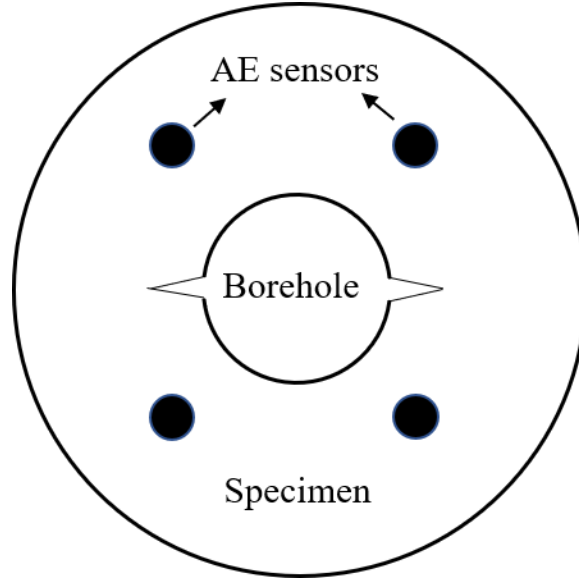


Figure 28 AE sensor layout on the specimen, viewed from the top looking down (Zhang 2019).

The rock material is assumed to be linear elastic with homogeneous properties and, as with all linear elastic fracture mechanics calculations, an assumption that the plastic zone is negligibly small compared to the size of the crack. It is also assumed that the fracture toughness does not change with fracture length with elastic deformation. But if plasticity develops around tip, it was shown that the effective fracture toughness increases with fracture length (Papanastasiou, 1997, 1999). Once the pressure associated with crack growth is ascertained from the experiment, the fracture toughness K_{Ic} for each test can be estimated using the equation proposed by Abou-Sayed (1978), that is

$$K_{Ic}(l) = P_{ic} K_I^{B*}(1, l, w, p^*) \sqrt{a\pi} \quad (4-1)$$

Here the quantity K_I^{B*} is the normalized stress intensity factor for a unit internal pressure, which can be computed numerically as a function of l , w and p^* . Also, P_{ic} is the internal pressure at the time of the burst, a is the borehole radius, p^* is the ratio of confining pressure over internal

pressure, w is the ratio of specimen radius over borehole radius, l is the normalized crack length computed via $l = \frac{L}{b-a}$, where L is the crack (notch) length and b is the specimen radius.

The challenge in the interpretation arises because it might not always be correct to assume that the burst pressure, P_{ic} , gives the loading required for first extension of a crack of length L . Indeed, if there is stable crack growth prior to the sudden change in pressure corresponding to an eventual unstable “burst”, then the crack length L will be longer at the time of the burst event than is assumed by the analysis. This will lead to overestimating the fracture toughness and hence overstating the dependence of fracture toughness on confinement. To this point, there are three possible evolutions of K_I^{B*} and the corresponding P_{ic} , which can be applied to define the stability of the crack growth in the burst experiment (Yoshioka et al. submitted).

1. The K_I^{B*} is decreasing monotonically with l increasing while the P_{ic} is increasing with l increasing monotonically (see Figure 29a). This case leads to a “stable” crack growth in the burst experiment.
2. The K_I^{B*} is decreasing with l increasing at beginning and then increasing with l increasing while the P_{ic} is increasing with l increasing and then decreasing with l increasing (see Figure 29b). The crack will grow either stably or unstably depending on normalized crack length l .
3. The K_I^{B*} is increasing monotonically with l increasing while the P_{ic} is decreasing with l increasing monotonically (see Figure 29c). In this case, the crack will grow unstably, and the specimen will burst.

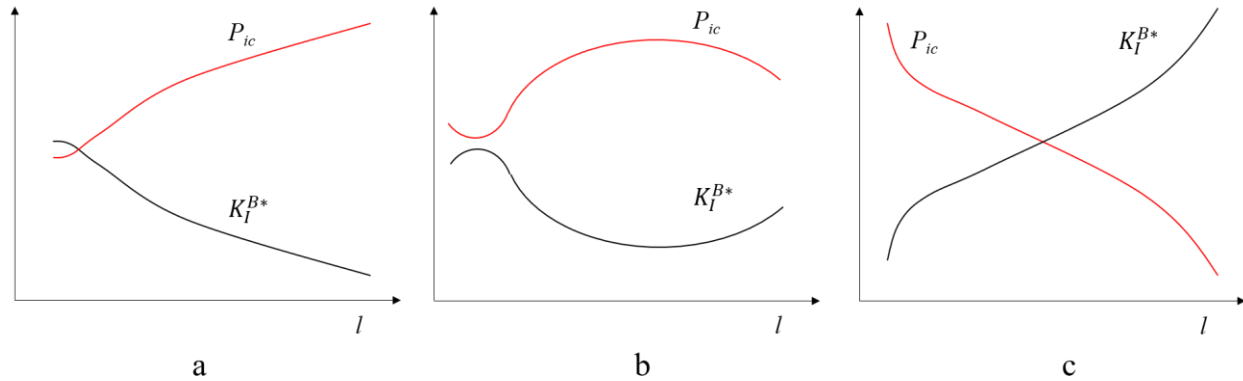


Figure 29 Possible evolution of normalized stress intensity factor K_I^{B*} versus normalized crack length l (after Yoshioka et al. submitted).

The burst pressure P_{ic} , obtained from the laboratory experiment, is the key value to calculate the fracture toughness (see Eq. (4-1)). Indeed, there are two possible ways to pick this P_{ic} from experiments (Zhang 2019). One way is to pick the peak pressure from pressure data recorded in experiments as shown in Figure 30 since the sudden pressure drop shown in the pressure data curve is considered to reflect the specimen rupture event. Another way, available only when AE data has been collected (which is not usually the case), is to obtain the P_{ic} at the time of the first inflection point from the AE data recorded in experiments (see Figure 30). It is clear from this example, which is for a stable case (0.5 inch hole in a 6 inch specimen), that the burst pressure one would pick from the pressure record significantly exceeds the crack initiation inferred from AE data. Zhang (2019) shows that such ambiguity does not exist for unstable cases (2 inch hole in a 6 inch specimen). And, to be clear, the CZ modeling presented in this paper does not resolve ambiguity in the moment of crack extension, The moment of crack extension is clear in the simulations, but if it is not observable in the experiments, the ambiguity remains. So, rather than resolving an experimental ambiguity, the CZ modeling provides a framework for capturing size/geometry and confining stress impacts on crack initiation and growth in cases where detection

of said growth is unambiguous. Henceforth, our analysis and comparisons will therefore be limited to all unstable cases and only the stable cases with AE data reported by Zhang (2019).

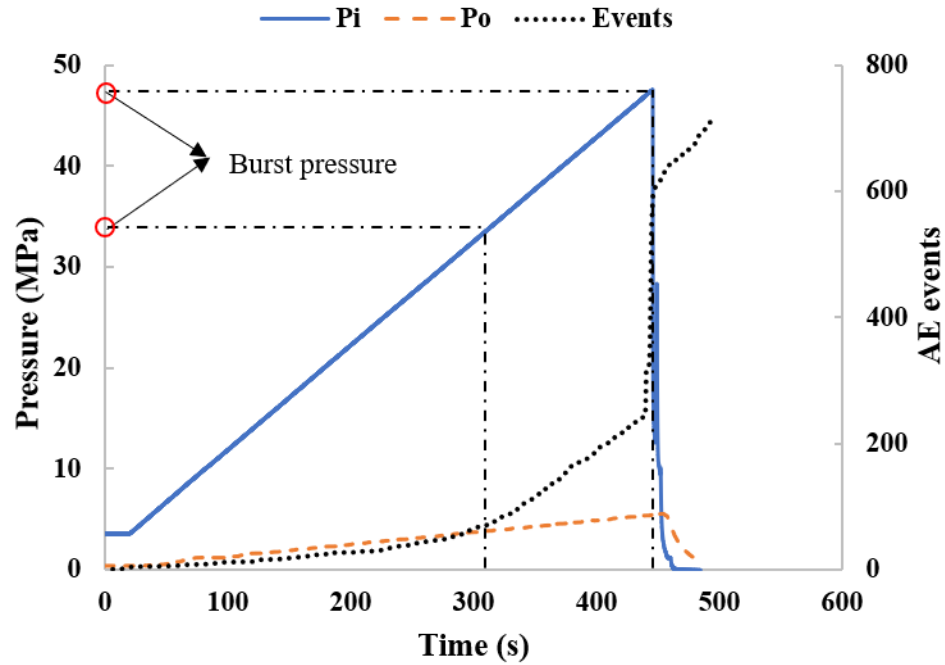


Figure 30 . Data curves with two possible P_{ic} labelled for lab experiment results of test 3 ($\frac{1}{2}$ inch borehole in a 6 inch specimen, the ratio of confining stress over internal stress is $\frac{1}{8}$) (after Zhang 2019).

4.5 Modelling Methodology

4.5.1 Cohesive Zone Elements

The numerical simulation model is developed using the commercial Finite Element method (FEM) software ABAQUS. The rock matrix is represented by plane strain elements governed by linear elasticity for an isotropic rock, and the cohesive elements are implemented on pre-defined

crack trajectories. The correspondence of solid and cohesive elements is illustrated in Figure 1 in a generic case of a pre-defined crack path, noting that details of the burst experiment geometry will be described later. Crack initiation and growth is accounted using built-in Cohesive Zone elements, which applies a Dugdale-Barenblatt type cohesive crack propagation model (Barrenblatt 1962 and Dugdale 1960). This cohesive crack model has been widely applied to quasi-brittle materials such as rock and concrete (Papanastasiou 1997; Papanastasiou 1999; Sarris and Papanastasiou 2011; Saouma et al. 2003; Segura and Carol 2010; Yao 2012), including for simulating size effect on hydraulic fracture initiation for a wellbore (Lecampion 2012).

The behavior of the cohesive elements follows a prescribed linear traction-separation law. The traction-separation law defines the relationship between the traction (T) and the displacement (δ) between a pair of cohesively-bonded surfaces (i.e. the two opposing surfaces connected by the CZ elements in the generic case of Figure 1). A bilinear damage evolution model (after Barrenblatt 1962 and Dugdale 1960, see Figure 31) is adopted in this study. This three-parameter model assumes that the cohesive surfaces follow linear elastic behavior (i.e. with a constant slope) before the traction reaches the cohesive element strength, T_{max} . This is equivalent to saying that the material begins to incur damage after the separation displacement exceeds the critical value of δ_0 . Then, the material softens, in this model assumed to be linearly, until completion of the material failure at the separation value of δ_f . The area under this curve gives the critical energy release rate, G_c , which can be related to the fracture toughness of the rock, K_{Ic} , via (Irwin 1957)

$$G_c = \frac{K_{Ic}^2(1-\nu^2)}{E} \quad (4-2)$$

where the E is the Young's modulus and ν is the Poisson's ratio. Also note that no shear or slippage are involved in this energy release rate. Additionally, the ratio ($\alpha = \delta_0 / \delta_f$) embodies the

relative portion of the region wherein the cohesive element is in elastic deformation compared to the portion in which it is undergoing plastic softening. Finally, note that in ABAQUS there is an ability to account for shearing failure and shearing deformation of cohesive elements, which is taken as negligible because crack opening is assumed to be caused by normal traction by setting shearing strength T_s and shearing stiffness K_s to values that exceed their tensile counterparts by several orders of magnitude. Moreover, the T_{max} has the similar order with the normal tensile strength magnitude of material, although its specific value is chosen in this study to match burst experiment results. Note that using an adjusted value of T_{max} relative to a nominal tensile strength obtained from, say, indirect tension tests is experimentally justified, for example by Haimson and Fairhurst(1969) who observed a different value of tensile strength governing hydraulic fracture initiation than would be obtained from testing in other configurations (see page 814). In this case where shear stiffness and tensile strength are large enough to be irrelevant to material failure, the breakage is uniquely described by any 3 independent parameters describing the traction separation law. In the following, we will use T_{max} , G_c , and the ratio α , as indicated by Figure 31, with other quantities (such as hardening and softening slopes) implicit in, and readily obtained from, these three parameters.

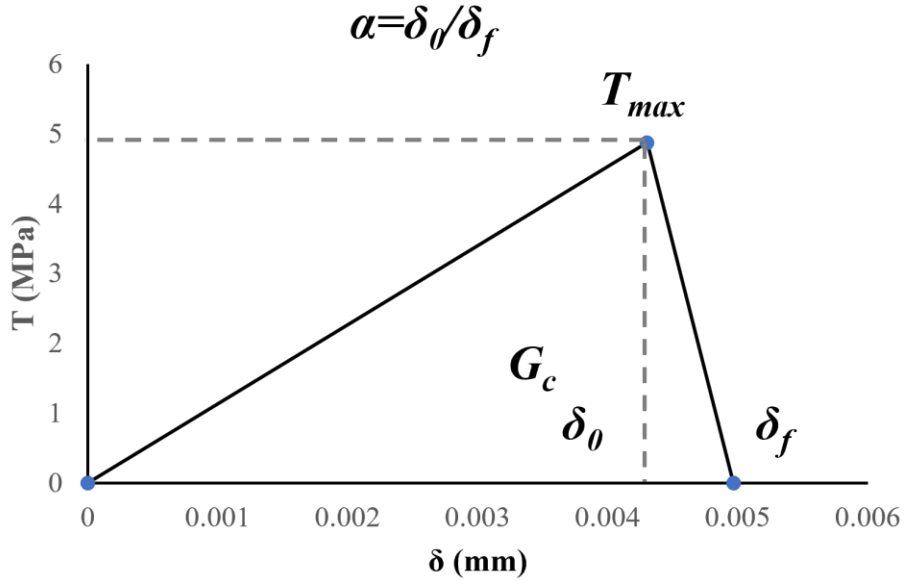


Figure 31 Bi-linear traction-separation law of cohesive elements (after Barrenblatt 1962 and Dugdale 1960).

4.5.2 Model Setup

The burst experiment is modeled in plane strain with a central borehole having diametrically-opposed notches in an isotropic rock with confining stress (Figure 32a). The plane strain approximation is strictly valid provided that the length of wellbore pressurized by the injection fluid is long compared to the wellbore diameter. In the present case, the length of the specimen is 2 inches (50.8 mm), and so it is not strictly satisfied for all cases and hence three-dimensional effects are possible and can be a topic of future investigation. The diametric notches are a part of the burst experiment setup, and are placed using saw cuts (Zhang 2019). The crack is assumed to initiate and grow in the notch orientation. Therefore, beginning at the tips of the notches with initial length L , cohesive elements are distributed along 2 pre-defined planes for potential crack growth, as shown in Figure 32. More specifically, cohesive elements are firstly place on the

bi-wing path. Then, a certain length of cohesive elements started from the wellbore will be removed (strength taken to zero) to define an initial notch with length L . To match the experiments, the radius of the specimen, b is 3 inches (76.2 mm) while the borehole radius a is either 0.25 inches (6.35 mm) or 1 inch (25.4 mm), as shown in Figs. 8b and 8c, respectively. Note that in both cases a particular mesh is discussed and presented, and these are chosen after a mesh sensitivity study with various mesh densities confirms that the solution is not mesh dependent.

The pressure loading is applied on both external and internal boundaries of the cylindrical specimen as P_o and P_i , respectively. Both P_o and P_i are set as a pressure loading increasing proportionally with time. The ratios of P_o over P_i for each test are shown in Table 2. The internal pressure P_i is increased at a constant rate, 6.2 MPa/min, starting from 2.5 MPa. Simultaneously, the outer (confining) pressure P_o is increased either at 1.03 MPa/min from 0.42 MPa, or at 0.78 MPa/min from 0.31 MPa, with these corresponding to the $p^*=1/6$ and $p^*=1/8$ cases, respectively. Roller-type boundary conditions are applied to 4 elements on the outer surface of the specimen to avoid rigid translations and rotations (see Figure 32a).

As previously mentioned, the simulation results in this paper are compared with the lab experiments carried out by Zhang (2019). These experiments used Kasota Valley Limestone, a dolomitic limestone quarried in southern Minnesota, especially near the Minnesota River and its tributaries. The rock properties of this limestone have been measured in the lab (Lu et al. 2020; Lu et al. 2017; Lu 2016) and are shown in Table 1. Additionally, the geometry, loading, stability, and burst pressure for the 6 configurations tested by Zhang (2019) are listed in Table 2. The burst pressure P_{ic} obtained from the laboratory experiments and the computed K_{Ic} using Eq. (4-1) based on LEFM method are also included in Table 2 (see Zhang 2019 and Yoshioka et al. submitted). Because some configurations had repeated experiments, a total of 12 experiments were performed.

These are listed in Table 2, noting that acoustic emission (AE) data is available for stable test 3. Also note that the meaning of the “partially stable” designation for some experiments will be discussed later in this article.

Table 6 Material properties of Kasota Valley Limestone (Lu et al. 2020; Lu et al. 2017; Lu 2016)

Material property		Test method
Young’s modulus	45GPa	Uniaxial compression on cylindrical specimens (ASTME111-04, 2010a)
Poisson’s ratio	0.3	Uniaxial compression on cylindrical specimens (ASTME132-04, 2010b)
Fracture toughness	0.77MPa.m ^{1/2}	Three-point loading on semicircular bend specimens (Kuruppu et al., 2014)

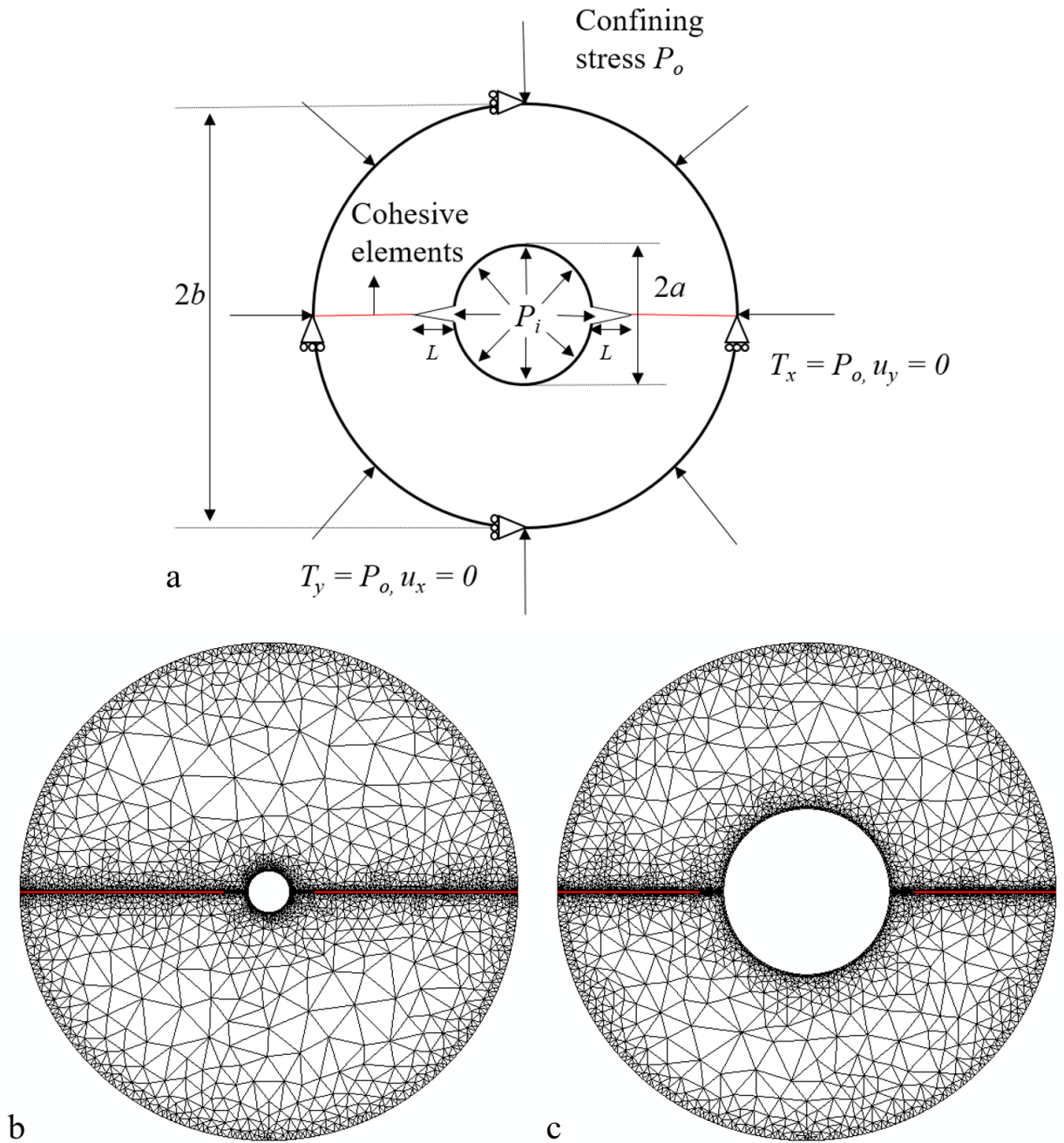


Figure 32 Sketch of model setup for burst experiment: a) Boundary conditions and loading setup; b) Mesh setup for 1/2-inch borehole; c) Mesh setup for 2-inch borehole.

Table 7 Configuration properties and stability for lab tests (after Zhang 2019 and Yoshioka et al. submitted).

Test ID	Stability	a (mm)	b (mm)	L (mm)	$p^*=P_o/P_i$	P_{ic} (Zhang (2019))	Computed K_{Ic} (MPa.m ^{1/2})
1	partially stable	6.35	76.20	7.68	0	14.10	0.84
2						17.60	1.05
3 (AE)	stable	6.35	76.20	7.68	1/8	47.60	1.56
4	stable	6.35	76.20	7.68	1/6	49.70	1.20
5						52.20	1.28
6	unstable	25.40	76.20	7.62	0	2.60	0.43
7						2.20	0.36
8	unstable	25.40	76.20	7.62	1/8	5.00	0.6
9	unstable	25.40	76.20	7.62	1/6	7.50	0.79
10						7.40	0.78
11						6.50	0.68
12						6.90	0.73

4.6 Results

4.6.1 Unstable Cases

All 12 lab tests shown in Table 2 are representing 6 different configurations varying by size and confining stress. The simulation results for lab tests 6-12, with 2-inch diameter borehole and different confining stress, show consistent crack growth behavior. Here, simulation cases for these lab tests are defined as unstable cases according to the categorization provided by Yoshioka et al. (submitted). While all cases are simulated and results are presented later in terms of comparing predicted and actual burst pressure, the simulation result for lab test 8 is selected as a

representative case for presenting details showing the crack initiation and propagation behavior that is qualitatively similar (although quantitatively distinct) all the unstable cases. For this case, Figure 33 shows the evolution of crack geometry and stress concentration, which corresponds in each time to a certain internal borehole pressure. The right column of subfigures shows contours of the maximum tensile principal stress (with tension positive). The left column of subfigures shows a zoomed-in view of the change of deformed CZ elements during the crack propagating progress colored by the overall scalar stiffness degradation (*SDEG*) value, which is calculated via,

$$SDEG = \frac{u^{pl}}{\delta_f} \quad (4-3)$$

Here u^{pl} is the effective displacement of the CZ element, which is also taken as the crack width in the following discussion. And also note the δ_f is computed by

$$\delta_f = \frac{2G_c}{T_{max}} \quad (4-4)$$

Hence, the CZ elements are fully broken when $SDEG=1$. Otherwise, the CZ elements are active (i.e. in plastic softening) if $0 < SDEG < 1$. It can be seen from Figure 33a and 33b that there are no CZ elements fully broken until the time increases to 24.21s. Then, the crack is fully broken to the specimen edge at $T=24.22s$ (see Figure 32c). The evolution of active CZ, labelled from Figure 33a to 33c, proves that the active CZ length is increasing from 0.28mm to 9.50mm as internal pressure increases from 4.85MPa to 4.98MPa before the crack grows to the edge. Moreover, the crack propagates to the specimen edge in only 0.01s (see Figure 33b to 33c), pointing to an unstable crack growth behavior. Indeed, this unstable crack growth can be interpreted by the location of stress concentration shown in the maximum principal stress contour changing along with fracture propagation (see the right column of Figure 33). Hence, in contrast to subsequent cases that will be presented, for these unstable cases there is only one distinguishable stage in the stress evolution (unstable growth) before the crack is fully developed to the specimen

edge (see Figure 33). During this stage, the maximum principal stress concentration is always expanding along with the crack tip as the crack grows until the crack is fully broken to the edge (see Figure 33a-33c). Also note, there is a tensile stress concentration at the borehole. However, the magnitude of stress concentration at the borehole is approximately half of the stress concentration at the crack tip. So that crack propagation from the notch is expected rather than fracture initiation and propagation from the borehole away from the notch.

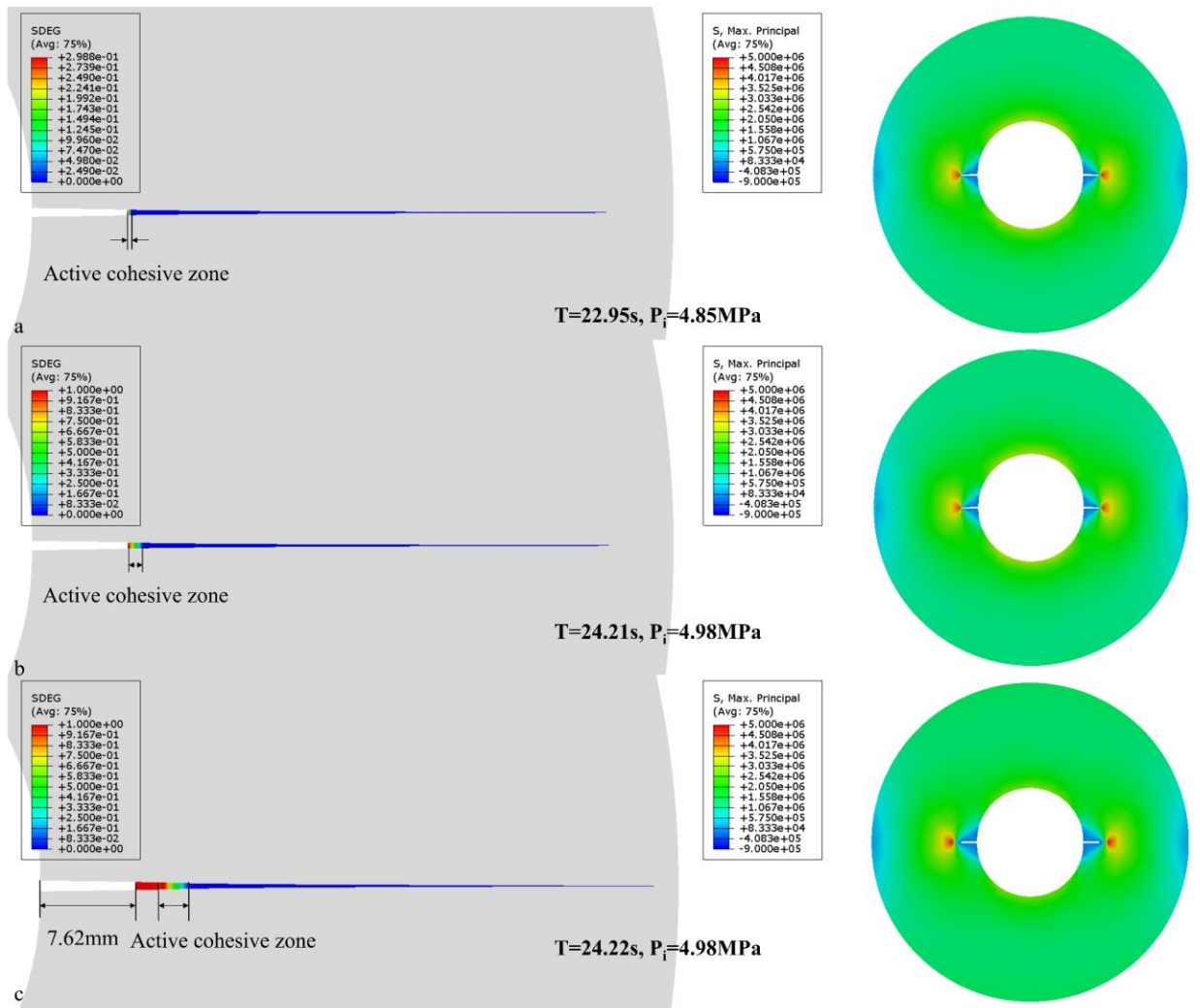


Figure 33 Simulation results showing the open cohesive elements colored by SDEG value and maximum principal stress contour for lab test 8 (2-inch borehole, showing the ratio of confining stress over internal stress is 1/8) at: a) 22.95s; b) 24.21s; c) 24.22s.

To view in greater detail, the fracture width and fracture length versus internal pressure loading for test 8 conditions are shown in Figure 34. Note that two different definitions of crack width as well as two definitions of crack length are included. For crack width, one definition counts the crack opening at the borehole while the other counts the crack opening at the notch tip. For crack length, one definition uses the distance to the first damaged element ($SDEG > 0$) and another

uses the distance to the first fully broken element ($SDEG=1$). The comparison of crack length from these two definitions demonstrates that the active CZ length is increasing as the internal pressure increases before any CZ element is fully broken. All the four data curves presented in Figure 34 show a sudden jump at the same corresponding pressure, reflecting the unstable crack growth behavior. Moreover, the unstable crack growth occurs once the crack width at the notch tip reaches the complete failure δ_f (see Figure 34). Hence, the internal pressure corresponding to this sudden jump is unambiguously defined as the predicted burst pressure for unstable cases, and it is this prediction that is compared with the burst pressure obtained from lab experiments in later discussions. Note that for purposes of comparison, the burst pressures for the laboratory experiments for unstable lab tests 6-12 (Table 2) are obtained by picking the peak pressure from the pressure data recorded (Zhang 2019) because the first sudden drop shown in pressure data (see Figure 30) reflects the specimen rupture event.

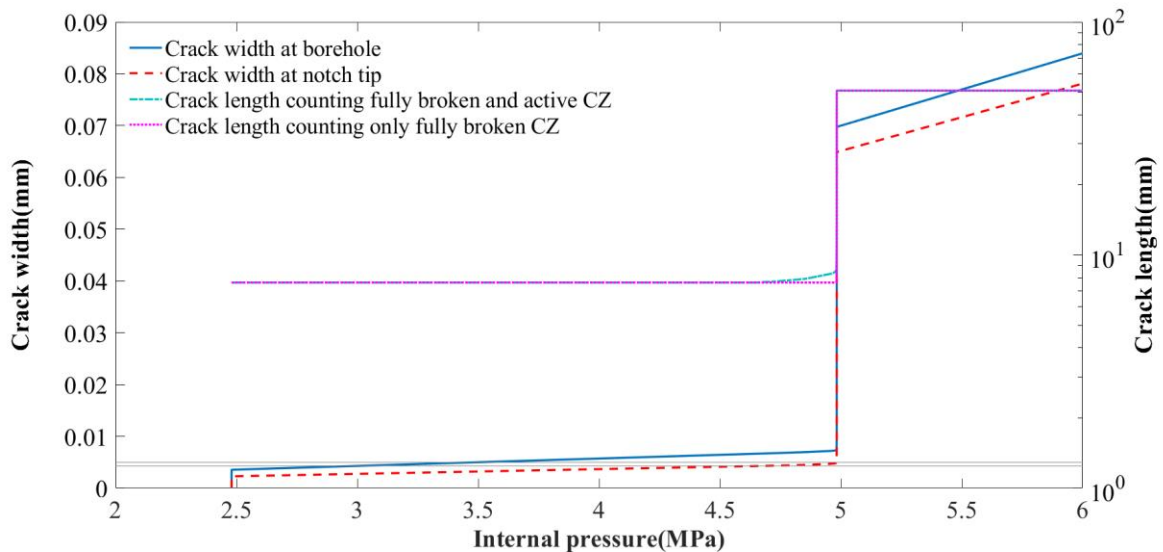


Figure 34 Crack width and length versus internal pressure with Pic labelled for CZ-based simulation of test 8 (2-inch borehole, showing the ratio of confining stress over internal stress is 1/8).

4.6.2 Confined Stable Cases

Laboratory tests 3-5, with 0.5 inch diameter borehole and non-zero confining stress are categorized as stable cases by Yoshioka et al. (submitted) because LEFM simulations predict stable growth of the crack prior to the final burst event. The CZ predictions for these tests are qualitatively similar to one another but strikingly different to the nominally unstable cases. The simulation result for laboratory test 3 is selected as a representative case with Figure 35 showing the open cohesive elements and the maximum principal stress contours, thus illustrating the evolution of crack geometry and stress concentration after the initiation of the primary fracture, corresponding in each time to a certain internal borehole pressure. The left column of Figure 35 shows the change of deformed CZ elements during the crack propagating progress colored by SDEG value. Fig 11a to 11b show that none of the CZ elements are fully broken before $T=307.96s$. Then, the crack propagates, but much more slowly than it did in the unstable cases since it takes only 24.22s for the crack to propagate to the boundary for unstable cases (see Figure 33). In addition, no specimen rupture event can be observed although the internal pressure has been increased to an extremely high level (15000MPa), indicating a stable crack growth behavior that results in complete crack arrest. Note that the simulations run to 15000MPa while no further evidence of crack extension is observed. Hence, Figure 35 focus on the first 50MPa. This complete crack arrest contrasts with LEFM predictions (Yoshioka et al. Submitted), which predict that once the crack growth momentarily arrests at a stable length, crack growth will recommence after a relatively small additional increase in pressure. However, this stable crack growth can be explained by the change of stress concentration shown in the right column of Figure 35. Here it is shown firstly that the largest tensile stress concentration occurs at the borehole rather than the crack tip, calling into question whether the rupture would actually occur at the well rather than notch tip.

Besides this, it is apparent that the proportional increasing of both the internal and external pressure is not leading to an expansion in the size of the region at crack tip in which there is a tensile stress concentration. This is unlike the unstable growth cases where the final instability is observed to be associated with expansion of the zone of the tensile stress concentration (recalling Figure 33 as well as forthcoming Figure 37). Hence, unlike LEFM model, the CZ model is impacted by the shape of the tensile stress concentration because it determines the proportion of the cohesive zone that is subjected to tensile traction that can lead to damage and breakage stays unchanged and eventually becomes so small that the crack no longer grows.

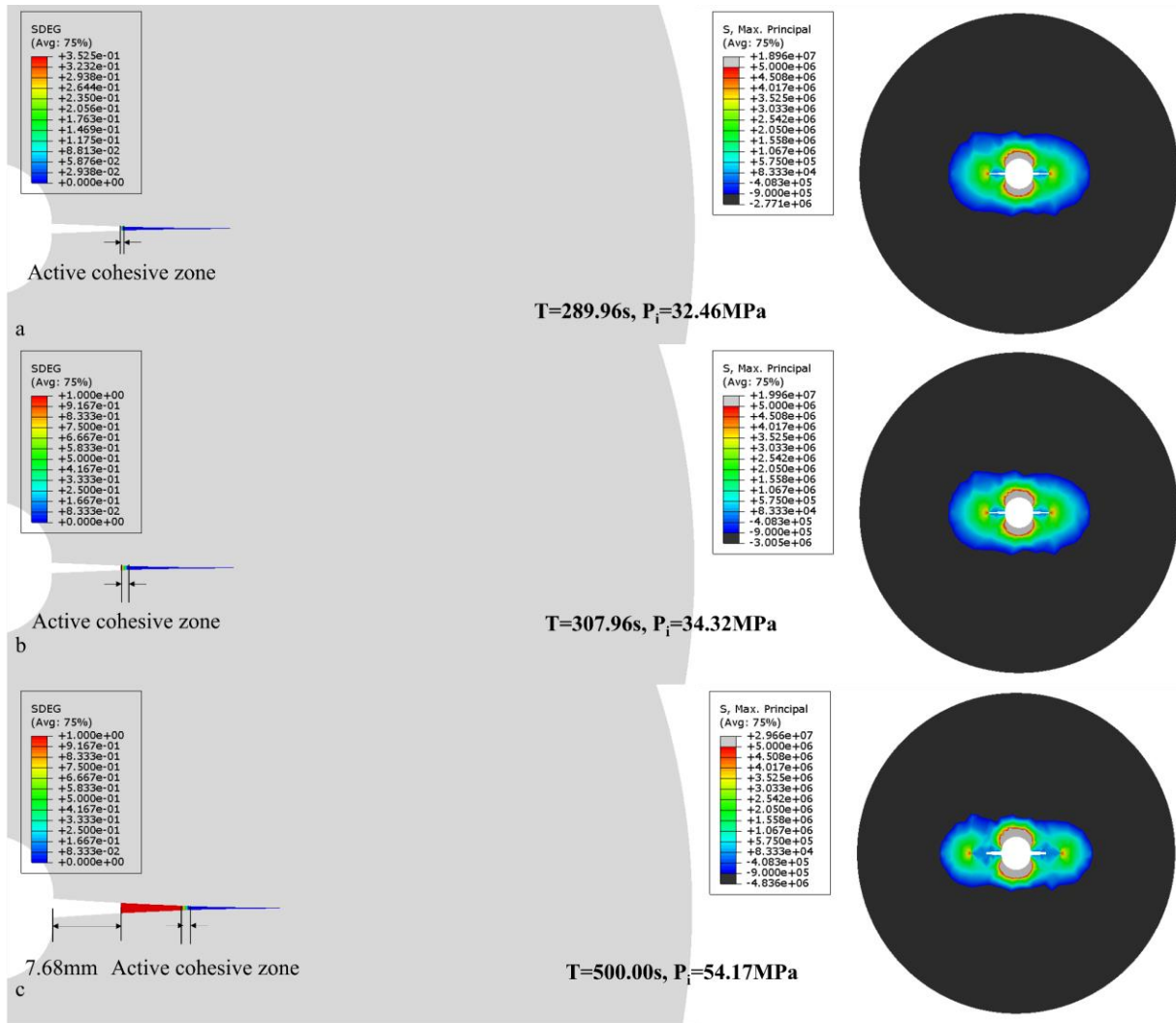


Figure 35 Simulation results showing the open cohesive elements and maximum principal stress contour for stable cases (1/2 inch borehole, showing the ratio of confining stress over internal stress is 1/8) at: a) 289.96s; b) 307.96s; c) 500.00s.

The stable crack growth is also confirmed and illustrated by plotting fracture width and crack length versus internal pressure loading, shown in Figure 36. In contrast with the unstable cases, there is no sudden jump in any of the curves, reflecting a stable crack growth. Instead, a gentler inflection point is observed. It can also be seen from Figure 36 that the fully broken CZ start to appear at the internal pressure corresponding to this inflection point. Moreover, the crack

width at the notch tip reaches the complete failure δ_f at the same pressure. Therefore, the internal pressure corresponding to this inflection point is picked as the predicted burst pressure from CZ-based simulations for stable cases (see Figure 36) and is compared with the burst pressure inferred from lab experiments in later discussions.

Notably, Zhang (2019) chose the peak pressure from pressure data recording from the lab experiment (see Figure 30) to be the burst pressure for stable cases since this peak pressure is considered to reflect the specimen rupture. However, the simulation result (see Figure 35 and 36) suggests there is no burst event corresponding to sudden crack growth in stable cases. For the experiments, it appears possible that the expanding crack width eventually accommodates extrusion of the membrane and therefore the rupture event occurs at a pressure corresponding to membrane breakage. If this is the mode of failure, then the burst event cannot be directly related to crack extension. We therefore note that in all experimental cases the membrane ruptures, the question is whether the rock fracture precedes or follows this membrane rupture. For unstable cases it appears reasonable to assume membrane rupture follows rock breakage, but for stable cases it is not so clear. For this reason, the burst pressures obtained from lab experiments for stable cases are modified in this study by picking the inflection pressure with the AE test data curve (see Figure 30), which is available for test 3 only, and laboratory tests 4 and 5 are considered ambiguous because they do not have AE data in order to ascertain the point of crack growth.

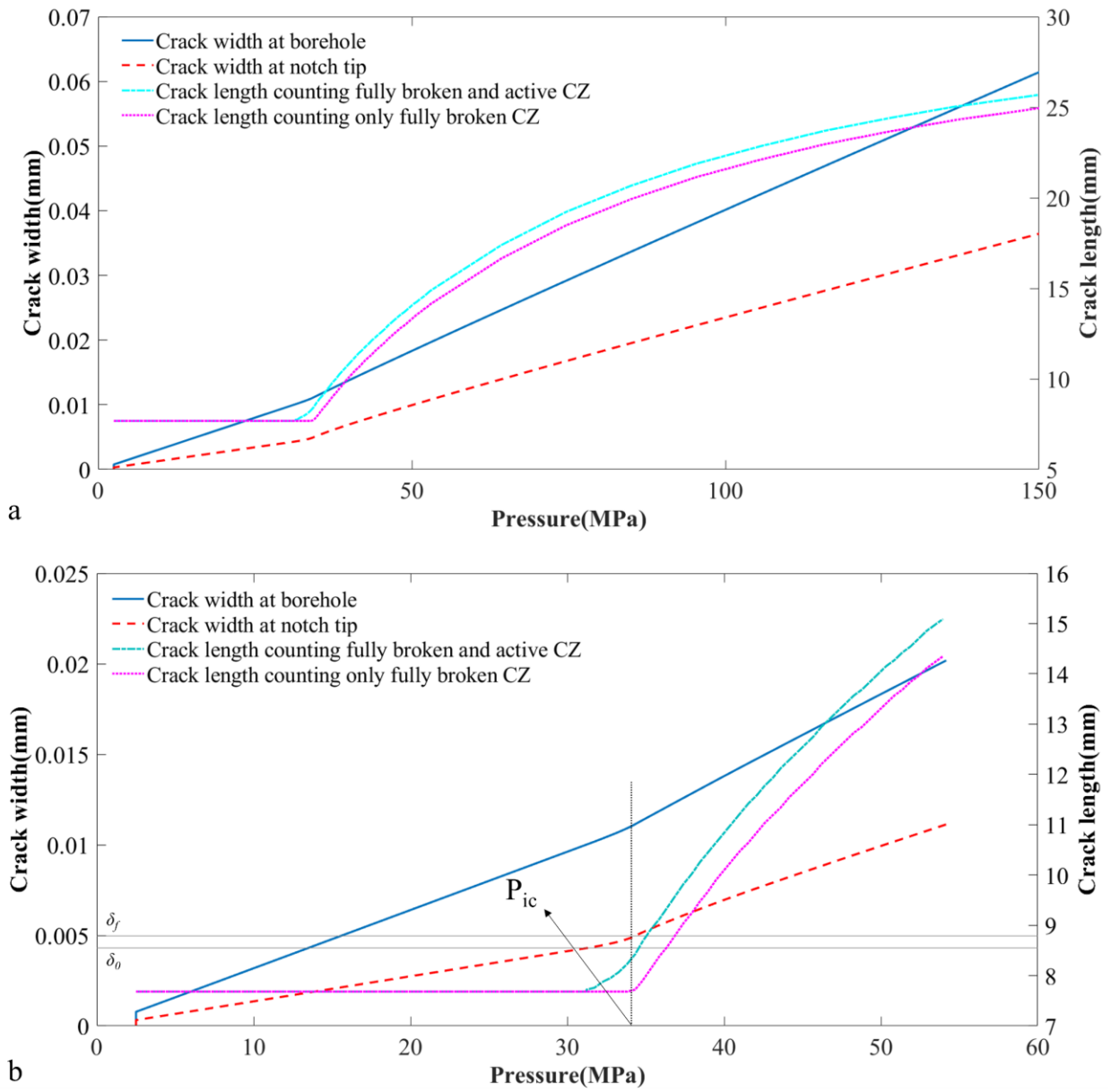


Figure 36 Crack opening versus internal pressure curve for CZ-based simulation of stable cases (1/2 inch borehole, showing the ratio of confining stress over internal stress is 1/8). a) showing the entire data with pressure increased to 150MPa; b) focusing on the first 50MPa with P_{ic} labelled.

4.6.3 Unconfined Partially Stable Cases

Laboratory tests 1 and 2, with a 0.5 inch borehole and no confining stress, are categorized as stable according to LEFM owing to the non-monotonic increase of stress intensity factor with increasing pressure (Yoshioka et al. submitted). However, the CZ simulations show crack growth behavior that shares some common features with unstable cases and other features with stable cases. Hence, these tests are more accurately defined as partially unstable cases. Specifically, these tests are similar to the stable cases in that the crack length propagates away from the loaded borehole and, at the beginning, the largest tensile stress concentration occurs at the borehole rather than the crack tip. However, unlike the fully stable cases, there is no pressure applied to the external boundary of the specimen that is increasing in proportion to the internal borehole pressure, and so the tensile zone is not as greatly suppressed and, eventually the tensile stress concentration region at the crack tip expands sufficiently to induce rapid crack growth to the boundary of the specimen.

To see how this partial instability manifests in some detail, simulation results for tests 1 and 2, showing the open cohesive elements and the maximum principal stress contours, are presented in Figure 37. These results show the evolution of crack geometry and stress concentration of the whole geometry, which corresponds in each time to a certain internal borehole pressure (see Figure 37). The left column of Figure 37 shows the change of deformed CZ elements during the crack propagation, color coded based on the SDEG value. Here it is observed that none of the CZ elements are fully broken before $T=127.58s$, $P_i=13.18MPa$ (see Figure 37b). The evolution of the active CZ, labelled from Figure 37a to 37b, indicates that the active CZ length is increasing as internal pressure increases before the fracture approaches the edge. Moreover, once the crack reaches approximately halfway to the edge at $T=128.14s$, $P_i=13.24MPa$ (see Figure 37c), it takes only 0.02s longer to fully reach the edge. This rapid growth is similar to what was observed

in the prior unstable cases and can be interpreted to correspond to generation of an expanded tensile stress concentration in the tip region based on observation of the maximum principal stress contours (see the right column of Figure 37).

Based on these results, two distinguishable stages are observed in the crack propagation (see Figure 37). In the first stage, the maximum principal stress concentration is located at the borehole, (see Figure 37a and 37b), with relatively smaller tensile stress at the notch tip. This smaller tensile stress concentration apparently leads to stable crack growth and is indeed similar to the stress distributions observed in simulation results for stable cases except that the crack grows much faster for the unconfined tests than for the fully stable confined tests with 0.5 inch borehole. Then, as the fracture propagates, the magnitude of stress concentration at the borehole starts to decrease at the crack tip (see Figure 37c). This stage is similar to the stage observed in unstable cases, leading to the unstable crack growth behavior discussed above. Furthermore, the crack accelerates to the specimen edge rapidly within 0.02s once the maximum stress concentration appears at the crack tip. Hence, the unconfined 0.5 inch borehole cases possess commonality with both the stable and unstable cases and are thus referred to as “partially stable cases” (or, equivalently, “partially unstable cases”).

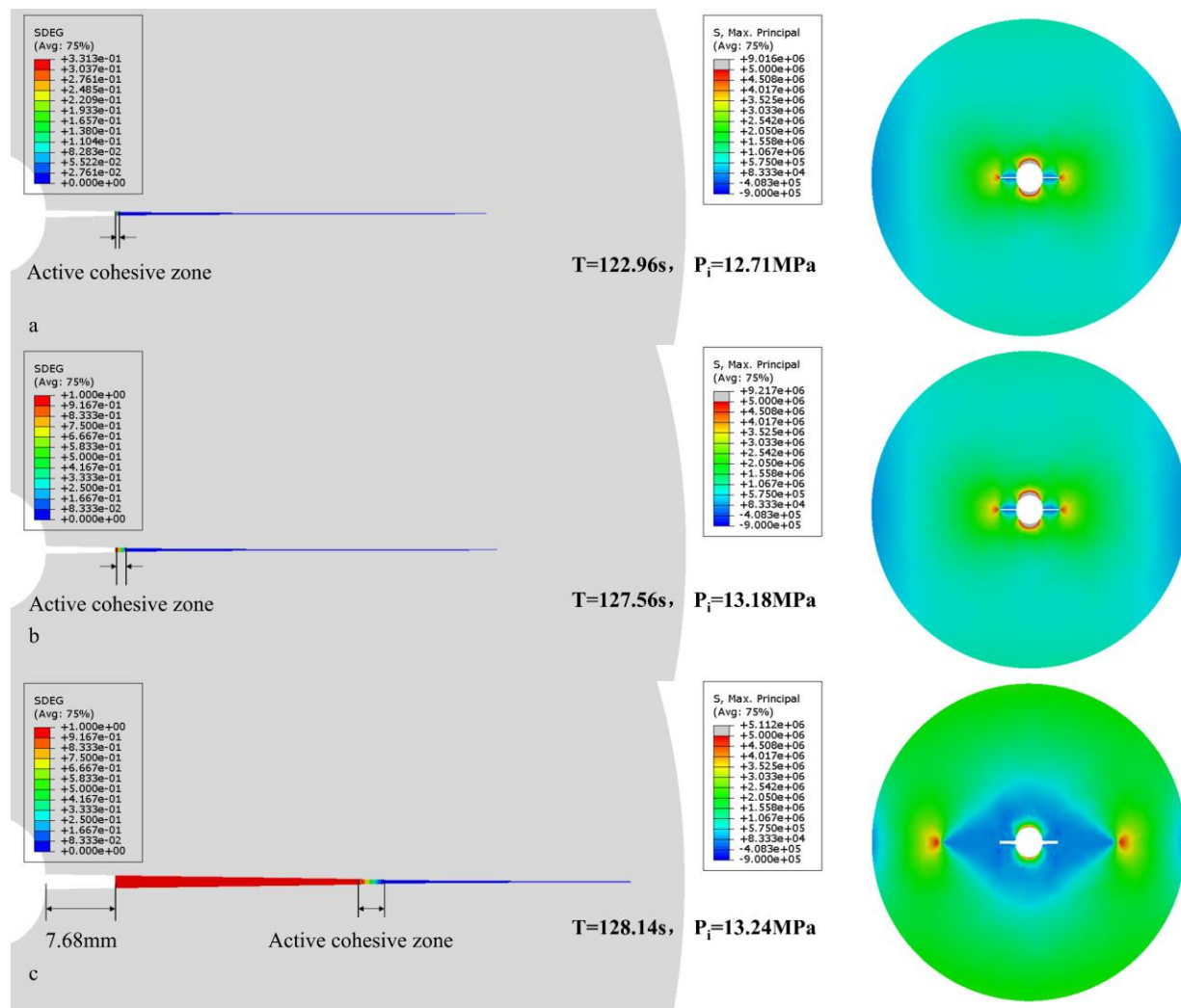


Figure 37 Simulation results showing the open cohesive elements and maximum principal stress contour for tests 1 and 2 (unconfining test with ½ inch borehole) at: a) 122.96s; b) 127.58s; c) 128.14s.

The fracture width and fracture length versus internal pressure loading behavior also indicates a period of stable growth followed by instability (see Figure 38). As in previous cases, the change of active CZ length with pressure can be seen as the separation between the crack length defined according to the distance to the first damaged element ($SDEG > 0$) and the crack length defined according to the distance to the first fully broken element ($SDEG = 1$). Furthermore, all the four data curves show an initial period of slow, stable growth followed by a sudden jump, with all

curves inflecting at the same pressure (see Figure 38). This inflection to unstable crack growth occurs once the crack width at the notch tip reaches the value for complete failure δ_f (see Figure 38). With all of these observations, the internal pressure corresponding to this inflection is defined as the predicted burst pressure for comparison with the laboratory experiments. Additionally, because the sudden change is an unambiguous point of instability, the assumption is that the observed sudden drop in pressure in the experiments (which occurs because the pump providing internal pressure can no longer run quickly enough to sustain a constant ramp) gives the critical pressure that can be compared to the simulation. Hence, burst pressures of laboratory experiments for tests 1 and 2 are obtained by picking the peak pressure from the data (Zhang 2019).

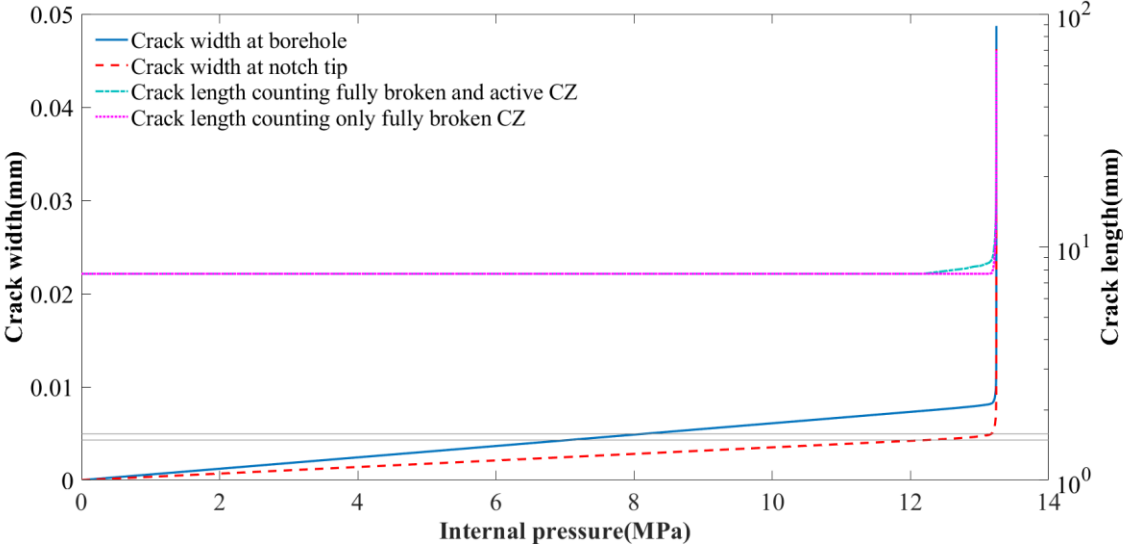


Figure 38 Crack width and length versus internal pressure with Pic labelled for CZ-based simulation of tests 1 and 2 (unconfining test with 1/2 inch borehole).

4.7 Comparison with Laboratory Experiments

Simulation results have demonstrated that the crack initiation and propagation behavior for burst experiments are affected by the size and confining stress conditions. The CZ-based simulation results have demonstrated that the crack grows unstably in unstable cases, i.e., laboratory tests 6-12, while the crack shows a stable propagation behavior for stable cases, i.e., laboratory tests 3-5. The crack propagation behavior of laboratory tests 1 and 2 is between unstable cases and stable cases. Furthermore, the simulation results for stable cases leads to a significant modification in picking burst pressure for current burst experiments. The burst pressures for lab test 3 is provided by an inflection in the AE event rate rather than the peak pressure from pressure data, as shown in Figure 30 (Zhang 2019).

The burst pressure P_{ic} , obtained in the laboratory experiment, is the key value to calculate the fracture toughness (see Eq. (4-1)). Hence, the comparison between the three parameter CZ-based simulation predictions and the laboratory data focuses on this quantity. Note that the stable case laboratory tests 4 and 5 are excluded from this comparison because there are no AE data and hence no way to unambiguously pick the critical pressure for crack propagation.

The comparison begins by optimally choosing the CZ parameters in order to obtain a best match in P_{ic} between the simulations and experiments. It begins by selecting initial (“prior”) values of the input parameters, as indicated in Table 3. Note that Table 3 shows the 3 independent CZ input parameters and, for convenience of comparison and interpretation, several quantities that are computed from these inputs. Then a search is undertaken to select CZ parameters that minimize the square root of the sum of the squared difference between the predicted and measured values of P_{ic} (RMS error). In principle this could be carried out through a formal genetic algorithm, grid search, or gradient-based search. In this case, because of the computational intensity of the

simulations (approximately 0.5 hours per evaluation on a single node of a supercomputer), the search is here carried out by hand following a quasi-gradient type of search method. Finally, one best combination of CZ element properties, as shown in Table 3, is found. The posterior fit of burst pressure P_{ic} obtained from three parameters CZ-based simulation with P_{ic} obtained from lab experiments is shown in Figure 39a, with the improvement over the prior apparent by comparison with Figure 39b.

We observe that most of the size/geometry effect and confinement effect are captured by this three parameter CZ model. This stands as a distinct improvement over the LEFM model where fracture toughness is taken as a constant value (Figure 39c). Hence, the CZ approach takes a major step towards capturing size/geometry and confinement effect on fracturing without resorting to *ad hoc* introduction of size and confinement dependent values of governing parameters. With that said, it is clear that only a very limited exploration of size effect is included here, and only via the changing borehole size so that size effect and specimen geometry effects are mingled together in the result. Nonetheless, the success of the model at capturing these impacts on crack initiation pressure comprises a promising move relative to alternatives such as ad hoc definition of size and geometry dependent values of fracture toughness.

As a further comparison, Figure 39d shows an LEFM approach where fracture toughness is fitted independently for each of the 5 experimental configurations that combine different hole sizes and confinement levels. As one would expect, the 5 parameter LEFM model matches the data very well, but it leaves uncertainty as to how to apply the model for a hole size and/or confinement level that was not directly addressed by the experiments. Also note that one could propose to introduce confinement dependent CZ element strength to improve the fitting the data to the experiments. However, the improvement provided by this approach is insignificant and does

not justify bringing an *ad hoc* treatment of size and confinement effect into the simulation methodology. Hence, the three parameter CZ-based simulations are found to suitably capture crack growth behavior for these lab experiments and, by doing this without need to introduce *ad hoc* stress and size dependency, they provide unique interpretation of fracture properties of the rock based on burst experiment data. Recalling also that the fracture toughness K_{Ic} can be computed by the CZ element energy G_c using Eq. (4-2), we find that the three parameters CZ simulation can provide estimation of an intrinsic fracture toughness (see Table 3). Interestingly, the best fit value of K_{Ic} for the LEFM model that assumes a single value of K_{Ic} for all cases is $0.73 \text{ MPa m}^{1/2}$, which is very similar to the value of $0.77 \text{ MPa m}^{1/2}$ that is found based on the best fit of the 3 parameter CZ model, which is, in turn, consistent with the value of $0.77 \text{ MPa m}^{1/2}$ found by unconfined semi-circular bending tests (Lu et al. 2020).

Table 8 CZ element properties.

		Formula	Prior	Posterior
Basic CZ properties	G_c (N/m)		41.35	12.10
	T_{max} (MPa)		7.93	4.87
	α		0.86	0.87
Computed properties	Fracture toughness (MPa.m ^{1/2})	$G_c = \frac{K_{Ic}^2(1 - \nu^2)}{E}$	1.43	0.77
	Irwin length (mm)	$l_r = \frac{K_{Ic}^2}{T_{max}^2}$	32.54	25.19
	δ_0 (μm)	$\delta_0 = \frac{2\alpha G_c}{T_{max}}$	9.00	4.30
	δ_f (μm)	$\delta_f = \frac{2G_c}{T_{max}}$	10.43	4.97

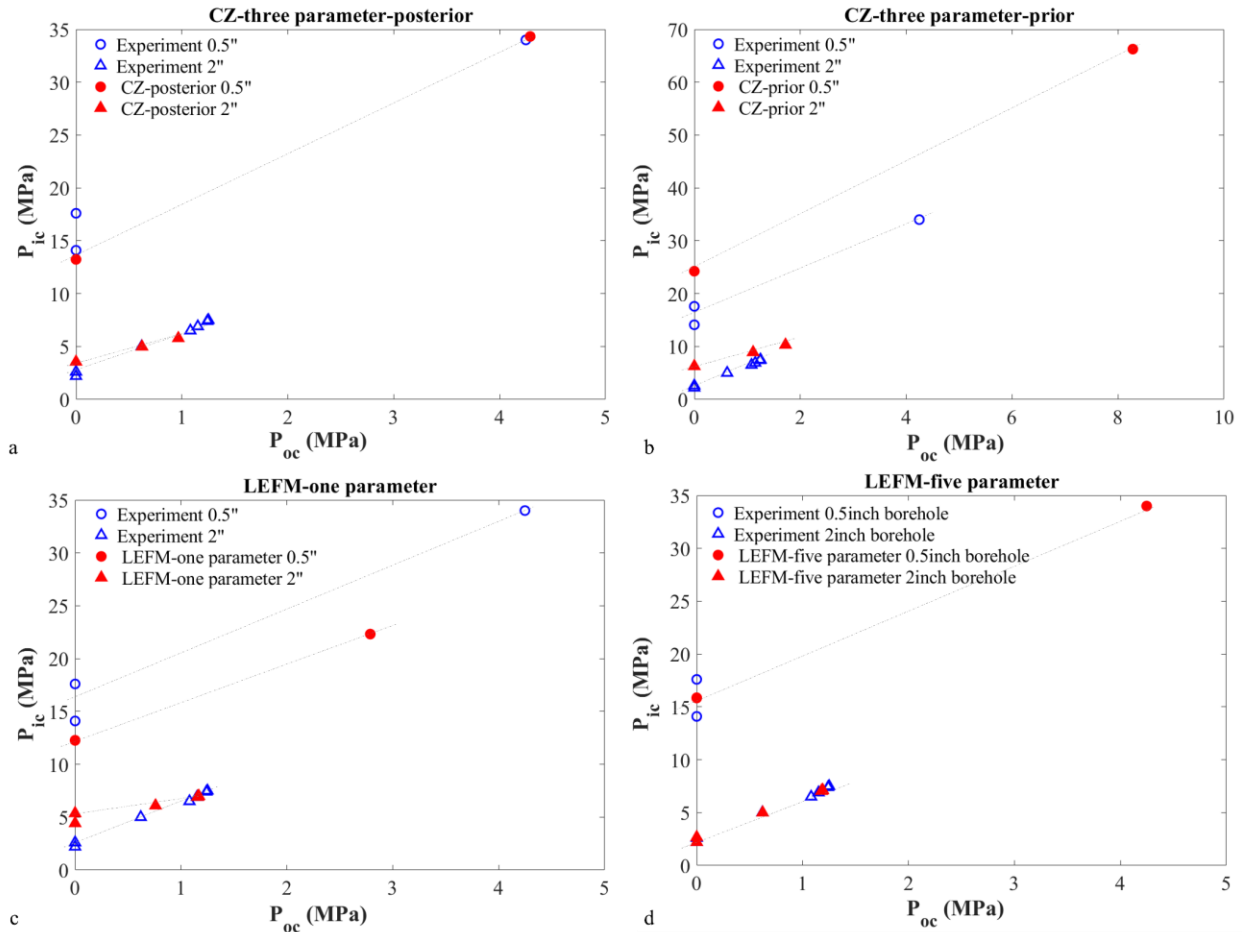


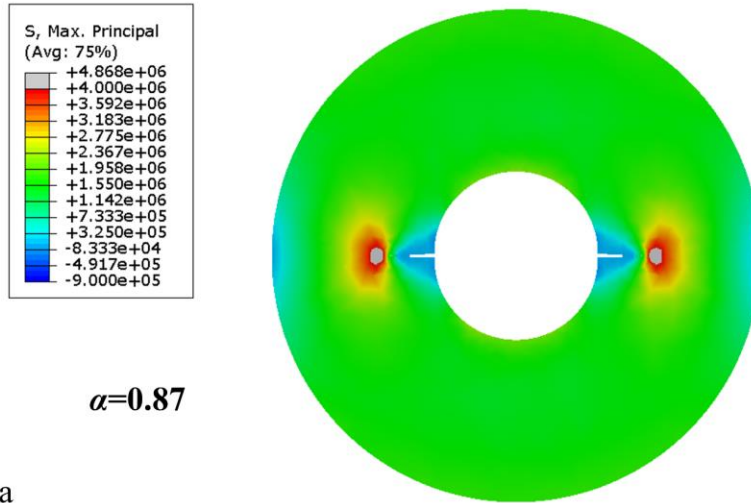
Figure 39 Comparison of burst pressure obtained from experiments and CZ-based simulations as well as LEFM methods. Note that KIC for the one parameter LEFM model is taken as 0.73

4.8 Discussion of T-S Law

The simulation results shown in Figure 33-38 are based on a critical separation ratio $\alpha \approx 1$ (recall Figure 31). The reason for this choice has been provided in the previous comparison of predicted burst pressure to observed critical internal pressure P_{ic} , and it corresponds to rock fracture for which the softening slope is much steeper compared to the elastic stiffness. However, it is useful to also observe that the critical separation ratio α has an impact on the qualitative

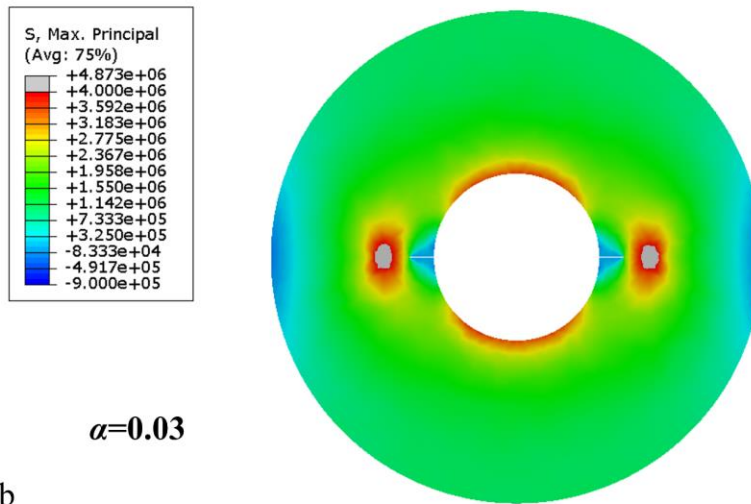
behavior of these confined unstable cases. Specifically, for a critical separation ratio $\alpha \approx 0$ (see Figure 40), which is the case where softening is gradual and most deformation is in the plastic part of the traction separation law, the stress concentration zone at the borehole is larger compared to the case for a critical separation ratio $\alpha \approx 1$. This difference leads to a prediction that the case with a small critical separation ratio tends to have a higher possibility to generate cracks at the orientation perpendicular to the notch direction than the case with a large critical separation ratio. In the future it will be of interest to investigate this propensity for oblique crack initiation and growth.

As discussed in previous section, we note that a combination of CZ elements with a large critical separation ratio α is demonstrated to provide a better fit compared to the combination with a small separation ratio, especially for stable case. In fact, through the fitting exercise carried out here, it is found that the separation ratio has negligible impact on the predicted burst pressure for unstable and partially stable cases. However, its impact on predicted burst pressure for stable cases is significant. So, from the perspective of the fitting, this separation ratio is a key quantity that allows the ability to capture burst pressure for stable cases. This observation implies that, provided AE detection is used to remove ambiguity in picking the crack propagation pressure in the experiments, the stable experimental cases provide an important part of an experimental campaign that is able to fully characterize a three parameter, bilinear traction-separation law for a given rock. We also note that for this rock, the Kasota Valley Limestone, the best fit with the large critical separation ratio implies that the traction separation law is most accurately depicted by a large elastic region and a small region of plastic softening (see e.g. Lecampion 2012 for a brief review of softening models with applications to rock mechanics CZ simulations).



a

$T=24.22s, P_i=4.98MPa, P_o=0.62MPa$



b

$T=24.21s, P_i=4.98MPa, P_o=0.62MPa$

Figure 40 Comparison of stress concentration of case8 at the same crack length 18.00mm under different critical separation ratio

4.9 Conclusions

Numerical simulation of burst experiments using cohesive zone elements leads to two main observations. The first is that the 3 parameter CZ model is able to suitably capture size/geometry and stress effect in the burst experiments without need to introduce *ad hoc* dependence of material properties on size and stress. Hence, the CZ model is more readily available to be applied at sizes and under stress conditions that are not directly considered in the laboratory. Secondly, the value of the fracture toughness computed from the three parameter CZ model is very similar to the value of fracture toughness required in order to obtain a best fit of an LEFM model to all experimental data under the restriction that a single value of the toughness be applied to all cases.

The present work therefore highlights the fact that application of LEFM to rock fracture, especially under conditions where the near-tip inelastic zone size is similar to the crack size, will result in a need to introduce a fracture toughness that is both size and stress dependent. By allowing interplay among size, stress, and the evolving inelastic zone near the crack tip, the CZ approach overcomes this limitation of LEFM-based simulations.

Besides capturing size/geometry and confining stress dependence of the burst experiment, CZ modeling demonstrates that the burst experiment has a limitation in capturing the crack initiation behavior for the typical burst experiment configuration. Perhaps most strikingly, the burst pressure obtained by picking the peak pressure on pressure data recording is not reflecting the actual specimen rupture. Recall that the burst experiment is pressurizing the pre-notched borehole through injecting fluid into the tube. So, there is a possibility that the membrane will be pushed into the notch due to the internal pressure, leading to a pressure rupture on the recorded pressure data curve. Furthermore, the CZ modelling shows no rupture on crack opening curve for

stable cases, which also exacerbates the ambiguity associated with the picking of burst pressure for the typical burst experiment configuration.

With that said, the fitting of the CZ model to the laboratory experiments highlights the potential for burst experiments to provide data for complete characterization of a three parameter (bilinear) traction-separation law. Here it is found to be advantageous to include cases with multiple hole sizes and confinement levels. It is also advantageous to include both stable and unstable configurations, but it is clearly also essential to include detection of crack growth (i.e. using acoustic emission monitoring) in order to find the critical pressure for the stable growth cases. Hence, this simulation and model-data fitting points a way forward whereby a modified burst experiment that uses multiple hole sizes and confinement levels can be used in combination with CZ modeling of the fracture process in order to completely characterize a suitable traction-separation law for a given rock in a manner that will enable simulation of rock breakage across a range of sizes and stress conditions that cannot be attained by LEFM owing to the lack of adherence of rock materials to the LEFM assumptions of negligibly small plastic zone and the fracture toughness being an intrinsic, unchanging material constant.

5.0 Conclusions

The crack initiation, propagation and interaction behavior of cracks emanating from a pressurized borehole are significant since these phenomena can be leveraged in order to estimate the maximum and minimum horizontal stresses from sleeve fracturing data and to evaluate the fracture toughness of rock with high confinement in laboratory experiments. By analyzing and thus quantifying the impact of in-situ stresses, specimen size/geometry and confining stress on crack growth behavior in sleeve fracturing and the burst experiment, this research paves the way for sleeve fracturing and the burst experiment to realize more reliable and insightful interpretation and hence wider applicability. The main contribution of this dissertation begins with providing a new numerical simulation model using plane-strain cohesive zone elements to investigate the fracture initiation and propagation behavior for sleeve fracturing problem. The model has been validated by benchmarking with both analytical solution and a laboratory test. The field-scale CZ simulations results bear similarity to predictions based on LEFM in the orientation of the first crack, which always initiates along the plane acted upon by the least compressive in-situ stress for $0 < \sigma_{hmin} / \sigma_{Hmax} \leq 0.93$. For cases with very similar horizontal stresses ($0.93 < \sigma_{hmin} / \sigma_{Hmax} \leq 1$), all the cracks initiate at the same internal pressure. However, the first crack initiates and grows steadily, without an instantaneous jump (in contrast to LEFM). In contrast to the consistent orientation of the first fracture, the opening direction of the second (and subsequent) fractures has been demonstrated to be varying with different in-situ stress combinations and CZ properties (in contrast to LEFM). Furthermore, the initiation pressure and location of fractures is systematically impacted by the in-situ stress conditions, pointing to a significant potential that simulations using

cohesive elements can be used to interpret field test data leading eventually to estimation of both the minimum and maximum horizontal far-field stress acting on a vertical wellbore.

Inspired by the remarkable fact that crack initiation and propagation behavior is systematically impacted by the maximum and minimum horizontal stress conditions, a new inversion algorithm is developed and validated to estimate both maximum and minimum horizontal stress for sleeve fracturing field test, which provided the second main contribution of this dissertation. The algorithm is based on an approximate model of fracture initiation with its basis in stress analysis around a wellbore. Simulations using FEM with Cohesive Zone elements predict inflection points in the wellbore deformation that enable straightforward identification of 5 key quantities that comprise the inputs to the inversion algorithm. The algorithm is validated using 100 sets of synthetic data generated by the FEM-CZ model, with most cases showing agreement between the estimated and actual values of both minimum and maximum horizontal stress within a few percent.

Finally, the present research provides a numerical simulation of burst experiments using cohesive zone elements which overcome the limitation of LEFM-based analyses. The 3 parameter CZ model is able to suitably capture size/geometry and stress effect in the burst experiments without introducing *ad hoc* dependence of material properties on size and stress. Hence, the CZ model is more readily available to be applied at sizes and under stress conditions that are not directly considered in the laboratory. Besides capturing size/geometry and confining stress dependence of the burst experiment, CZ modeling shows that, perhaps most strikingly, the burst pressure obtained by picking the peak pressure on pressure data recording is not reflecting the actual specimen rupture, thereby demonstrating that the burst experiment has a limitation in capturing the crack initiation behavior for the typical burst experiment configuration. Furthermore,

no rupture is observed on crack opening curve for stable cases in CZ modelling, which also exacerbates the ambiguity associated with the picking of burst pressure for the typical burst experiment configuration.

It is also interesting to observe that the laboratory test results were shown to be highly sensitive to the manner of load application and block size in sleeve fracturing test, by accounting for these details it is possible to obtain a reasonable match with experiments in both fracturing geometry (i.e. orientation of the secondary fracture) and the borehole pressure leading to both primary and secondary initiation. This match requires some adjustment of CZ properties, and further emphasizes the usefulness of such block experiments for model calibration to the particulars of the failure of given materials. This size and confinement effects are also observed from CZ simulation results for the burst experiment, pointing out a significant potential that simulations using cohesive elements can capture crack growth behavior of fractures emanating from a pressurized borehole, regardless of the specimen size and confinement level.

In summary, the research comprised in this dissertation shows both qualitatively and quantitatively the impact of in-situ stresses, borehole size and confining stress conditions on the crack initiation, propagation and interaction behavior of cracks emanating from a pressurized borehole. It predicts behavior with potential diagnostic importance for prediction of stresses, both minimum and maximum, based on data from sleeve fracturing experiments, and further provides a rapid, well-validated and sufficiently accurate inversion algorithm to estimate the maximum and minimum horizontal stress from sleeve fracturing test data. Furthermore, this research identifies the size and confining stress dependency of fracture toughness obtained from the burst experiments, and then provides a 3 parameter CZ model to capture the size/geometry and stress effect in the burst experiments without introducing *ad hoc* size and stress dependence.

Appendix A Extended Discussion of Lab Scale Simulation

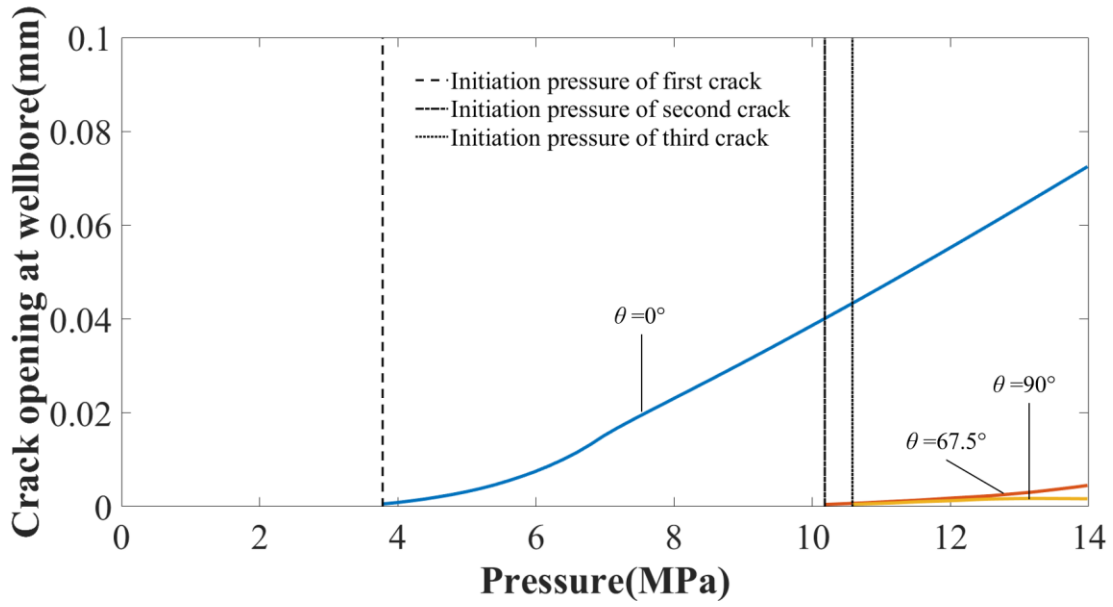
Assuming that the load application in the lab can be replaced with a far field stress in an infinite domain, A field-scale simulation with same material properties and in-situ stresses with lab-scale test is further provided to see if the results from lab experiments can predict the field test.

Appendix Figure 1 shows the crack initiation and propagation behavior predicted by this infinite domain numerical model. It is qualitatively similar to the behavior observed in the lab in that a primary crack growth in the plane upon which the smaller stress is acting. Also, upon increasing of the pressure inside the central hole, a secondary crack grows in the plane with angle 67.5° , although this secondary crack is suppressed much more quickly in the lab-scale model. Then, a tertiary crack initiates in the plane with angle 90° , as in the lab-scale model. The other 10 potential planes of crack growth did not show substantial fracturing, also in agreement with a lack of damage observed in the tested block.

The crack opening versus pressure loading is plotted in Appendix Figure 1, which provides the initiation pressure for the first, second crack and third crack. Indeed, the difference between the initiation pressure of the secondary and tertiary crack is very small. However, the secondary crack has not been suppressed by the tertiary crack, which is different from the lab-scale simulation results with finite domain where only the 90° crack grows. Furthermore, a comparison of initiation pressure for first and second crack between simulation and lab test (Table 5) indicates substantial deviation between the finite and infinite models, with the predicted pressure for primary crack growth with infinite domain simulation is about 54% higher than the finite domain lab experiment

and the predicted pressure for secondary crack growth with infinite domain simulation is about 82% higher than the finite domain lab experiment.

The block size was increased relative to the hole size until the finite domain simulation results effectively converge to the infinite domain results. Results are shown in Appendix Table 1. Convergence is observed when the hole size to block size ratio is 1/10, and even then, only when the pressure loading uniformly distributing along the whole boundary. Such a pressure distribution could be obtained with fluid-filled flat jack loading, but would not be expected when loading is applied with hydraulic pistons. Indeed, the details of the piston size (i.e. applied loading area) and thickness of the steel platens are observed through the experience of this study to have a strong effect on the predicted initiation pressures, and therefore are chosen to closely match the actual lab configuration. Still, even if ideal loading is applied, the block size requirement is problematic because the required hole size needed to provide space for the packer and its accompanying sensors means that a 10x larger block size is impractical. So, for most practical purposes, the comparison between finite domain and infinite domain results further emphasizes the significance of boundary conditions for lab-scale simulation. If one wishes to simulate the lab experiments, it is important to use a purpose-built simulator that accounts for the details of the boundary conditions rather than simply assuming that the lab experiments approximate an infinite domain.



Appendix Figure 1 Crack opening versus pressure loading for ABAQUS infinite domain, i.e. (incorrectly) assuming that the load application in the lab can be replaced with a far field stress in an infinite domain.

Appendix Table 1 Comparison of simulation results with lab test data for the pressure associated with first and second crack initiation.

Initiation pressure	Initiation angle for 2 nd crack	Initiation pressure for 1 st crack	Initiation pressure for 2 nd crack
Laboratory experiment results	90°	2.45MPa	5.59MPa
ABAQUS CZM finite domain (the hole size to block size ratio is 1/5 as in the actual lab configuration)	67.5°	2.46MPa	6.61MPa
ABAQUS CZM finite domain (the hole size to block size ratio is 1/10 with pressure uniformly distributing along the part of boundary)	22.5°	3.65MPa	4.14MPa
ABAQUS CZM finite domain (the hole size to block size ratio is 1/10 with pressure uniformly distributing along the entire boundary)	67.5°	3.78MPa	10.18MPa
ABAQUS CZM infinite domain	67.5°	3.78MPa	10.18MPa

The predicted initiation pressures are somewhat sensitive to CZ properties. To explore this sensitivity, lab-scale simulations with different cohesive element properties are carried out while the boundary and loading conditions are set to match the actual lab configuration. The comparison of these simulation results is listed in Appendix Table 2, which shows that all 3 properties impact

initiation pressures. Basically, the initiation pressure of first and secondary crack is increasing as α increases while the cohesive element strength and cohesive element energy G_c are held to be the same so that only α is varying. This approach is the same for G_c and T_{max} . Therefore, by comparing with initiation pressure of first and secondary crack observed from laboratory experiment results, one group of CZ properties is selected to be applied in the final lab-scale simulation (see Table 3). Then, the lab-scale simulation with actual lab configuration can provide initiation pressure that is the closest to the experiment results with this group of CZ properties.

Appendix Table 2 Comparison of lab-scale simulation results with different cohesive element properties for the pressure associated with first and second crack initiation.

α	T_{max}	G_c	Initiation angle for 2 nd crack	Initiation pressure for 1 st crack	Initiation pressure for 2 nd crack
0.003	2MPa	10.7N/m	67.5°	2.6MPa	6.8MPa
0.003	2MPa	32N/m	67.5°	3.37MPa	7.5MPa
0.003	1MPa	10.7N/m	67.5°	2.2MPa	6.1MPa
0.03	1MPa	10.7N/m	67.5°	4.2MPa	6.7MPa
0.003	1.5MPa	10.7N/m	67.5°	2.46MPa	6.6MPa

Appendix B Impact of In-Situ Stresses on Key Quantities

Simulation results for cases with varying stresses (Appendix Table 3) are shown in Appendix Figure 2. Initiation pressure of the first fracture under different in-situ stresses with the same material properties are shown in Table B1 while initiation pressure of the first crack for different cohesive element strength with the same in-situ stresses are presented in Table B2.

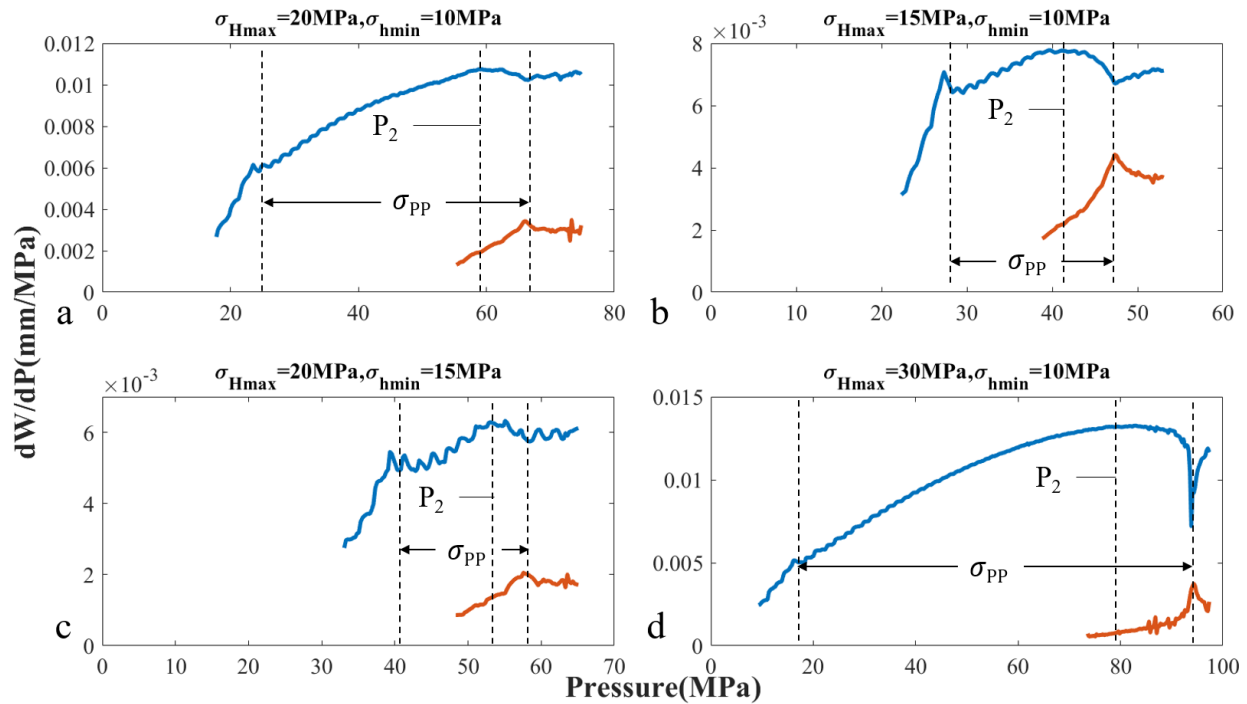
Appendix Table 3 P_I obtained by field-scale cases under different in-situ stresses.

σ_{Hmax}	σ_{hmin}	P_I
15MPa	10MPa	17MPa
20MPa	10MPa	12MPa
20MPa	15MPa	27MPa
30MPa	10MPa	5MPa

Appendix Table 4 P_I obtained by field-scale cases for different cohesive element strength.

T_{max}	P_I
1MPa	17MPa
2MPa	17MPa
4MPa	17MPa
10MPa	17MPa

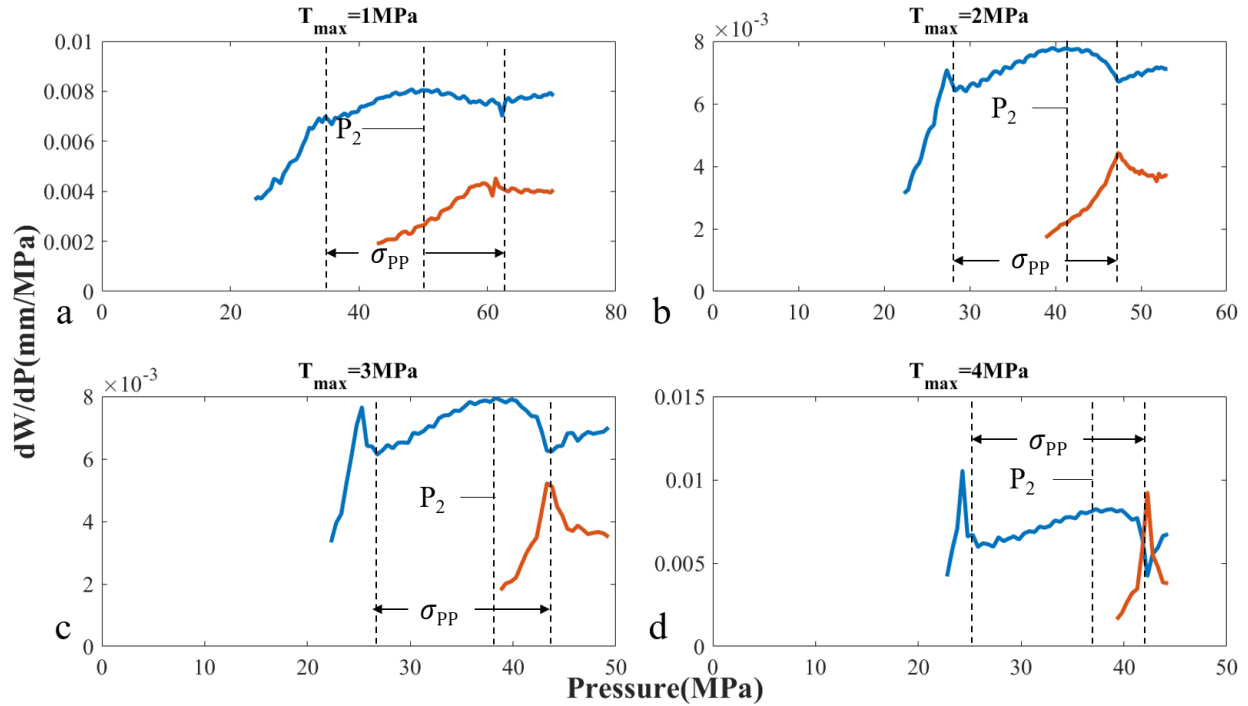
Besides obtaining the pressure for initial fracturing, the derivative of crack width at wellbore versus the pressure loading for cases under different in-situ stresses is plotted in Appendix Figure2 to obtain the P_2 and σ_{PP} . Appendix Figure2 shows that both P_2 and σ_{PP} value are varying with the combination of in-situ stresses, which provides the evidence that there is a relationship between the in-situ stresses and these two parameters. Additionally, the derivative of crack width at wellbore versus pressure loading for different cohesive element strength is also plotted in Appendix Figure3 to show how the P_2 and σ_{PP} are obtained. It can be seen from Appendix Figure3 that both P_2 and σ_{PP} values are varying with the cohesive element strength, which demonstrates the significance of T_{max} in interpreting the in-situ stresses.



Appendix Figure 2 Crack interaction behavior for field-scale under different in-situ stresses, with P_2 and σ_{PP}

labelled as an illustration for: a) $\sigma_{Hmax}=20\text{MPa}, \sigma_{hmin}=10\text{MPa}$; b) $\sigma_{Hmax}=15\text{MPa}, \sigma_{hmin}=10\text{MPa}$; c)

$\sigma_{Hmax}=20\text{MPa}, \sigma_{hmin}=15\text{MPa}$; d) $\sigma_{Hmax}=30\text{MPa}, \sigma_{hmin}=10\text{MPa}$.



Appendix Figure 3 Crack interaction behavior for field-scale for different cohesive element strength, with P_2 and σ_{PP} labelled as an illustration for: a) $T_{max}=1\text{MPa}$; b) $T_{max}=2\text{MPa}$; c) $T_{max}=3\text{MPa}$; d) $T_{max}=4\text{MPa}$.

Taken together, comparison of field-scale simulation results from section Appendix B demonstrates the impact of in-situ stresses on the four key quantities, including P_1 , θ , P_2 and σ_{PP} . Indeed, as expected, the simulation shows that these four key quantities are all sensitive to the change of in-situ stresses. This variability of key quantities provides an assumption that there is a relationship between the key quantities and in-situ stresses which can be applied to interpret the in-situ stresses by finding key quantities from the field test data. Moreover, the P_2 and σ_{PP} values are also showing sensitivity to the cohesive element strength while the T_{max} can be related to the material tensile strength. Therefore, the T_{max} (the tensile strength of the rock or, in the model, the cohesive element strength) should also be considered as a key quantity. In the end, the most important observation is that with known material tensile strength, the key quantities picked from the data curve of simulation results by locating the inflection points are proved to have a

relationship with combination of in-situ stresses. Indeed, such inflection points have already been observed from quarry test data of sleeve fracturing (Ohanian et al. 2021), pointing to high potential that these key quantities can be applied to interpret actual field test data and eventually estimate the maximum and minimum horizontal stress.

Appendix C Picking Key Quantities for Illustrative Cases

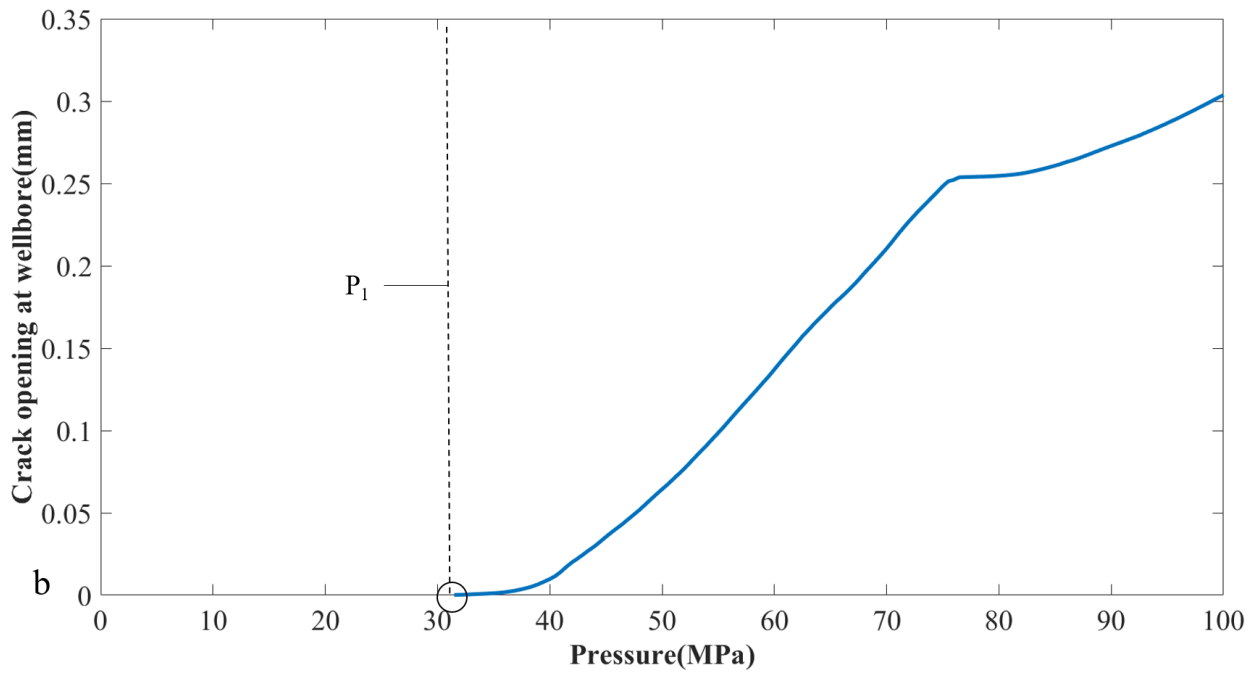
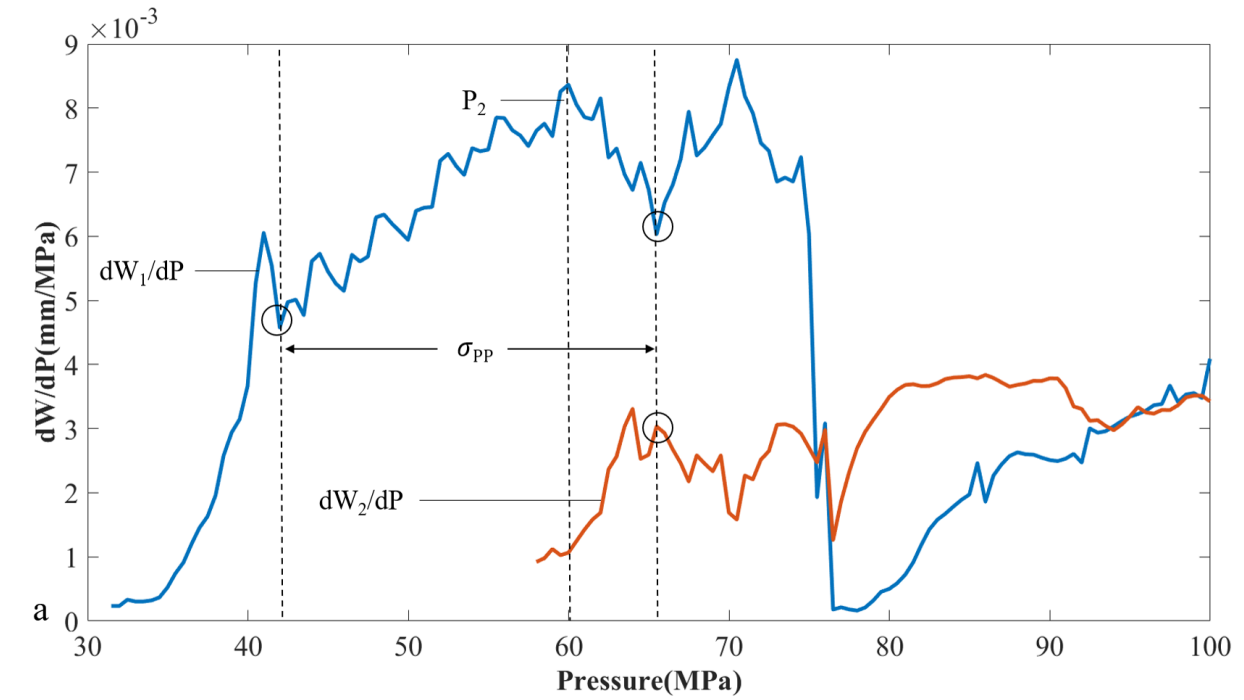
This section shows four illustrative cases that do not adhere as strictly to the pattern in Figure 22 and how to pick the key quantities for these cases. This illustration shows that, even for non-ideal cases, picking key quantities to the best of one’s ability (Appendix Table 5 shows the picks corresponding to Appendix Figures 4-7) leads to reasonably accurate stress estimates. Notably, Appendix Figure 7 shows the special case with several cracks initiating at the same time. For such cases, the maximum horizontal stress can be assumed to be equal to the minimum horizontal stress. Then, the in-situ stresses can be calculated by Eq. (3-6) with P_1 and T_{max} . The comparison between the estimated and actual in-situ stresses for these four non-ideal cases are shown in Appendix Table 6. In addition, the data curve generated from quarry test (Ohanian et al. 2021) is extremely similar to the data curve shown in Appendix Figure 5 with all the inflection points required for the application of the inversion algorithm, leading to the confidence in estimating in-situ stresses from the actual sleeve fracturing field data.

Appendix Table 5 Key quantities for four example cases

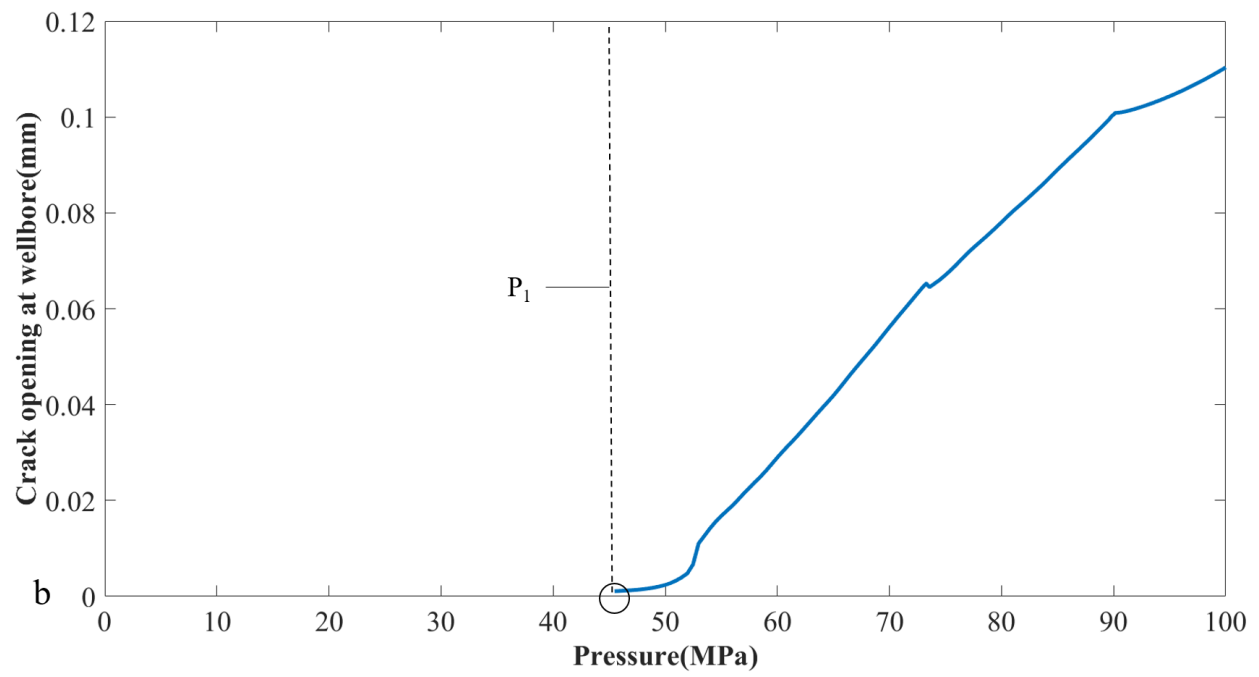
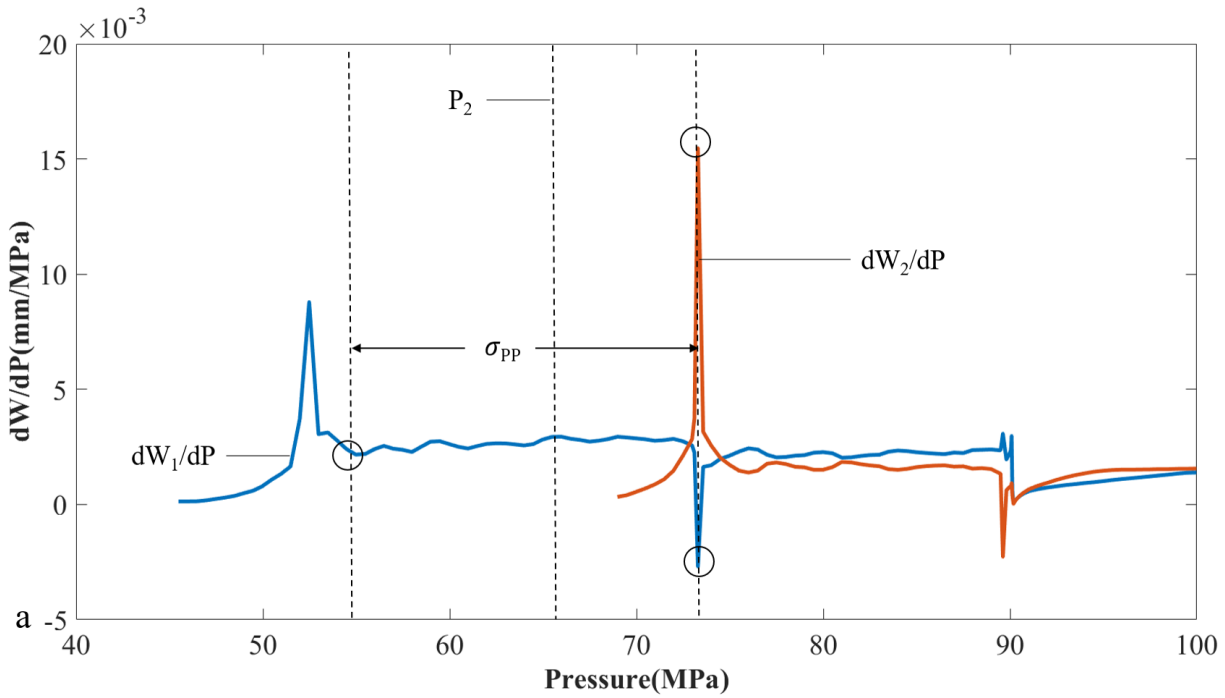
	θ (°)	P_1 (MPa)	P_2 (MPa)	σ_{PP} (MPa)	T_{max} (MPa)
Case10	22.5	31	60	23.5	3
Case15	45	45.5	66	18.3	9
Case30	67.5	32	39.5	11	8
Case97	N	91.5	N	N	6

Appendix Table 6 Comparison of estimated and actual in-situ stresses for four example cases

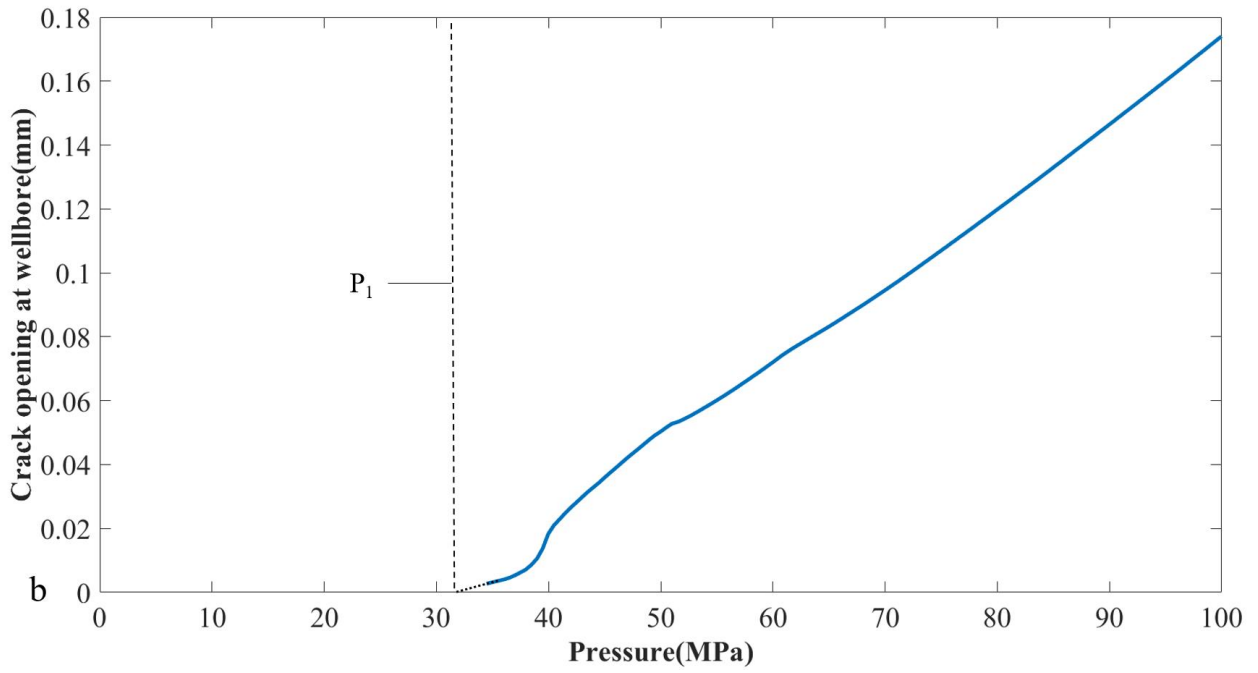
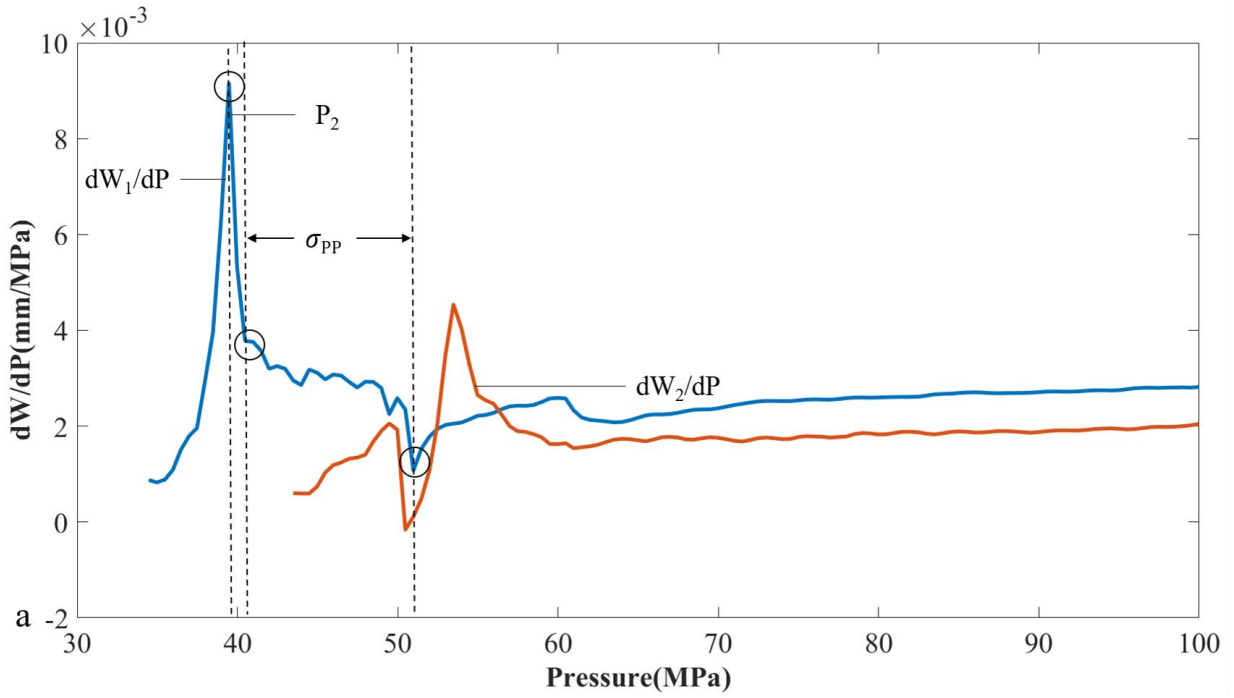
	Estimated σ_{Hmax} (MPa)	Actual σ_{Hmax} (MPa)	Estimated σ_{hmin} (MPa)	Actual σ_{hmin} (MPa)
Case10	35.75	35.77	22.17	21.26
Case15	27.8	27.03	21.41	21.18
Case30	13.4	14	11.39	12.66
Case97	42.78	42.78	42.77	42.77



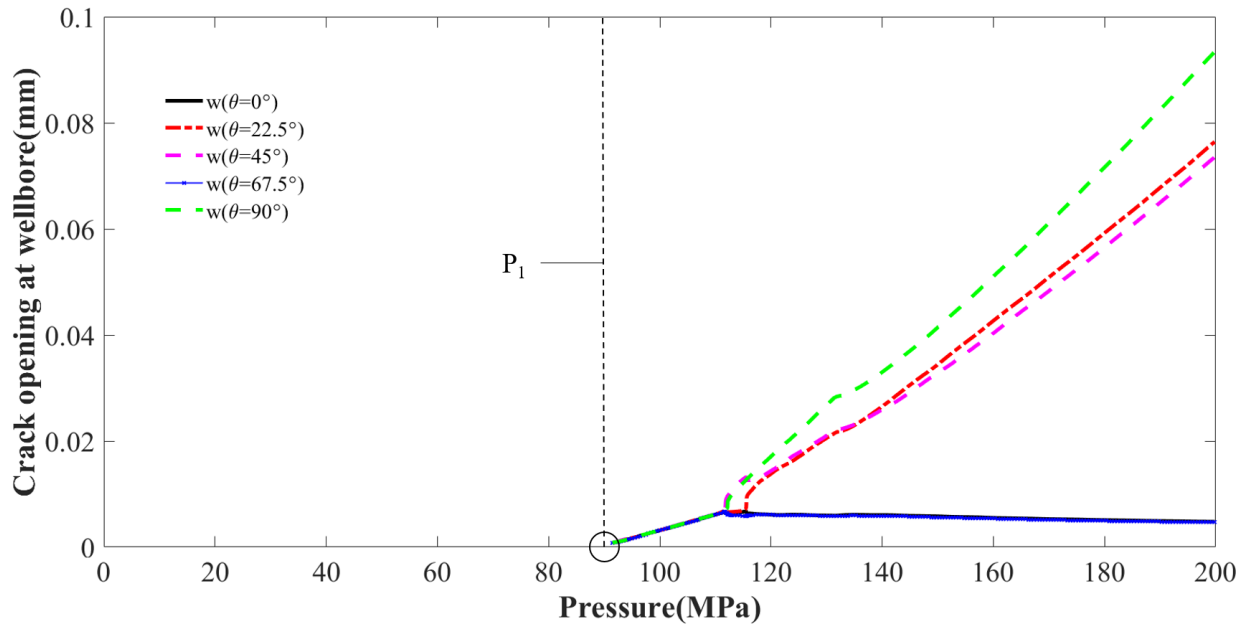
Appendix Figure 4 Data curves with key quantities labelled for Case 10 showing: a) P_2 and σ_{PP} ; b) P_1 .



Appendix Figure 5 Data curves with key quantities labelled for Case 15 showing: a) P_2 and σ_{PP} ; b) P_1 .



Appendix Figure 6 Data curves with key quantities labelled for Case 30 showing: a) P_2 and σ_{PP} ; b) P_1 .



Appendix Figure 7 Data curve for Case 97, with P_1 quantity labelled.

Appendix D Values Corresponding to Figure 24 and 25

This section contains three tables showing the values corresponding to Figure 24 and 24 in major text. Figure 24 compares the impact of uncertainty level of different key quantity on the accuracy in estimation for horizontal stresses and further labelled the confidence interval for estimated horizontal stresses for the illustrative case. Appendix Table 7 shows the mean, standard deviation, and coefficient variation corresponding to each curve shown in Figure 24. Then, the Figure 25 is aiming showing the relationship between the uncertainty level for estimating horizontal stresses and the angle between the first and secondary cracks. The mean, standard deviation, and coefficient variation corresponding to three representative cases with different θ and 5% uncertainty level for P_2 are shown in Appendix Table 8. Appendix Table 9 compares the uncertainty level of estimated horizontal stresses by choosing different uncertainty level for P_2 .

Appendix Table 7 Comparison of mean and standard deviation for estimated in-situ stresses varying different key quantities for illustrative case (see Figure 24 in major text).

	Varying only θ	Varying only P_1	Varying only P_2	Varying only σ_{PP}	Varying only T_{max}	Varying All
Mean of estimated σ_{Hmax} (MPa)	14.26	14.25	14.25	14.25	14.25	14.26
Standard deviation of estimated σ_{Hmax} (MPa)	0.32	0.084	1.66	0.3	0.025	1.72
Coefficient variation of estimated σ_{Hmax}	2.2 %	0.6%	11.6%	2.1%	0.2%	12%
Mean of estimated σ_{hmin} (MPa)	9.75	9.75	9.75	9.75	9.75	9.75
Standard deviation of estimated σ_{hmin} (MPa)	0.11	0.084	0.56	0.1	0.025	0.58
Coefficient variation of estimated σ_{hmin}	1.1%	0.86%	5.7%	1%	0.26%	6%

Appendix Table 8 Comparison of mean and standard deviation for estimated in-situ stresses varying all the key quantities for three illustrative cases with 5% uncertainty level for P_2 (see Figure 25 in major text).

	Case 10 ($\theta=22.5^\circ$)	Case 15 ($\theta=45^\circ$)	Case 30 ($\theta=67.5^\circ$)
Mean of estimated σ_{Hmax} (MPa)	35.84	26.66	14
Standard deviation of estimated σ_{Hmax} (MPa)	7.99	2.53	0.86
Coefficient of variation of estimated σ_{Hmax}	22%	9.5%	6.1%
Mean of estimated σ_{hmin} (MPa)	21.28	21.05	12.67
Standard deviation of estimated σ_{hmin} (MPa)	2.64	0.88	0.39
Coefficient of variation of estimated σ_{hmin}	12%	4.2%	3.1%

Appendix Table 9 Comparison of mean and standard deviation for estimated in-situ stresses varying all the key quantities for three representative cases with different uncertainty level for P_2 .

	Case 10 ($\theta=22.5^\circ$)	Case 15 ($\theta=45^\circ$)	Case 30 ($\theta=67.5^\circ$)
Uncertainty of estimated σ_{Hmax} with uncertainty of P_2 (5%)	22%	9.5%	6.1%
Uncertainty of estimated σ_{Hmax} with uncertainty of P_2 (2%)	10%	4.2%	2.6%
Uncertainty of estimated σ_{hmin} with uncertainty of P_2 (5%)	12%	4.2%	3.1%
Uncertainty of estimated σ_{hmin} with uncertainty of P_2 (2%)	5.7%	2.1%	2.3%

Bibliography

- ABAQUS (2011) ABAQUS Version 6.11 Analysis User's Manual. Dassault Systèmes Simulia Corp, Providence.
- Abou Sayed, A.S., 1978. An experimental technique for measuring the fracture toughness of rocks under downhole stress condition. VDI-Berichte 313, 819–824.
- Abou-Sayed, A.S., Jones, A.H., 1979. Process for measuring the fracture toughness of rock under simulated down-hole stress conditions. U.S. Patent No. 4,152,941. U. S. Patent and Trademark Office, Washington, DC.
- Arndt, S., Van der Zee, W., Hoeink, T., Nie, J., 2015, May. Hydraulic fracturing simulation for fracture networks. In: Proceedings of the SIMULIA Community Conference, Berlin, Germany, pp. 18–21.
- Barenblatt, G. I. (1962). The mathematical theory of equilibrium cracks in brittle fracture. *Advances in applied mechanics*, 7(1), 55-129. Author's last name, first initial. (Publication date). Book title. Additional information. City of publication: Publishing company.
- Bazant, Z. P., & Planas, J. (1997). *Fracture and size effect in concrete and other quasibrittle materials* (Vol. 16). CRC press.
- Chandler, N. (1989): An energy approach to sleeve fracture stress measurements. Ph. D. Dissertation, University of Manitoba, Winnipeg.
- Charsley, A. D., Martin, C. D., & McCreath, D. R. (2003). Sleeve-fracturing limitations for measuring in situ stress in an anisotropic stress environment. *International Journal of Rock Mechanics and Mining Sciences*, 40(1), 127-136.
- Detournay E, Jeffrey RG. Stress conditions for initiation of secondary fractures from a fractured borehole. In: Proceedings of the International Symposium on Rock Stress and Rock Stress Measurements, Stockholm, 1986. p. 281–8.
- Dugdale, D. S. (1960). Yielding of steel sheets containing slits. *Journal of the Mechanics and Physics of Solids*, 8(2), 100-104.
- Feng, Y., Harrison, J.P., Bozorgzadeh, N., 2019. Uncertainty in in situ stress estimations: A statistical simulation to study the effect of numbers of stress measurements. *Rock Mech. Rock Eng.* 52 (12), 5071–5084.
- Funatsu, T., Seto, M., Shimada, H., Matsui, K., Kuruppu, M., 2004. Combined effects of increasing temperature and confining pressure on the fracture toughness of clay bearing rocks. *Int. J. Rock Mech. Min. Sci.* 41 (6), 927–938.

- Haimson, B.C., Cornet, F.H., 2003. ISRM suggested methods for rock stress estimation—part 3: hydraulic fracturing (HF) and/or hydraulic testing of pre-existing fractures (HTPF). *Int. J. Rock Mech. Min. Sci.* 40, 1011–1020.
- Hickman, S., Zoback, M.D., 2004. Stress orientation and magnitudes in the SAFOD pilot hole. *Geophys. Res. Lett.* 31, L15S12. <https://doi.org/10.1029/2004GL020043>.
- Heidbach, O., M. Rajabi, X. Cui, K. Fuchs, B. Müller, J. Reinecker, K. Reiter, M. Tingay, F. Wenzel, F. Xie, M. O. Ziegler, M.-L. Zoback, and M. D. Zoback (2018): The World Stress Map database release 2016: Crustal stress pattern across scales. *Tectonophysics*, 744, 484-498, <https://doi:10.1016/j.tecto.2018.07.007>.
- Huang Y, Zolfaghari N, Bungler A, 2022. Cohesive Element Simulations Capture Size and Confining Stress Dependence of Rock Fracture Toughness Obtained from Burst Experiments, *Journal of Mechanics and Physical of Solids*, Volume 160, 2022, 104799, ISSN 0022-5096, <https://doi.org/10.1016/j.jmps.2022.104799>
- Huang Y, Zolfaghari N, Ohanian III J, Bungler A, 2021. Technical Note: An inversion algorithm to estimate maximum and minimum horizontal stress based on field test data for sleeve fracturing, *Computers and Geotechnics*, Volume 137, 2021, 104274, ISSN 0266-352X, <https://doi.org/10.1016/j.compgeo.2021.104274>.
- Huang, Y, Zolfaghari, N, Ohanian, O.J, Bungler A. 2021. Numerical Simulation of Sleeve Fracturing for In Situ Stress Measurement Using Cohesive Elements and Its Implications. *Rock Mechanics and Rock Engineering*, 54, 4505–4522 (2021).<https://doi.org/10.1007/s00603-021-02554-4>
- Hubbert, M. K. and Willis, D. G.: "Mechanics of Hydraulic Fracturing", *Trans., AIME-* (1957) 210, 153.
- Irwin, G., 1957. Analysis of stresses and strains near the end of a crack traversing a plate. *J. Appl. Mech.* 24.
- Kirsch, C. (1898). Die theorie der elastizitat und die bedurfnisse der festigkeitslehre. *Zeitschrift des Vereines Deutscher Ingenieure*, 42, 797-807.
- Labuz, J.F., Shah, S.P., Dowding, C.H., 1987. The fracture process zone in granite: evidence and effect. *Int. J. Rock Mech. Mining Sci. Geomech. Abs.* 24 (4), 235–246. Pergamon.
- Lecampion, B. (2012). Modeling size effects associated with tensile fracture initiation from a wellbore. *International Journal of Rock Mechanics and Mining Sciences*, 56, 67-76.
- Lin, Q., Labuz, J.F., 2013. Fracture of sandstone characterized by digital image correlation. *Int. J. Rock Mech. Min. Sci.* 60, 235–245. Lu, G., Gordeliy, E., Prioul, R., Aidagulov, G., Uwaifo, E.C., Ou, Q., Bungler, A.P., 2020. Time-dependent hydraulic fracture initiation. *J. Geophys. Res.* 125 (3), e2019JB018797.

- Ljunggren, C., Chang, Y., Janson, T., & Christiansson, R. (2003). An overview of rock stress measurement methods. *International Journal of Rock Mechanics and Mining Sciences*, 40(7-8), 975-989.
- Lu, Q., Lu, G., Bungler, A.P., Prioul, R., Aidagulov, G., 2017. Impact of fluid acidity on the time-dependent initiation of hydraulic fractures in carbonate rocks. In: Proceedings 51st U.S. Rock Mechanics/Geomechanics Symposium, San Francisco, California, USA, June. American Rock Mechanics Association. ARMA 17-0200.
- Lu, Q., 2016. Hydraulic Fracture Initiation In Limestone. University of Pittsburgh. Master dissertation. Papanastasiou, P.C., 1997. A coupled elastoplastic hydraulic fracturing model. *Int. J. Rock Mech. Min. Sci.* 34 (3-4), 240. -e1.
- Ohanian III J, Huang Y, Zolfaghari N, Bungler A, 2021. High-Resolution Distributed Fiber Optic Measurement of Borehole Fractures to Enable In-situ Stress Measurement. Proceedings of the 55TH US Rock Mechanics / Geomechanics Symposium, 2021. 20-23 June 2021, Houston, Texas, 20-A-1386-ARMA.
- Ohanian, O. J., VandenBerge, D. R., Davis, M. A. (2019). “Distributed measurement of minimum and maximum in-situ stress in substrates”, US Patent Application US20190064387A1.
- Papanastasiou, P., 1999. The effective fracture toughness in hydraulic fracturing. *Int. J. Fract.* 96 (2), 127–147.
- Papanastasiou, P., Thiercelin, M., 2011. Modelling borehole collapse with capability of predicting the scale effect. *ASCE Int. J. Geomech.* 11 (4), 286–293.
- Roegiers, J.C., Zhao, X.L., 1991. Rock fracture tests in simulated downhole conditions. In: The 32nd US Symposium on Rock Mechanics (USRMS). American Rock Mechanics Association. 10-12 July, Norman, Oklahoma. ARMA-91-221.
- Sarris, E., Papanastasiou, P., 2011. The influence of the cohesive process zone in hydraulic fracturing modelling. *Int. J. Fract.* 167 (1), 33–45.
- Segura, J. M., & Carol, I. (2010). Numerical modelling of pressurized fracture evolution in concrete using zero-thickness interface elements. *Engineering fracture mechanics*, 77(9), 1386-1399.
- Saouma, V. E., Natekar, D., & Hansen, E. (2003). Cohesive stresses and size effects in elastoplastic and quasi-brittle materials. *International journal of fracture*, 119(3), 287-298.
- Schmidt, R.A., Huddle, C.W., 1977. Effect of confining pressure on fracture toughness of Indiana limestone. *Int. J. Rock Mech. Min. Sci. Geomech. Abst.* 14 (5-6), 289–293. Pergamon, 1977.
- Serata, S., Sakuma, S., Kikuchi, S., & Mizuta, Y. (1992). Double fracture method of in situ stress measurement in brittle rock. *Rock mechanics and rock engineering*, 25(2), 89-108.

- Stephansson O. Rock stress measurement by sleeve fracturing. In: Proceedings of the 5th Cong. Int. Soc. Rock Mech., Melbourne, 1983. p. F129-137.
- Tomar, V., Zhai, J., & Zhou, M. (2004). Bounds for element size in a variable stiffness cohesive finite element model. *International journal for numerical methods in engineering*, 61(11), 1894-1920.
- Thallak, S.G., Holder, J., Gray, K.E., 1993. The pressure dependence of apparent hydro fracture toughness. In: The 34th US Symposium on Rock Mechanics (USRMS). American Rock Mechanics Association. 28-30 June, Madison, Wisconsin. ARMA-93-0665.
- Yao, Y. (2012). Linear elastic and cohesive fracture analysis to model hydraulic fracture in brittle and ductile rocks. *Rock mechanics and rock engineering*, 45(3), 375-387.
- Yoshioka, K., Zhang, Y., Lu, G. Y., Bungler, P. A., Adachi, J., El-Fayoumi, A., Bourdin, B. Revisiting the fracture toughness of rocks under confining pressure, *Rock Mechanics and Rock Engineering* submitted.
- Zhang, Y., 2019. Stress Dependence of the Burst Experiment for Determining Fracture Toughness. University of Pittsburgh. Master dissertation.
- Zielonka, M.G., Searles, K.H., Ning, J., Buechler, S.R., 2014, May. Development and validation of fully-coupled hydraulic fracturing simulation capabilities. In: Proceedings of the SIMULIA community conference, SCC2014, pp. 19–21.
- Zoback, M.D., Barton, C.A., Brudy, M., Castillo, D.A., Finkbeiner, T., Grollmund, B.R., Moos, D.B., Peska, P., Ward, C.D., Wiprut, D.J., 2003. Determination of stress orientation and magnitude in deep wells. *Int. J. Rock Mech. Min. Sci.* 40, 1049–1076.